CATALYTIC MICROCHANNEL CONFIGURATIONS FOR HYDROCRACKING OF FISCHER-TROPSCH HYDROCARBONS

by

Mehmet İrfan Hösükoğlu

B.S., Chemical Engineering, Boğaziçi University, 2009

Submitted to the Institute for Graduate Studies in
Science and Engineering in partial fulfillment of
the requirements for the degree of
Master of Science

Graduate Program in Chemical Engineering

Boğaziçi University

2011

CATALYTIC MICROCHANNEL CONFIGURATIONS FOR HYDROCRACKING OF FISCHER-TROPSCH HYDROCARBONS

APPROVED BY:

Assoc. Prof. Ahmet Kerim Avcı .....
(Thesis Supervisor)

Assoc. Prof. Hasan Bedir .....

Prof. Zeynep İlsen Önsan .....

DATE OF APPROVAL: 14.06.2011

ACKNOWLEDGEMENTS

I would like to express my deepest thanks to my supervisor Assoc. Prof. Ahmet Kerim Avcı, who was the driving force and guide of my graduate study. I am very grateful to God whom given me the opportunity to work with him.

I also would like to thank to my thesis committee members, Prof. Zeynep İlsen Önsan and Assoc. Prof. Hasan Bedir for devoting their valuable time to read and comment on my thesis.

Two special thanks goes to Gamze Gümüşlü whom helped me a lot with her previous studies and teaching assistance experiences during my master of science study and Mustafa Karakaya whom taught me everything I needed for my thesis with his endless patience starting from my graduation project.

I wish to thank Şefik Kerem Ovalı, Gülsüm Ersoy, Eyüp Şimşek and Murat Erol for the priceless friendship they have shown to me and who I will be grateful to be friend for the rest of my life. I would like to thank to my dear freinds in the department; Selcen, İpek, Aybüke, Caner, Burcu, Okan, Bahar, İrem, Ferit, Duygu, Ünal, Çağlar, Tarık, Ali, Vasfiye, Merve, Nilay, Kerem, Feyza, Bilgi Dedeoğlu, Nurettin Bektaş and Kamuran Çevre who made the days of my master study enjoyable and meaningful.

Even though the words are not capable of expressing my thankfulness, I would like to thank to my family for encouraging me to do my master of science study and supporting me and my decisions through out my life.

Finally, I would like to acknowledge Boğaziçi University Research Fund for the financial support provided through project BAP-09HA507D and TUBA-GEBIP program.

ABSTRACT

CATALYTIC MICROCHANNEL CONFIGURATIONS FOR HYDROCRACKING OF FISCHER-TROPSCH HYDROCARBONS

Petroleum crude oil is an important commodity as the primary source of energy and petrochemical industry but suffers from decreasing reserves and quality. Hydrocarbon commodities can also be produced synthetically by Fischer-Tropsch (FT) synthesis. Products of FT synthesis consist of a mixture of n-paraffins with wide ranges of molecular weights, boiling point fractions and poor cold flow properties due to their linear nature. These properties require improvement by catalytic hydrocracking for meeting the quality specifications. Hydrocracking of FT products decrease the heavy cut fractions by cracking and improves cold flow properties by isomerization. Hydrocracking reactions of FT hydrocarbons are exothermic and require precise temperature control; high temperatures lead to overcracking, whereas low temperatures inhibit the process. Integration of hydrocracking with microchannel reactor technology is a promising process, since sub millimeter dimensions of this technology minimizes transport resistances and allows temperature control and efficient use of catalyst. This work investigates the applicability of a heat-exchange integrated microchannel reactor for hydrocracking of FT hydrocarbons by parametric analysis in operational aspects. The reactor has parallel reaction, coated with a Pt based catalyst, and cooling channels separated by metallic walls. Integrated operation of simultaneous catalytic reactions and heat transfer are modeled and simulated using FEM based techniques. Kinetic model describes conversion of hydrocarbons species with in C_1-C_{70} range. The results show the possibility of isothermal operation at high temperatures and space velocities. Jet and diesel yields are found to be sensitive to reactant and coolant feed temperatures, feed flow rate and pressure of the reactant and wall material and almost unaffected by to H_2-to-wax ratio.

ÖZET

FİSCHER-TROPSCH HİDROKARBONLARININ HİDROKIRILMASI İÇİN MİKROKANALLI REAKTÖR DÜZENLERİ

Ham petrol petrokimya endüstrisi ve enerji piyasası için önemli bir kaynaktır ancak azalan rezervler ve kalite gibi sorunlar yaşamaktadır. Hidrokarbon mamüllerini Fischer-Tropsch (FT) sentezi ile üretmek mümkündür. FT sentezi ürünleri değişik molekül ağırlıklarına ve kaynama noktalarına sahip ve doğrusal yapılarından dolayı zayıf soğuk akış özellikli parafinler içerir. Bu özellikleri kalite şartlarına uygun hale gelebilmek için katalitik hidrokırılma işlemi gerektirir. FT sentezi ürünlerine hidrokırılma uygulanması ağır molekülleri hafif moleküllere dönüştürür ve izomerleşme ile soğuk akış özelliklerini iyileştirir. Hidrokırılma reaksiyonları sonucu ısı açığa çıkar ve hassas sıcaklık kontrolü gerekir, yüksek sıcaklıklar aşırı kırılmaya, düşük sıcaklıklar ise sürecin durmasına sebep olur. Hidrokırılma reaksiyonlarının milimetre altı boyutları ile taşınım dirençlerini düşüren, sıcaklık kontrolüne ve katalizörün verimli kullanımına olanak sağlayan mikrokanallı reaktör teknolojisine entegrasyonu umut vaadetmektedir. Bu çalışma FT ürünlerinin hidrokrılmasının ısı değişimli mikrokanallı reaktörlerde uygulanabilirliğini parametrik olarak incelemektedir. Reaktör, birbirine paralel ve metal duvarlarla ayrılmış, Pt bazlı katalizörle kaplanmış reaksiyon ve soğutma kanallarından oluşmaktadır. Katalitik reaksiyonlar ve ısıdeğişimi içeren entegre operasyon, sonlu elemanlar temelli teknikler kullanılarak çözümlenmiştir. Kinetik model 70 karbona kadar hidrokarbon bileşiklerinin dönüşümlerini içermektedir. Sonuçlar yüksek sıcaklıklarda ve akış hızlarında sabit sıcaklıkta operasyonun mümkün olduğunu göstermektedir. Jet ve dizel yakıt oranlarının reaksiyona giren ve soğutucu akışların giriş sıcaklıklarına, reaksiyona giren akışın miktarı ve basıncına ve duvar malzemesinin cinsine karşı hassas olduğu ve hidrojen hidrokarbon oranından az miktarda etkilendiği görülmüştür.

TABLE OF CONTENTS

ACKNOWLEDGEMENTS iii
ABSTRACT iv
ÖZET v
LIST OF FIGURES vii
LIST OF TABLES xii
LIST OF SYMBOLS xiv
LIST OF ABBREVIATIONS xvii
1. INTRODUCTION 1
2. LITERATURE SURVEY 3
2.1. Microstructured systems 3
2.2. Synthetic Fuel Production 6
2.2.1. Fischer-Tropsch Synthesis 7
2.2.2. Fischer-Tropsch Wax Hydrocracking 10
3. MODELING AND SIMULATION OF THE MICROCHANNEL REACTOR SYSTEM 14
3.1. Modeling 17
3.2. Parameters analyzed during simulations 28
4. RESULTS AND DISCUSSION 31
4.1. Effect of reactant and coolant feed temperatures and residence time on wax hydrocracking 36
4.2. Effect of wall material at jet and diesel fuel base configuration on wax hydrocracking 47
4.3. Effect of H_2-to-wax ratio on wax hydrocracking 63
4.4. Effect of reactive stream pressure on wax hydrocracking 69
5. CONCLUSIONS AND RECOMMENDATIONS 74
5.1. Conclusions 74
5.2. Recommendations 75
APPENDIX A: THERMOPHYSICAL PROPERTIES OF THE SPECIES . . 77
REFERENCES 87

LIST OF FIGURES

Figure 2.1. Number of FT Related Publications. 9

Figure 3.1. Feed stream molar vapor fraction: dependence on temperature . . 15

Figure 3.2. Feed stream molar vapor fraction: dependence on pressure 15

Figure 3.3. Kinetic Scheme of FT Hydrocracking Process 16

Figure 3.4. Composition of wax (n-paraffins) in the feed mixture 16

Figure 3.5. Microchannel reactor-heat exchanger system configuration. 17

Figure 3.6. Unit cell of the microchannel reactor-heat exchanger system. . . . 18

Figure 3.7. Total kinetic scheme of the model. 25

Figure 4.1. Temperature profile along reactor length under adiabatic conditions with complete conversion 32

Figure 4.2. Profiles of jet, diesel and heavy cuts along reactor length under adiabatic conditions with complete conversion 32

Figure 4.3. Feedstock and product compositions under adiabatic conditions with complete conversion 33

Figure 4.4. Temperature profile along reactor length under adiabatic conditions 34

Figure 4.5. Profile of jet, diesel and heavy cuts along reactor length under adiabatic conditions 34

Figure 4.6. Feedstock and product compositions under adiabatic conditions . . 35

Figure 4.7. 22+ n-hydrocarbon conversions at 440°C. 36

Figure 4.8. 22+ n-hydrocarbon conversions at 450°C. 37

Figure 4.9. 22+ n-hydrocarbon conversions at 460°C. 37

Figure 4.10. Molar fraction of diesel cut at 440°C. 38

Figure 4.11. Molar fraction of diesel cut at 450°C. 39

Figure 4.12. Molar fraction of diesel cut at 460°C. 39

Figure 4.13. Molar fraction of jet fuel cut at at 440°C. 41

Figure 4.14. Molar fraction of jet fuel cut at 450°C. 41

Figure 4.15. Molar fraction of jet fuel cut at 460°C. 42

Figure 4.16. Molar fraction of heavy cut at 440°C. 43

Figure 4.17. Molar fraction of heavy cut at 450°C. 44

Figure 4.18. Molar fraction of heavy cut at at 460°C. 44

Figure 4.19. Molar fraction of isomer to normal hydrocarbon ratio at 440°C. . . 45

Figure 4.20. Molar fraction of isomer to normal hydrocarbon ratio at 450°C. . . 46

Figure 4.21. Molar fraction of isomer-to-normal hydrocarbon ratio cut at 460°C. 46

Figure 4.22. Isomer-to-normal paraffin ratio at reactor outlet vs corresponding conversion. 47

Figure 4.23. Jet fuel, diesel fuel, heavy cut and conversion of 22+ n-hydrocarbon profiles along reaction channel at jet base configuration. 48

Figure 4.24. Temperature profile along reaction channel with different wall materials. 49

Figure 4.25. Temperature profile of along cooling channel with different wall materials. 49

Figure 4.26. 22+ N-hydrocarbon conversion profiles along reaction channel with different wall materials. 51

Figure 4.27. Jet fuel cut profiles along reaction channel with different wall materials. 52

Figure 4.28. Jet fuel cut at reactor outlet for different wall materials and WHSV values. 53

Figure 4.29. Diesel fuel cut profiles along reaction channel with different wall materials. 53

Figure 4.30. Heavy cut profiles along reaction channel with different wall materials. 54

Figure 4.31. Isomer-to-normal ratio profiles along reaction channel with different wall materials. 55

Figure 4.32. Jet fuel, diesel fuel, heavy cut and conversion of 22+ n-hydrocarbon profiles along reaction channel at diesel base configuration. 56

Figure 4.33. Temperature profile along reaction channel with different wall materials. 57

Figure 4.34. Temperature profile along cooling channel with different wall materials. 58

Figure 4.35. 22+ N-hydrocarbon conversion profiles along reaction channel with different wall materials. 59

Figure 4.36. Jet fuel cut profiles along reaction channel with different wall materials. 60

Figure 4.37. Diesel fuel cut profiles along reaction channel with different wall materials. 61

Figure 4.38. Heavy cut profiles along reaction channel with different wall materials. 62

Figure 4.39. Isomer-to-normal ratio profiles along reaction channel with different wall materials. 63

Figure 4.40. 22+ N-hydrocarbon conversion profiles at different H_2/wax ratios. 64

Figure 4.41. 22+ N-hydrocarbon conversion values at different H_2/wax ratios. . 64

Figure 4.42. Molar fraction of jet fuel cut profiles at different H_2/wax ratios. . 66

Figure 4.43. Molar fraction of diesel fuel cut profiles at different H_2/wax ratios. 66

Figure 4.44. Molar fraction of heavy cut profiles at different H_2/wax ratios. . . 67

Figure 4.45. Isomer to normal hydrocarbon ratio profiles at different H_2/wax ratios. 67

Figure 4.46. Reaction channel temperature profiles at different H_2/wax ratios. . 68

Figure 4.47. Cooling channel temperature profiles at different H_2/wax ratios. . 68

Figure 4.48. Conversion profiles for different reactive stream pressures. 69

Figure 4.49. Molar fraction of jet fuel cut profiles for different reactive stream pressures. 70

Figure 4.50. Molar fraction of diesel fuel cut profiles for different reactive stream pressures. 71

Figure 4.51. Molar fraction of heavy cut profiles for different reactive stream pressures. 71

Figure 4.52. Isomer to normal hydrocarbon ratio profiles for different reactive stream pressures. 72

Figure 4.53. Reaction channel temperature profiles for different reactive stream pressures. 72

Figure 4.54. Cooling channel temperature profiles for different reactive stream pressures. 73

LIST OF TABLES

Table 2.1. Main reactions in FT synthesis. 8

Table 3.1. Default properties of the unit cell. 19

Table 3.2. Boundary conditions used for the momentum conservation equations. 20

Table 3.3. Boundary conditions used for the mass transport equations. 21

Table 3.4. Boundary conditions used for the energy conservation equations. . 22

Table 3.5. Values of constant properties and ranges of variable properties. . . 29

Table 3.6. Configurations for the jet fuel base. 29

Table 3.7. Configurations for the diesel fuel base. 30

Table 3.8. Properties of wall materials. 30

Table A.1. Viscosity coefficients of hydrogen (micropoise). 77

Table A.2. Thermal conductivity coefficients of hydrogen (W/(mK)). 77

Table A.3. Enthalpy of formation values of normal hydrocarbons 78

Table A.4. Enthalpy of cormation values of iso-hydrocarbons and hydrogen . . 79

Table A.5. Heat capacities of normal hydrocarbons 80

Table A.6. Heat capacities of iso-hydrocarbons and hydrogen 81

Table A.7. Heat capacity constants of species. 82

LIST OF SYMBOLS

A	Constant in heat capacity equation
A_c	Cross-sectional area of wall
B	Constant in heat capacity equation
c_A	Concentration of species A
$\bar{c}_A$	Concentration of species A
C	Constant in heat capacity equation
C_P	Heat capacity of species
D	Constant in heat capacity equation
$\mathcal{D}_{AB}$	Diffusion coefficient of A in B
$\mathcal{D}_{AB,eff}$	Effective diffusion coefficient in catalyst layer
dS	Area increment
E	Constant in heat capacity equation
E_{cr}	Activation energy for cracking reaction
E_{iso}	Activation energy for isomerization reaction
F	Constant in heat capacity equation
F_A	Flow rate of species A
$\bar{F}_A$	Average flow rate of species A
F_{A0}	Initial flow rate of species A
G	Constant in heat capacity equation
H	Channel height
i	Species index
k_{cr}	Pre-exponential factor of rate constant of cracking reaction
k_{eff}	Effective thermal conductivity in catalyst layer
k_{gas}	Thermal conductivity of gas
k_i	Thermal conductivity of gas in channel i
k_{iso}	Pre-exponential factor of rate constant of isomerization reaction
k_{wall}	Thermal conductivity of wall
K_{cr}	Forward rate constant for cracking reaction

K_{eq}	Equilibrium constant for isomerization reaction
K_{iso}	Forward rate constant for isomerization reaction
L	Channel length
Ln	Natural logarithm
m	Channel index
M	Molecular mass
M_ω	Molecular weight
N	Normal
n	normal
p_A	Partial pressure of species A
p_i	Partial pressure in channel i
P	Total pressure
Q	Generated heat
r_{cr-Ci}	Rate of cracking reaction of species with i number of carbons
r_{iso-Ci}	Rate of isomerization reaction of species with i number of carbons
R	Universal gas constant
R_i	Rate of formation of species i
S	Cross-sectional area of channel
T	Temperature
T_i	Temperature within channel i
T_0	Initial temperature
T_w	Temperature of wall
υ	Linear velocity
υ_i	Linear velocity in channel i
$\bar{\upsilon}$	Average linear velocity
$\upsilon_{i,0}$	Initial linear velocity in channel i
υ_x	x component of linear velocity
$\upsilon_{x,i}$	x component of linear velocity in channel i
υ_y	y component of linear velocity
$\upsilon_{y,i}$	y component of linear velocity in channel i
V	Volume

V_0	Initial volumetric flow rate
ΔH_A	Heat of formation of A at T
ΔH_i	Heat of formation of species i at T
$\Delta H_{rxn,i}$	Enthalpy of reaction i at T
ε_p	Porosity of washcoat layer
κ	Permeability of washcoat layer
μ	Viscosity
ρ	Density
τ	Tortuosity of washcoat layer
σ	stoichiometric coefficient
ϑ	Structural volume increments

LIST OF ABBREVIATIONS

ADSORB	Adsorbtion term in reaction rates
C	Hydrocarbon species
CFD	Computational fluid dynamics
FTS	Fischer-Tropsch synthesis
HTFT	High temperature Fischer-Tropsch
iso	Isomer
LTFT	Low temperature Fischer-Tropsch
WHSV	Weight hourly space velocity

1. INTRODUCTION

Petroleum crude oil is an important commodity serving as the primary source of energy and petrochemical industry. However oil reserves are limited and expected to be insufficient for the demand in the long term. Although alternatives such as solar and wind energy offer sustainable solutions to energy needs, they cannot replace the fossil fuel use completely due to applicability and necessity of liquid products for petrochemical industry. Synthetic generation of liquid fuels via Fischer-Tropsch (FT) process, involving conversion of syngas ($CO+H_2$) to a wide range of hydrocarbons, is a promising option since it does not depend on crude oil and utilizes alternative resources such as natural gas, coal and biomass.

FT process produces a mixture of paraffins, olefins and oxygenates with a wide range of molecular weights, a large fraction of them being characterized by a high boiling point more than 370°C. Middle distillates fraction (i.e. 150-370°C cut), another group in the product stream, is known to present poor cold flow properties due their linear nature. Hydrocracking of FT product stream (also called) wax is a solution for increasing the yields of middle distillates by cracking of high boiling point components and improving cold flow properties of middle distillates by their isomerization.

Hydrocracking reactions of FT wax are highly exothermic and require strict temperature control; high temperatures lead to products lighter than the desired specifications whereas the process suffers from the decreased reaction rates at low temperatures at this point process intensification by using micro structured reactor heat exchanger systems can provide a novel way of achieving temperature control in hydrocracking reactions and optimizing product selectivity. Process intensification is a way of miniaturizing the process plants by micro structured equipment usage such as microchannel reactors and heat exchangers which are composed of channel sizes in the sub millimeter range. Microchannel equipments have advantages of high surface to volume ratio, enhanced heat and mass transfer rates and safer operations even at near explosives regimes.

This work investigates the response of the FT wax hydrocracking process in a heat exchange integrated microchannel reactor with respect to changes in process variables through parametric analyses. In these investigations FT wax is assumed to be composed of linear paraffins up to 70 carbon atoms. The reaction system is considered to be a microchannel network of square-shaped adjacent reaction and cooling channels in the form of parallel arrays, which are arranged such that reactant and coolant stream flows in successive channels in counter current mode. This configuration aims to control the temperature of the reaction channel and simplify the modeling of the system. Since same reactions are occurring or cooling fluid is flowing within the parallel groups of channels, the heat flow between identical channels are considered to be negligible compared to heat flow between successive reaction and cooling channels allowing the elimination of one spatial dimension from the calculations. The resulting set of two dimensional momentum, mass and energy balances which are partial differential equations are solved in COMSOL Multiphysics package using finite element method. The catalyst is considered as a washcoat porous layer on the walls of reaction channels where Brinkman type equations are used to model the reactive flow.

The process investigated contains 67 isomerizations and 66 cracking reactions on a Pt catalyst supported on amorphous silica alumina. The reaction mixture is assumed to contain only paraffins and isomerized products are grouped according to the number of carbon atoms. Parametric analysis is performed through making changes in wall material type, reactant (FT wax) and coolant feed temperatures, residence time of reactive stream, hydrogen-to-hydrocarbon (wax) ratio and reaction channel pressure, and observing the resulting effects on hydrocarbon cuts, temperatures of coolant and reactant streams, conversion of normal paraffins and isomer-to-normal hydrocarbon ratio.

The literature survey about FT synthesis, hydrocracking process and microchannel systems is given in Chapter 2. Mathematical modeling and simulation of microchannel system with the kinetic scheme of reactions are presented in Chapter 3. Results of simulations and related discussions are presented in Chapter 4. Chapter 5 contains the major outcomes of the study and recommendations for possible future work.

2. LITERATURE SURVEY

2.1. Microstructured systems

Microstructured systems, generally known as micro reaction systems, are devices composed of structured flow paths having dimensions from sub-micrometer to sub-millimeter range that are fabricated by using methods of microtechnology and precision engineering [1]. Microchannel technology is a novel approach in chemical processing hardware offering many advantages such as increased efficiency and productivity [2].

Main advantages of microstructured reactors can be summarized as; size reduction through micro fabrication, reduced transport distances, enhanced heat and mass transfer rates and processing yields, reduced reaction volumes, controlled systems avoiding contamination and reducing safety risks, replacing a batch process by a continuous one and reduced chemical consumption [3]. These advantages are making use of microreactors possible in diverse applications such as highly exothermic reactions, screening for potential catalysts, precision particle manufacture, high throughput materials synthesis, fuel cell construction, miniature and portable micro plants [4].

Currently a number of chemical processes are operating batch-wise since desired capacity is not sufficient for a continuous process. Some of these processes have reaction times longer than their kinetic requirements because of slow mass and heat transfer and low specific surface area. Replacing these processes by a continuous one in a microreactor can decrease contact times significantly due to fast transport in thin fluid layers [1]. Microsystems can also provide significantly enhanced conversion rates due to shorter diffusional lengths compared to the conventional reactors which was exemplarily verified for the intensification of heat transfer of thermally coupled high temperature reactions [5]. Calculations predict that amount of catalyst needed can be decreased up to a factor of 1000 by miniaturization [1].

For a given difference in a physical property such as temperature, pressure, con-

centration or density, higher respective gradients can be obtained by decreasing the linear dimensions. In other words higher driving forces for heat transfer, mass transport or diffusional flux can be obtained by use of microreactors. Present microreactors and micro heat exchangers have typical channel dimensions of 50 to 500 microns in which heat transfer coefficients up 25kW/m^{2}K have been measured which are higher at least one order of magnitude than those of conventional reactors [6]. Microstructured reactors also have high surface-to-volume ratios; specific surfaces of these units can reach up to 50,000 m^2/m^3 while typical production vessels do not exceed 100 m^2/m^3 [7]. This situation enhances the heat transfer in the reactor and it can also be utilized for the yields of gas phase and multiphase processes. In 2000 the highest interface reported was 25,000 m^2/m^3 for a falling film reactor while the best modern gas/liquid contactors were generating surfaces up to 2000 m^2/m^3 [8]. The difference in the volumes becomes larger if a large scale batch operation is replaced by a continuous operation in a micro-channel reactor, i.e; material hold up of a metalo-organic reaction could be decreased from a 6000 liter tank to a volume of few milliliters which also increases the process safety and increases selectivity due to shorter residence times [4]. Similarly size of a conventional steam reformer which has block dimensions around 30m x 30m x 30m can be reduced to 3.9m x 5.9m x 3.9m with use of micro-channel reactors [9].

Compact nature of microchannel units favors heat transfer, which is important for highly exothermic reactions in terms of effective catalyst utilization, favoring isothermal operation and preventing hot spots formation [10]. High heat transfer rates have been demonstrated in a steam methane reformer reactor where the energy required for reforming is supplied by partial oxidation of methane in adjacent channels[9]. In this study, heat transfer rates for the exothermic reaction exceeded 18W/m^2 and total volumetric heat flux has reached 65 W/cm^3 while in a conventional reactor volumetric heat flux remains 1W/cm^3 [9]. Enhanced heat transfer rates also makes it possible to control the temperature in a well established manner. Considering the fact that flow amount through the microflow units are smaller than the traditional reactors, use of microchannel reactors make operate safely at near explosive conditions including the reactions such as partial oxidations [11, 12]. In addition there are other examples of

operations in microreactors demonstrating safe operations at parameters of explosive regimes in conventional reactors [13].

Mass transfer just like heat transfer is better in microreactors. Since laminar flow is fully developed in microchannels the Sherwood number, which is mass transfer coefficient multiplied by hydraulic diameter divided by the diffusion coefficient, reaches a constant value. This implies that as the hydraulic diameter gets smaller, the mass transfer coefficient gets larger, decreasing the mass transfer limitation [14]. Another beneficial feature of micro sized units is the narrow residence time distribution. This increases the selectivity for production of specific material as it also enables easier scaling up by only increasing the number of units keeping the required geometry the same. [15]

Micro reaction technology offers operational flexibility for the limitations of conventional FT synthesis reactors. Since capacities of FT reactors are limited by the heat removal capacity of reactors and FT synthesis is a highly exothermic reaction, microchannel reactor is a promising option in terms of temperature control through rapid heat transfer [16]. Moreover, conventional gas-to-liquid complexes are only suitable for onshore applications as they require very high investment costs making them only feasible for very large gas reserves. Microreactor based GTL technologies can overcome these limitations since these reactors require lower investment costs and are suitable for gas reserves associated to smaller oil fields in remote or deep-water areas and these systems can be adapted to onshore, offshore and mobile/on-board applications [17]. Microstructured reactors also enhances the efficiency of catalyst for Fischer-Tropsch synthesis, it is shown that turnover activity of $FeCrAlY/Al_2O_3$ catalyst is enhanced by a factor of four due to its microstructure [18].

Microchanneled reactors are significantly compact processing unit which offers the possibility of transportation [19]. Currently, chemical productions are carried out in large facilities, which are aimed to be as large as possible in terms of capacities due to economic reasons. However, as in case of petrochemical industries, raw materials need to be transported over long distances to a central plant, which makes a

vast number of small sized and remote feedstocks unprofitable. These feedstocks could be processed with microstructured systems since processing in microreactors requires less investments and operational costs [1]. There are also examples of processes generally with reactions of extremely toxic substances which may benefit from distributed production with the help of micro-structured reactors [1].

2.2. Synthetic Fuel Production

Synthetic fuel generation involves catalytic conversion of carbon sources such as coal and natural gas to high quality fuels that can meet primary energy requirements and can be utilized as raw materials for petrochemical industry.

Synthetic fuel production has started in 1925 by German official's decision to develop an independent source of transportation fuels after they have handicapped by their poor oil resources during WW I since US was the principal exporter of oil at those years. First commercial production of synthetic fuel was direct liquefaction of coal under high pressure with hydrogen (H_2), which was called Bergius process and awarded the Nobel Prize in 1931. In addition to the production based in Germany until the end of World War II, there are two periods in which synthetic fuel production became important; after the Arab embargo in 1972 and after 1985 to present. [20] Currently world is dealing with the two problems of fossil fuel usage, environmental problems and depletion of reserves [21].

Considering the facts that oil reserves will deplete in the following 40 years and gas and coal reserves will exist in the following 65 and 1300 years respectively, vehicle travel and fossil fuel demand in 2020 will be the triple of the corresponding statistics of 1990 [21, 22]. Such a scenario emphasizes the importance of synthetic fuel generation. Moreover synthetic fuels are attractive since they are free from sulfur, nitrogen and aromatics which make them suitable for upcoming stringent environmental regulations [23].

Several methods are available for production of synthetic fuels depending on

source and production technology which can be summarized as oil shale retorting, coal liquefaction by direct hydrogenation and indirect liquefaction, coal gasification, biomass liquefaction and gasification, tar sands recovery, solid waste liquefaction and gasification [24]. Although coal reserves exceed the sum of all the alternatives, in the short term, natural gas will be preferred for economic and environmental reasons. However, in the long term, coal will hold the dominant position in the synthetic fuel generation due to lack of alternatives [22].

Synthetic fuel generation process involves three major steps; synthesis gas generation, Fischer-Tropsch synthesis and wax hydrocracking. The process is named as XTL (X-to- Liquids) where X is G, C, B, if the starting raw material is natural gas, coal and biomass, respectively. Production of synthesis gas (a mixture of CO and H_2) from coal or natural gas is the most expensive one of the three steps; it accounts up to 70% of capital and running cost of synthetic fuel generation [25]. Conversion of synthesis gas to higher hydrocarbons occurs in the Fischer-Tropsch synthesis step, and the products, collected under the general title of FT wax, are hydro-processed (cracked) to give the synthetic fuels such as gasoline and diesel. CTL and GTL start to become more profitable for liquid fuel production than crude oil refining if oil prices exceeds 60$/bbl for CTL and 36$/bbl for GTL process [26]. Currently there are plans about construction and operation of a number of large scale GTL plants which will result in a total production capacity of 1 million barrels/day within the next decade [27].

2.2.1. Fischer-Tropsch Synthesis

Fischer-Tropsch fuel production has started in 1935 at Germany and nine CTL plants were built and operated until 1945 [28]. After WW II, FT fuels have been produced especially in South Africa to reduce the nation's dependence on foreign oil. Coinciding with the high oil prices in 1970s, productions in South Africa have reached an economic success [29]. After 1990s construction of GTL plants started to utilize the stranded gas reserves [30].

Franz Fischer and Hans Tropsch developed a process in 1920 to produce diesel fuel

Table 2.1. Main reactions in FT synthesis.

1	Paraffin	$nCO+(2n+1)H_2 \longrightarrow C_nH_{2n+2}+nH_20$
2	Olefins	$nCO+(2n)H_2 \longrightarrow C_nH_2+nH_20$
3	Water Gas Shift	$H_2O+CO \longrightarrow H_2+CO_2$

from synthesis gas with a series of reactions in the presence of catalyst [31]. Reactions series include combinations using iron/cobalt catalyst to react hydrogen and carbon monoxide to form paraffins, olefins and alcohols. These reactions are highly exothermic and not specific to the formation of any single compound [24]. Table 2.1 shows the main reactions of Fischer-Tropsch synthesis.

Among several suitable transition metal catalysts, cobalt and iron are the most common ones that are being used in FT synthesis. Cobalt is more preferred when the feedstock is natural gas since syngas produced from natural gas has high hydrogen to carbon monoxide ratio and does not need water gas shift reaction. Iron catalysts are more preferred when the feedstock is lower quality such as coal and biomass, resulting in lower hydrogen-to-carbonmonoxide ratios [27].

Fischer Tropsch processes are classified into two groups according to their operation temperature; high temperature FT (HTFT) between 310-340°C and low temperature FT (LTFT) between 210-260°C [29]. Products of FT synthesis are highly dependent on operation temperature and catalyst type. HTFT yields more naphtha and lower amounts of hydrocarbons with boiling points above 360°C, whereas LTFT yields significant amounts of hydrocarbons with boiling points above 360°C. In addition final composition of HTFT process contains aromatic and olefins while LTFT process gives mainly paraffins. In other words, HTFT process is more suitable for gasoline production and LTFT process is more suitable for diesel production [32]. It is possible to obtain ultra clean and high cetane number fuels with FT synthesis which are virtually free from sulfur and aromatic hydrocarbons. These fuels can facilitate further reduction in the internal combustion engine emissions and have a very high potential for realizing the upcoming environmental regulations without decreasing the

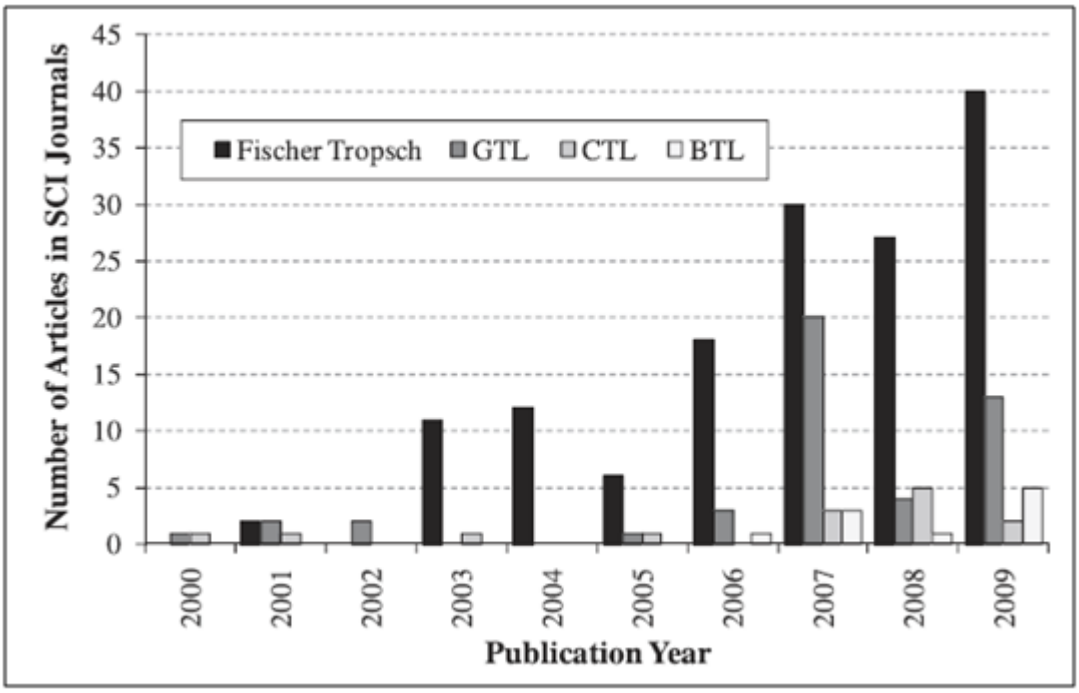

Figure 2.1. Number of FT Related Publications.

fuel efficiency [33].

Interests in renewable energy and alternative fuels are increasing significantly because of the concerns about limited future oil resources and requirements of carbon dioxide reductions. As it can be seen in Figure 2.1 there is an exponential increase in the number of publications related to FT synthesis [27].

Reactions included in FT synthesis are highly exothermic with a reaction enthalpy around 170 kJ/mol and require strict temperature control. Simulation studies show that micro structured reactors can provide the highest productivity per unit catalyst among slurry bubble reactors and monolith reactors [34]. It is also shown by computational fluid dynamics simulations that micro-channeled reactor with heat exchange systems are suitable for temperature control and consequently product control of FT synthesis with acceptable pressure drop values [35].

2.2.2. Fischer-Tropsch Wax Hydrocracking

After 1990 European Union started to apply strict standards for diesel quality and exhaust gas emission in terms of NO_x, CO, hydrocarbon and particulate matters. Current environmental regulations are forcing a minimum diesel cetane number of 51 and sulfur content less than 10 ppm since 2009 [36]. In addition common additives of gasoline to improve the octane number such as aromatics and olefins have to be substituted paraffins and naphthenes [37]. Turkey also started to apply similar regulations since 2011 by prohibiting the sales of agricultural diesel which can have up to 1000 ppm sulfur and by reducing maximum sulfur content of standard diesel fuel from 50 ppm to 10 ppm [38].

Fuels that are acceptable according to these standards can be produced by Fischer-Tropsch synthesis by using feedstocks such as biomass, natural gas and coal with proper sulfur removal applications. Fischer-Tropsch synthesis products are mainly composed of long chain normal paraffins and small amounts of aromatics which do not have sulfur and nitrogen [39].

Fischer Tropsch synthesis is suitable for production of high quality and clean gasoline and diesel fuels. However, it is not possible to produce a specific cut such as gasoline or diesel since the process produces a distribution of hydrocarbons that contains a wide range of molecular weight hydrocarbons. Therefore, hydrocracking should be applied to FT products to increase the fraction of desired components but the process should not crack the components already in the desired range. [39]

FT synthesis is generally operated at low temperature mode for decreasing the selectivity towards light hydrocarbons, which means wasting the raw material. LTFT synthesis provides products with boiling points higher than 350°C, yield of middle distillate range is limited and distribution is strongly biased to long chain paraffins. As a result, FTS produces middle distillates with very high cetane numbers (more than 75 while regulations require 51) but the products have very poor cold flow properties which cause problems both in direct use in internal combustion engines and in

indirect use as a blending component in diesel pool [40]. There are studies aiming the improvement of the process by increasing the intrinsic selectivity towards desired fractions by catalysts and process conditions, but these studies have reported limited success [40]. The most effective method to maximize to yield the fraction of a desired distillate is the hydrocracking of FT wax in which two main reactions, hydrocracking and hydroisomerization are occurring [41].

Isomer content is an important property for diesel which affects both cold flow properties and cetane number. In other words, controlling the amounts of isomers and the degree of branching are important objectives of hydrocracking process [42]. Hydroisomerization reactions lead to significant increases in the cold flow properties of FT diesel. The freezing point of C_{10} - C_{14} fraction decreases from -23°C to -45°C and pour point of C_{15} – C_{22} fraction decreases from 13°C to -23°C. Isomerization is an important benefit of hydrocracking at the expense of lowering the cetane number of product [40].

In addition to isomerizations hydrocracking reactions increase the amounts of middle distillate yields in a range between 80% to 85% while keeping methane and ethane yields low, since reactivity of linear paraffins increases with the molecular weight. The higher activity of heavier paraffins can be explained by their stronger physisorption which results in higher concentration on catalyst compared to the bulk phase and higher reaction rates accordingly [40]. Hydrocracking of a linear paraffin occurs after a variety of successive reactions. The first step in the process is dehydrogenation of alkanes to produce olefin intermediates, which then forms carbenium ions that are adsorbed on the acid sites of catalyst. These adsorbed carbenium ions undergo acid catalyzed isomerization then crack with respect to the carbon atom bearing the positive charge. After the cracking the isomerized and cracked species desorb from the acid site and hydrogenate on the metal site forming the corresponding paraffins. Finally the described process produce paraffins with smaller number of carbon atoms and higher degree of branching [43].

Hydrocracking process requires bi-functional catalyst characterized by the pres-

ence of acidic sites, which are active in cracking function, and a metallic site for the hydrogenation/dehydrogenation steps [39]. Various metals such as Pt, Ni and Mo, and different acidic supports such as zeolites, sulfated zirconia, silicoaluminaphosphates and amorphous silica alumina have usage in hydrocracking catalysts. The degree of isomerization and cracking can be controlled by changing the acidic strength or by the shape selectivity of some zeolite structured materials. Some mesoporous materials also have usage even though they have milder acidities and lower thermal resistances which make them suitable for isomerization but not for hydrocracking [44].

Fischer-Tropsch wax differs from the conventional heavy oil in a manner that it does not contain sulfur and the only hydrocarbon types present are normal paraffins. In other words, FT wax hydrocracking involves milder conditions compared to conventional refinery hydrocracking [45]. For hydrocracking of heavy oil hydrocarbons, bimetallic systems are commonly used, due to their high sulfur contents [46].

Rossetti and coworkers have observed a positive relationship between H_2/wax and C_{22+} conversion which is an unexpected situation according to the kinetic expressions they have used. This situation is explained by vapor liquid equilibrium, with the increase of H_2/wax ratio, vapor fraction of system and vapor fraction of hydrocarbons increases together. Hydrocarbons that are adsorbed on catalysts surfaces could not be replaced by fresh hydrocarbons unless they crack and become lighter hydrocarbons. In other words residence time of hydrocarbons that are adsorbed once increase, which results at higher conversions [44]. There is a negative relation between the C_{22+} conversion and pressure, the negative relation can be explained by the bi-functional mechanism of catalyst where first step, formation of adsorbates on metal site, is followed by the formation of carbenium ion at acidic site. In this mechanism rate limiting step is rearrangement of carbenium ions while the other steps are assumed to be at quasi equilibrium. Increasing the pressure in the system results at lower steady state concentrations of secondary carbenium ions and accordingly a decreased rate limiting step which is slowing the overall process [47]. Experimental studies also show that there is a positive relation between hydrocracking and temperature and residence time, as expected due to kinetic reasons [47]. It is also shown that reactivity of heavier hydro-

carbons is higher than those of lower hydrocarbons which is related to the stronger physisorption of heavier molecules on catalyst surface [44].

In order to model and simulate a hydrocracker efficiently, a kinetic model that can capture the complex chemistry of the process is required. In the last two decades, hydrocracking and hydroisomerization have been the object of several studies. In an ideal model different reactions and mechanisms relevant to all components in the reaction mixture have to be taken into account, but, in practice, it is very difficult to keep track of each component. Based on this fact all of the models available in the literature investigate the process by grouping the hydrocarbons [46]. There are two groups of such models. First group of models is based on discrete lumping of hydrocarbons as pseudo components according to a physical property, and second group of models considers the components as a continuous mixture with regard to an identifying parameter like boiling point temperature, molecular weight etc. [46]. In 2007, Pellegrini and coworkers developed a model enhancing their previous lumped models, that is tracking each linear paraffin independently and lumping only isomers of the same carbon number [48]. In this study model of Pellegrini and coworkers is used as basis for reaction kinetics mechanism and will be explained further in the modeling part.

There is another group of models which is an alternative to lumped models that is based on a theory called "Single Event". This theory is based on tracking each elementary reactions taking place on the surface of catalyst [46]. Models based on single event theory requires considering the reaction rates of each elementary step involved in carbenium ions on a molecular level. However it is not possible to measure concentrations of olefins and ion intermediates which are in very small amounts compared to the saturated species. Hydrogenation/dehydrogenation and protonation/deprotonation reactions are assumed to be in thermodynamic equilibrium and acid surface reactions are considered as rate limiting step [43].

3. MODELING AND SIMULATION OF THE MICROCHANNEL REACTOR SYSTEM

This chapter explains the microchannel reactor heat exchanger system and methods used to simulate the reactions and transport phenomena occurring inside the system. In this work hydrocracking of FT wax inside a microchannel reactor heat exchanger system with Pt on amorphous silica alumina catalyst is investigated by utilizing the kinetic data available in literature [48].

The feedstock of hydrocracking reactions contains only linear paraffins ranging from 5-70 number of carbons and excess amounts of hydrogen in molar basis. Molar fraction of hydrogen in the mixture is around 95% at the inlet and does not decrease below 93% within the investigated conversion range. All of the kinetic models in the literature considers the mixture in gaseous phase since vapor fraction of the system does not fall below 96% in typical operating conditions; the lowest value observed is 93% with the lowest hydrogen to hydrocarbon ratio in the investigated range [49]. Moreover, a kinetic model that considers vapor liquid equilibrium is not available in literature. Therefore in this study, it is assumed that the reactant stream is in vapor phase only.

Pellegrini and coworkers investigated the vapor fraction of the feed stream in their modeling study and its dependence on pressure, temperature and hydrogen-to-hydrocarbon ratio [49]. Effect of temperature and pressure on vapor fraction of reactant stream are shown in Figure 3.1 and Figure 3.2 respectively. As it can be seen from the figures, vapor fraction of the system is around 97% in most cases [49] Feed temperatures investigated in this study are well above the temperature range investigated by Pellegrini and coworkers, so its safe to treat the reaction channel to operate in gaseous phase.

Hydrocracking reactions are briefly illustrated in Figure 3.3, it is assumed that there are 67 isomerization and 66 cracking reactions occurring inside the system. Feed-

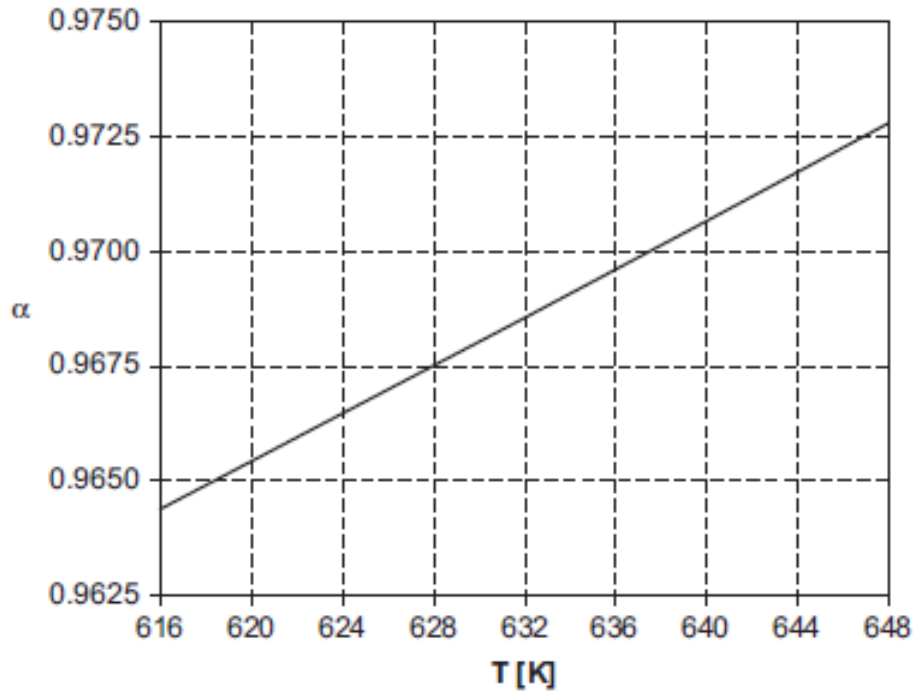

Figure 3.1. Feed stream molar vapor fraction: dependence on temperature (P=47. 5 bar, H2/waxes = 0. 105 kg/kg)[49].

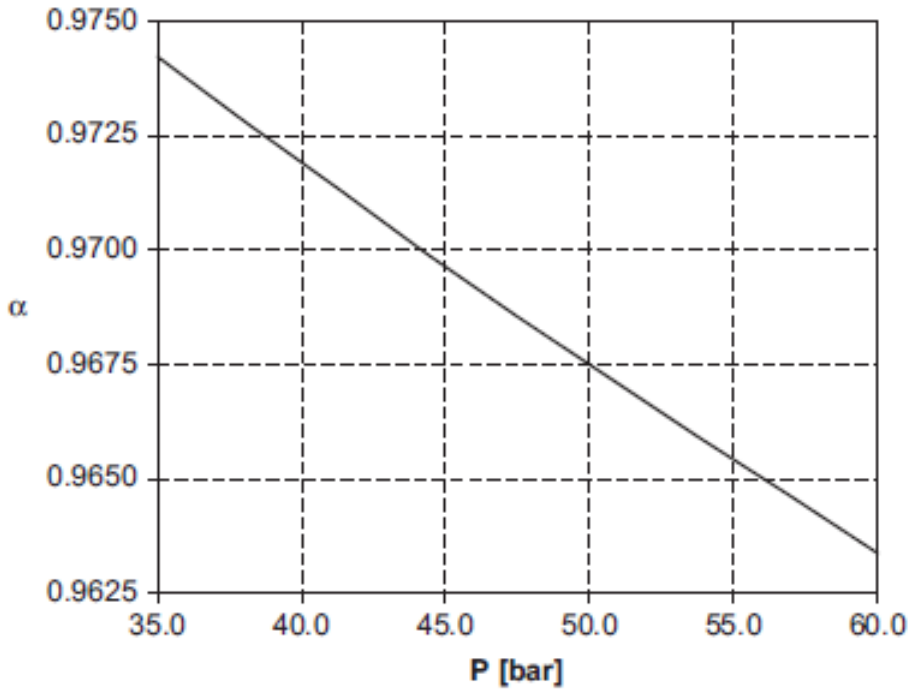

Figure 3.2. Feed stream molar vapor fraction: dependence on pressure (T = 632. 15 K,H2/waxes = 0. 105 kg/kg)[49].

stream which is composed of linear paraffins only, is characterized by the composition shown in Figure 3.4. Enthalpies of cracking reactions at 450° change between 27 and 49 kJ/mol. Some assumptions are made during the simulations which are listed below.

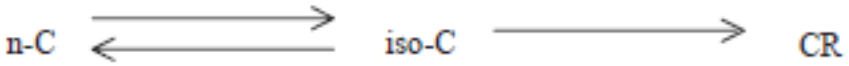

Figure 3.3. Kinetic Scheme of FT Hydrocracking Process [46].

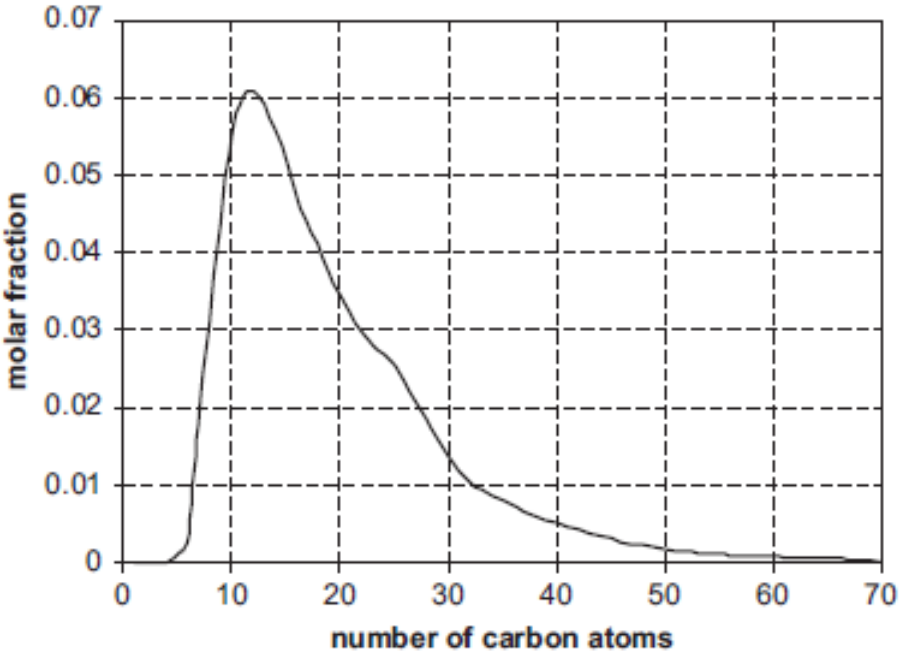

Figure 3.4. Composition of wax (n-paraffins) in the feed mixture [49].

- Heat capacity and heat of formation values of isomers with more than 20 carbon are assumed to be the same as those of corresponding linear hydrocarbons, since data is not available in literature and total number of carbon and hydrogen atoms and numbers and types of inter atomic bonds do not change during isomerization.

- Reactant stream is assumed to behave like ideal gas and density of this stream is calculated accordingly, since majority of the reactant stream is made of hydrogen and reduced temperature of hydrogen in the investigated temperature range is more than 20 [50].

- Viscosity of the reactant stream is assumed to be same as hydrogen since majority of the reactant stream is composed of hydrogen.

- Cracking of isomerized species is assumed to occur at carbon bonds in the center of hydrocarbon molecule.

3.1. Modeling

The microchannel reactor heat exchanger system is illustrated at Figure 3.5. The system consists of rectangular microchannels either used for reaction channel for the exothermic reaction or for flow of cooling stream used as heat sink to absorb heat released by the reaction channel. Walls of reaction channels are coated with a porous, platinum supported on amorphous silica alumina catalyst layer.

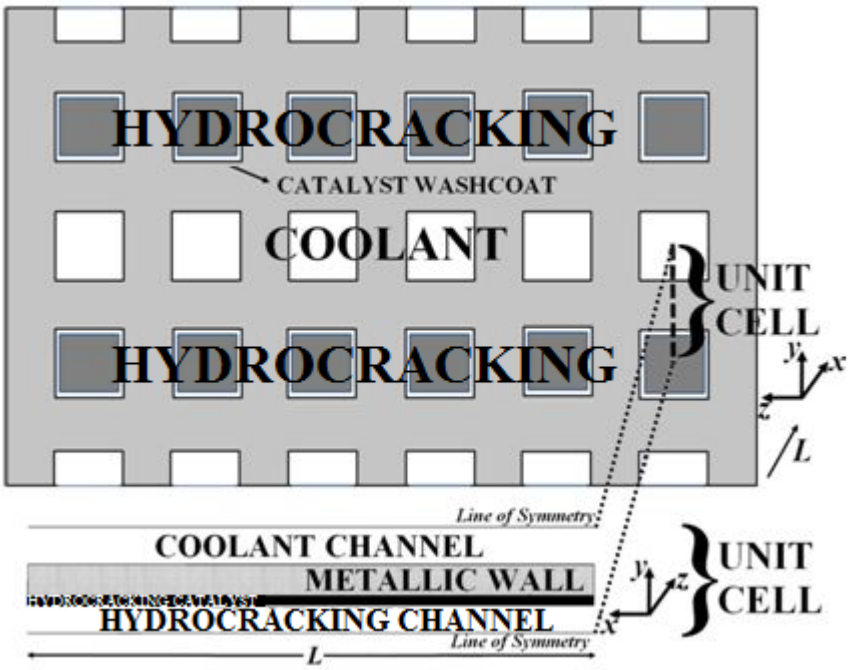

Figure 3.5. Microchannel reactor-heat exchanger system configuration.

The system is arranged in a parallel organization in z direction. Properties of the fluids flowing in the same horizontal group do not differ and heat transfer in the z direction is negligible compared to heat flow in the x and y directions. Since the calculations are performed in Cartesian coordinate system and gradient in z direction is negligible, simulations are carried out in two dimensional environment.

A two dimensional unit cell is used for simulations which contains domains between the centerlines of reaction channel and adjacent cooling channel, both of which became symmetry axes as a result of repeating pattern. Since heat flow in z direction is negligible, centerlines act as symmetry axes, and it is possible to understand the dynamics in the whole system by modeling and simulating the unit cell. A detailed description of unit cell is given in Figure 3.6

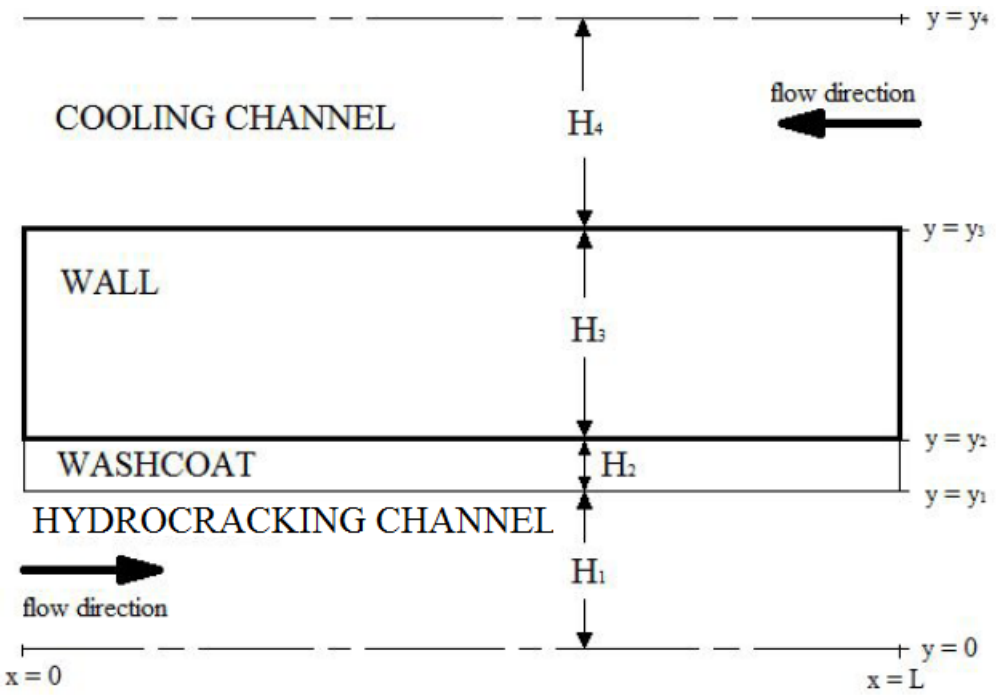

Figure 3.6. Unit cell of the microchannel reactor-heat exchanger system.

Default dimensions and properties of the unit cell shown in Figure 3.6, are summarized in Table 3.1.

Reactant stream flows inside the hydrocracking channel and coolant stream flows inside cooling channel in counter current direction to the reactant stream. Reactor wall separates the two channels while conducting the heat released from the hydrocracking channel. Washcoat domain contains the porous catalyst and it assumed that reactions take place only in the washcoat domain. Flowing gases are treated as incompressible, non-reactive, Newtonian fluids.

Modeling and simulation of hydrocracking reaction and heat transfer inside the

Table 3.1. Default properties of the unit cell.

Side length of the reaction channel	500 μm	2xH_1
Washcoat thickness	50 μm	H_2
Reactor Wall thickness	300 μm	H_3
Side length of the cooling channel	600 μm	2xH_4
Length	0.1 m	L
Reactor Wall Material	Steel-AISI	
Coolant	Steam	

system requires simultaneous solution of momentum, mass and energy conservation equations in the four domains named as hydrocracking channel, washcoat layer, wall and cooling channel. Conservation of momentum is valid for domains involving fluid flow (hydrocracking channel, washcoat layer and coolant channel) The two dimensional Navier-Stokes equations in Cartesian coordinates for Newtonian fluids are used to solve the momentum balances for fluid phases. The equations are given as follows [51]:

$$\rho_m(\upsilon_{x,m}\frac{\partial \upsilon_{x,m}}{\partial x} + \upsilon_{y,m}\frac{\partial \upsilon_{x,m}}{\partial y}) = -\frac{\partial p_m}{\partial x} + \mu_m(\frac{\partial^2 \upsilon_{x,m}}{\partial x^2} + \frac{\partial^2 \upsilon_{x,m}}{\partial y^2}) \tag{3.1}$$

$$\rho_m(\upsilon_{x,m}\frac{\partial \upsilon_{y,m}}{\partial x} + \upsilon_{y,m}\frac{\partial \upsilon_{y,m}}{\partial y}) = -\frac{\partial p_m}{\partial y} + \mu_m(\frac{\partial^2 \upsilon_{y,m}}{\partial x^2} + \frac{\partial^2 \upsilon_{y,m}}{\partial y^2}) \tag{3.2}$$

In the equations given above m is used to identify the channels as hydrocracking channel (m=1) and cooling channel (m=2). A modified form of momentum conservation equation known as Brinkman equations are used to model flow in porous the washcoat layer [51]:

$$(\frac{\mu_1}{\kappa})\upsilon_{x,1} = -\frac{\partial p_1}{\partial x} + (\frac{1}{\epsilon_p})\mu_1(\frac{\partial^2 \upsilon_{x,1}}{\partial x^2} + \frac{\partial^2 \upsilon_{x,1}}{\partial y^2}) \tag{3.3}$$

$$(\frac{\mu_1}{\kappa})\upsilon_{y,1} = -\frac{\partial p_1}{\partial y} + (\frac{1}{\epsilon_p})\mu_1(\frac{\partial^2 \upsilon_{y,1}}{\partial x^2} + \frac{\partial^2 \upsilon_{y,1}}{\partial y^2}) \tag{3.4}$$

In Equations (3.3) and (3.4), ϵ_p is the porosity and κ is the permeability related to with the used catalyst. The porosity is taken as 0.5 and permeability as 1x10^{-8} [52] Boundary conditions related to Equations (3.1) to (3.4) are given in Table 3.2.

Table 3.2. Boundary conditions used for the momentum conservation equations.

x=0	0<y<y_1	$\upsilon_1 = \upsilon_1^0$
	y_3 <y<y_4	$p_2 = p_{2out}$
x=L	0<y<y_1	$p_1 = p_{1out}$
	y_3 <y<y_4	$\upsilon_2 = \upsilon_2^0$
y=0	∀x	n.υ_1=0
y=y_1	∀x	n.υ_1=0
y=y_2	∀x	υ_1=0
y=y_3	∀x	υ_2=0
y=y_4	∀x	n.υ_2=0

It is required to calculate the mass transport of species in the hydrocracking channel and washcoat layer, since concentration of reactants change along the channel and the washcoat layer as a result of hydrocracking reaction. Considering the fact that reaction is taking place only in the catalytic washcoat layer, Equations (3.5) and (3.6) used to calculate mass transfer in hydrocracking channel and washcoat layer respectively [51].

$$\upsilon_{x,1}\frac{\partial c_A}{\partial x} + \upsilon_{y,1}\frac{\partial c_A}{\partial y} = \mathcal{D}_{AB}\left(\frac{\partial^2 c_A}{\partial x^2} + \frac{\partial^2 c_A}{\partial y^2}\right) \tag{3.5}$$

$$\upsilon_{x,1}\frac{\partial c_A}{\partial x} + \upsilon_{y,1}\frac{\partial c_A}{\partial y} = \mathcal{D}_{AB,eff}\left(\frac{\partial^2 c_A}{\partial x^2} + \frac{\partial^2 c_A}{\partial y^2}\right) + r_A \tag{3.6}$$

The subscript A is used for the linear paraffins ranging from 1-70 carbon, isomerized paraffins ranging from 4-70 carbon and hydrogen. Boundary conditions related to Equations (3.5) and (3.6) are given in Table 3.3.

Table 3.3. Boundary conditions used for the mass transport equations.

x=0	0<y<y_1	$c_A = c_A^0$
x=L	0<y<y_1	$n.(-\mathcal{D}_{AB}\nabla c_A) = 0$
y=0	$\forall$x	$n.(-\mathcal{D}_{AB}\nabla c_A + c_A \upsilon_1) = 0$
y=y_2	$\forall$x	$n.(-\mathcal{D}_{AB}\nabla c_A + c_A \upsilon_1) = 0$

Effective diffusivity appearing in Equation (3.6) is calculated from binary diffusivity by taking tortuosity, which is taken as 2 [53], and porosity (0.5) of the catalyst into account [54]:

$$\mathcal{D}_{AB,eff} = \frac{\epsilon_p}{\tau}\mathcal{D}_{AB} \tag{3.7}$$

Heat releases from the hydrocracking channel since the reactions taking place are exothermic. Steam, which is selected as the cooling fluid, flows in to the cooling channel and absorbs heat released from the hydrocracking to control its temperature. The heat is generated at the washcoat layer and is dissipated into both hydrocracking and coolant channels by passing through the wall material. Energy conservation equations that give temperature changes in the hydrocracking and cooling channels (Equation (3.8)), washcoat layer (Equation (3.9)) and wall phases (Equation (3.10)) are given below [51]. Boundary conditions related to Equations (3.8)-(3.10) are given in Table 3.4. In Equation (3.10), thermal conductivity of the washcoat is taken as 4.5 times of the thermal conductivity of the fluid [52].

$$\rho_i C_{Pi}(\upsilon_{x,i}\frac{\partial T_i}{\partial x} + \upsilon_{y,i}\frac{\partial T_i}{\partial y}) = k_i(\frac{\partial^2 T_i}{\partial x^2} + \frac{\partial^2 T_i}{\partial y^2}) \tag{3.8}$$

$$\rho_i C_{Pi}(\upsilon_{x,i}\frac{\partial T_i}{\partial x} + \upsilon_{y,i}\frac{\partial T_i}{\partial y}) = Q + k_{eff}(\frac{\partial^2 T_i}{\partial x^2} + \frac{\partial^2 T_i}{\partial y^2}) \tag{3.9}$$

$$k_{wall}(\frac{\partial^2 T_i}{\partial x^2} + \frac{\partial^2 T_i}{\partial y^2}) = 0 \tag{3.10}$$

Table 3.4. Boundary conditions used for the energy conservation equations.

x=0	0<y<y_1	$T_1 = T_1^0$
	y_1 <y<y_2	n.$(-k_{eff}\nabla T_1) = 0$
	y_2 <y<y_3	n.$(-k_{wall}\nabla T_w) = 0$
	y_3 <y<y_4	n.$(-k_2\nabla T_2) = 0$
x=L	0<y<y_1	n.$(-k_1\nabla T_1) = 0$
	y_1 <y<y_2	n.$(-k_{eff}\nabla T_1) = 0$
	y_2 <y<y_3	n.$(-k_{wall}\nabla T_w) = 0$
	y_3 <y<y_4	$T_2 = T_2^0$
y=0	∀x	n.$(-k_1\nabla T_1) = 0$
y=y_1	∀x	n.$(-k_1\nabla T_1 - k_{eff}\nabla T_1) = 0$
y=y_2	∀x	n.$(-k_{eff}\nabla T_1 - k_{wall}\nabla T_w) = 0$
y=y_3	∀x	n.$(-k_{wall}\nabla T_w - k_2\nabla T_2) = 0$
y=y_4	∀x	n.$(-k_2\nabla T_2) = 0$

The heat generated (Q) in catalyst layer as a result of reactions is calculated via molar enthalpies of species involved in reactions. The molar enthalpy of species A, ΔH_A (J/mol^{-1}), at a specified temperature is calculated using Equation (3.11):

$$\Delta H_A = \Delta H_{A0} + \int_{T_0}^{T} C_{PA} dT \tag{3.11}$$

C_{PA} term in Equation (3.11) is calculated by Equation (3.12) using constants A, B, C, D, E, F, G related to specific heat capacity, C_P (J mol$^-$1 K$^-$1), calculation of species [55]:

$$C_{PA} = A + BT + CT^2 + DT^3 + ET^4 + FT^5 + GT^6 \tag{3.12}$$

Heat released by a reaction is calculated by subtracting enthalpy of reactant species

from product species by Equation (3.13):

$$\Delta H_{rxn,i} = \sum \sigma_i \Delta H_i \tag{3.13}$$

where σ is the stoichiometric coefficient of species in the reaction negative for reactants and positive for products. Heat generated by the reactions are calculated by Equation (3.14):

$$Q = \sum r_i \Delta H_{rxn,i} \tag{3.14}$$

Finally, the continuity equation used in all channels and in washcoat domain can be given as follows [51]:

$$\frac{\partial \upsilon_x}{\partial x} + \frac{\partial \upsilon_y}{\partial y} = 0 \tag{3.15}$$

Properties of solids (density and thermal conductivity) are assumed to be constant against temperature changes, whereas properties of gases are considered to change with temperature. Coolant is assumed to be pure steam, whose properties are taken directly from the material library of COMSOL Multiphysics, the package used to solve Equations (3.1)-(3.15) by finite element based techniques. Viscosity and thermal conductivity of reactant stream are assumed to be the same as those of hydrogen since mole fraction of hydrogen is around 94% in the reactant stream. Viscosity and thermal conductivity of hydrogen are calculated according Equations (3.16) and (3.17) respectively. Density and heat capacity of the reactant stream is calculated according to the feed composition and is assumed to be constant along the reactor. Heat capacity species are calculated by Equation (3.12) and density of the reactant stream is calculated by Equation (3.18).

$$\mu = A + BT + CT^2 + DT^3 \tag{3.16}$$

$$k_{gas} = A + BT + CT^2 + DT^3 \tag{3.17}$$

$$\rho = \frac{PM_{\omega}}{RT} \tag{3.18}$$

Binary diffusivity values are taken from Yaws [56] in which diffusivity data are available for diffusion of species of interest in air. These diffusivity data are corrected for temperature, pressure and diffusivity in hydrogen by Equation (3.19). [54]

$$\mathcal{D} = \frac{1.00 \times 10^{-7} T^{1.75} (1/M_A + 1/M_B)^{1/2}}{P[(\sum \vartheta_A)^{1/3} + (\sum \vartheta_B)^{1/3}]^2} \tag{3.19}$$

The kinetic expressions that are used to describe the hydrocracking reactions over Pt supported on amorphous silica alumina catalyst are taken from Pellegrini et.al [48]. The kinetic model considers all of the linear hydrocarbons and lumps the isomers according to their carbon number. The kinetic expressions specify activation energies and frequency factors for isomerization and cracking reactions separately. Equilibrium constants are specified for reversible isomerization reactions. An adsorption term is defined for considering the adsorption of species on catalyst surface. Total kinetic scheme of the model is presented in Figure 3.7. Rate expressions for the isomerization and cracking reactions and expressions of the terms in the equations are defined as follows [48]:

$$r_{iso-Ci} = \frac{K_{iso}(p_n(i) - p_{iso}(i)/K_{eq})}{ADSORB} \tag{3.20}$$

$$r_{cr-Ci} = \frac{K_{cr}(p_{iso}(i))}{ADSORB} \tag{3.21}$$

$$ADSORB = p_{H_2}\left[1 + \sum_{i=1}^{i=70}(K_{Ln}(i)p_n(i) + \sum_{i=4}^{i=70}(K_{Liso}(i)p_{iso}(i))\right] \tag{3.22}$$

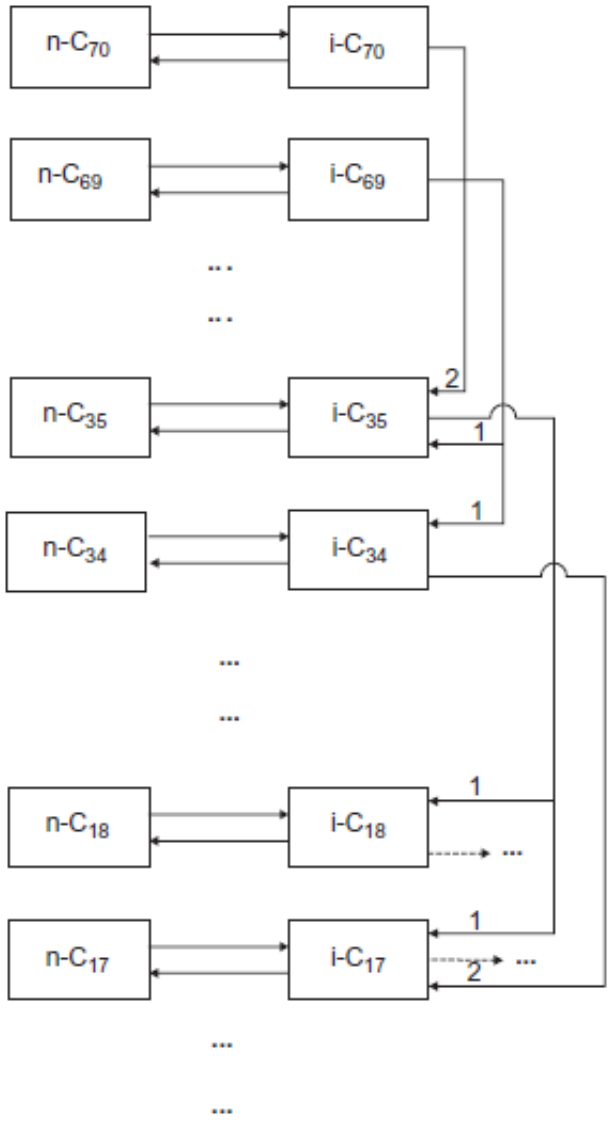

Figure 3.7. Total kinetic scheme of the model.

$$K_{iso} = k_{iso}(i)e^{-E_{iso}(i)/RT} \tag{3.23}$$

$$K_{CR} = k_{cr}(i)e^{-E_{cr}(i)/RT} \tag{3.24}$$

$$K_{Ln}(i) = 0.1e^{0.39(i)} \tag{3.25}$$

$$K_{Liso}(i) = 0.1e^{0.38(i)} \tag{3.26}$$

$$K_{eq}(i) = 1.1268(i)^2 - 3.1914(i) + 3589.1 \tag{3.27}$$

$$k_{cr}(i) = 2 \times 10^{18}(i)^{5.7677} \tag{3.28}$$

$$k_{iso}(i) = 5 \times 10^{16}(i)^{7.9241} \tag{3.29}$$

$$E_{cr}(i) = 29806Ln(i) + 86006 \tag{3.30}$$

$$E_{iso}(i) = 22253Ln(i) + 118350 \tag{3.31}$$

In order to test the rate expressions, they are implemented into 1-D pseudo homogeneous tubular reactor model which works under COMSOL Reaction Engineering Lab^{TM}. In Reaction Engineering Lab, concentration and temperature gradients are allowed only to develop in the axial direction. The species mass balances are given by Fogler [57]:

$$\frac{dF_i}{dV} = R_i \tag{3.32}$$

Adiabatic operation is required to observe the temperature profile of the system. The energy equation deployed in calculations can be given as follows [57].

$$\frac{dT}{dV} = \frac{\sum_i (-r(i))[\Delta H_{rxn,i}(T)]}{\sum_i F_i C_{P_i}} \tag{3.33}$$

Solution of the model equations is performed using the COMSOL Multiphysics^{TM}

package. COMSOL uses finite element method (FEM) to solve the partial differential equations. Stationary solver type is used since the solution is aimed to be achieved when the system approaches steady state. Whether to use a linear or non-linear solver is automatically decided by COMSOL with an analysis of the residual and the constraint Jacobian matrices. Damped Newton method is used to find the starting value of next iterative step. Solution is always carried out using linear systems, thus, nonlinear systems are linearized before the solution. For linear systems, direct UMFPACK solver is chosen. Unstructured meshing is used with 8314 triangular elements in each solution, which is obtained by applying adaptive mesh refinement to the base mesh structure to obtain solutions free from mesh structure.

In order to execute the solution, COMSOL requires initial temperature and total pressure of the system, inlet linear velocity to the channel and, for reaction channel only, initial compositions of the species. Among these, composition values should be calculated to find the corresponding values at the specified operational conditions of the system. As temperature and pressure of the feed is fixed and the molar fractions of the species are known, the concentrations (mol/ m^3) in feed stream are calculated by Equation (3.34).

$$c_{A0} = \frac{P_{A0}}{RT_0} = \frac{y_{A0}P_0}{RT_0} \tag{3.34}$$

As inlet linear velocity and the geometry of the channel are known, the volumetric flow of feed, and the inlet molar flow of species can be calculated:

$$F_{A0} = c_{A0}V_0 \tag{3.35}$$

The outlet concentration and molar flows are given at their average values via integration over the boundaries as follows.

$$\bar{v}_1 = \frac{\int v_1 dS}{\int dS} \tag{3.36}$$

$$\bar{c}_A = \frac{\int c_A \upsilon_1 dS}{\int \upsilon_1 dS} \tag{3.37}$$

$$\bar{F}_A = \bar{c}_A \bar{\upsilon}_1 S \tag{3.38}$$

Partial pressures of species are required for calculating the rate of reactions. At any point within the reaction channel, partial pressures are calculated by ideal gas assumption:

$$P_A = c_A RT \tag{3.39}$$

3.2. Parameters analyzed during simulations

In this study effects of process variables, such as weight hourly space velocity (WHSV) (kgwax/kgcat.h), reactant and coolant feed temperatures, reactant feed pressure, H_2-to-wax ratio at the inlet and type of wall material on the jet fuel mole fraction (hydrocarbons with carbon number ranging from 11 to 18 including linear and isomerized hydrocarbons,C_{18}-C_{22}), diesel fuel mole fraction (hydrocarbons with carbon number ranging from 19 to 22 including normal and isomerized hydrocarbons,C_{19}-C_{22}), mole fraction of heavy hydrocarbons (hydrocarbons with carbon number higher than 22 including normal and isomerized hydrocarbons,C_{22+}), isomer to normal ratio (molar ratio of isomerized hydrocarbons to normal hydrocarbons) and conversion of normal hydrocarbons more than 22 carbon atoms (nC_{22+}) are investigated. Values of the constant properties and ranges of variable properties are given in Table 3.5. Inlet velocity of reactant stream is calculated according to feed temperature, pressure and residence time assuming the stream is ideal gas by Equation (3.40).

$$\upsilon = \frac{V}{A_c} = \frac{nRT}{PA_c} \tag{3.40}$$

Table 3.5. Values of constant properties and ranges of variable properties.

Reactant feed temperature, °C	440-460
Reactant stream pressure, bar	41.25-60
WHSV, kgwax/kgcat.h	100-220
Coolant feed temperature, °C	300-390
Coolant stream pressure, bar	30
Coolant inlet velocity, m/s	0.05
H_2/Wax Ratio, kg H_2/kg wax	0.06-0.15
Type of wall material	Steel -AISI, Alumina (Al_2O_3), Silicon Carbide

In order to carry out parametric analysis, the required base configurations are determined according to maximum yields of diesel fraction (C_{19}-C_{22}) and jet fraction (C_{11}-C_{18}). Parametric analysis is then conducted by changing a single variable within the ranges specified in Table 3.5, while keeping the others constant as given in Tables 3.6 and 3.7 Then effect of residence time and wall material type on the profiles of jet fuel fraction , diesel fuel fraction , heavy fraction (C_{22+}), isomer to normal ratio, reaction channel temperature, coolant channel temperature and conversion of (nC_{22+}) along reactor are investigated.

Table 3.6. Configurations for the jet fuel base.

Reactant feed temperature	460°C
Reactant stream pressure	53.75 bar
WHSV	160 kgwax/kgcat.h
Coolant feed temperature	390°C
Coolant stream pressure	30 bar
Coolant inlet velocity	0.05 m/s
H_2/Wax Ratio	0.1275 kg H_2/kg wax

Table 3.7. Configurations for the diesel fuel base.

Reactant feed temperature	450°C
Reactant stream pressure	53.75 bar
WHSV	220 kgwax/kgcat.h
Coolant feed temperature	300°C
Coolant stream pressure	30 bar
Coolant inlet velocity	0.05 m/s
H_2/Wax Ratio	0.1275 kg H_2/kg wax

Table 3.8. Properties of wall materials.

Material	**Thermal Conductivity k, W/(m.K)**	**Density kg/m^3**	**Heat Capacity J/(kg.K)**
Steel-AISI	44.5	7850	475
Alumina (Al_2O_3)	27	3900	900
Silicon Carbide	87	3160	1135

4. RESULTS AND DISCUSSION

The reaction mechanism of the hydrocracking reactions are first tested in simple 1D pseudo-homogeneous model by using MATLAB^{TM} and COMSOL Reaction Engineering Lab packages. Then after this step FEM-based simulations and the parametric analysis of system defined in Section 3.2 previously is carried out using COMSOL Multiphysics^{TM} package. The simulations are done with the feedstock specified in Figure 3.4. Feedstock contains only linear paraffins up to hydrocarbons with 70 carbon atoms and excess amounts of hydrogen in the molar basis.

Nature of the process should be understood well before starting any calculations on this process. 1D pseudo-homogeneous model simulations of the process with the reaction scheme shown in Figure 3.3 are performed with MATLAB^{TM} and COMSOL Reaction Engineering Lab under adiabatic conditions to see the behavior of the system without temperature control. Temperature and molar fractions of jet fuel cut (C_{11}-C_{18}), diesel fuel cut (C_{19}-C_{22}) and heavy cut (C_{22+}) are shown in Figure 4.1 and Figure 4.2 respectively. Molar fractions of species at the feedstock and at the product are shown with respect to carbon number in Figure 4.3.

As it can be seen from Figure 4.1 reactions are highly sensitive to temperature such that temperature of the system increases from 460°C to 473° in the first 60% of the reactor and reaches to 670°C and complete conversion from 60% to 70% of the reactor. This situation shows that even under operation with cooling, system can suffer from a thermal runaway in case of a hot spot formation since exothermic nature of reactions cause a chain effect resulting at undesired conversion values. Figure 4.2 is showing the profiles of investigated cuts which deplete with the sudden increase of temperature. Figure 4.3 is showing that as a result of the thermal runaway all of the feedstock becomes gaseous products instead of products in the desired (C_{11} to C_{22}) range.

The process is simulated under adiabatic conditions with lower residence time,

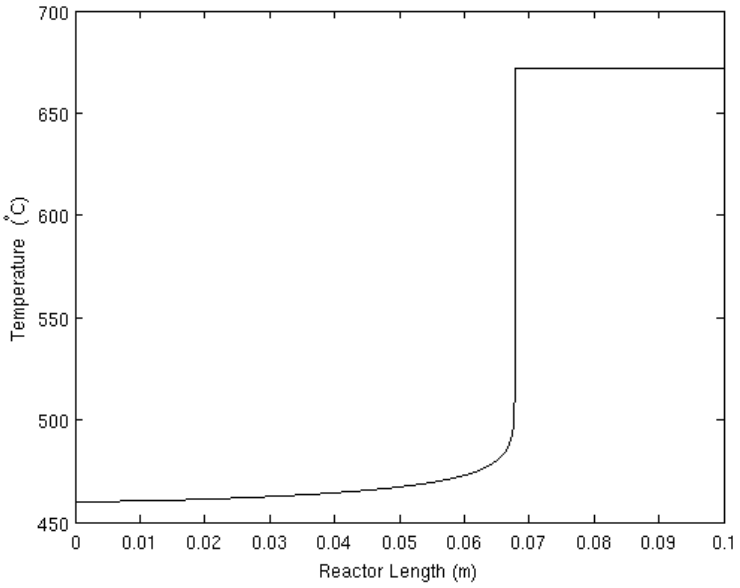

Figure 4.1. Temperature profile along reactor length under adiabatic conditions with complete conversion (WHSV:160 h^{-1} Feed T: 460°C P:53.75 bar and H_2/Wax:0.1275).

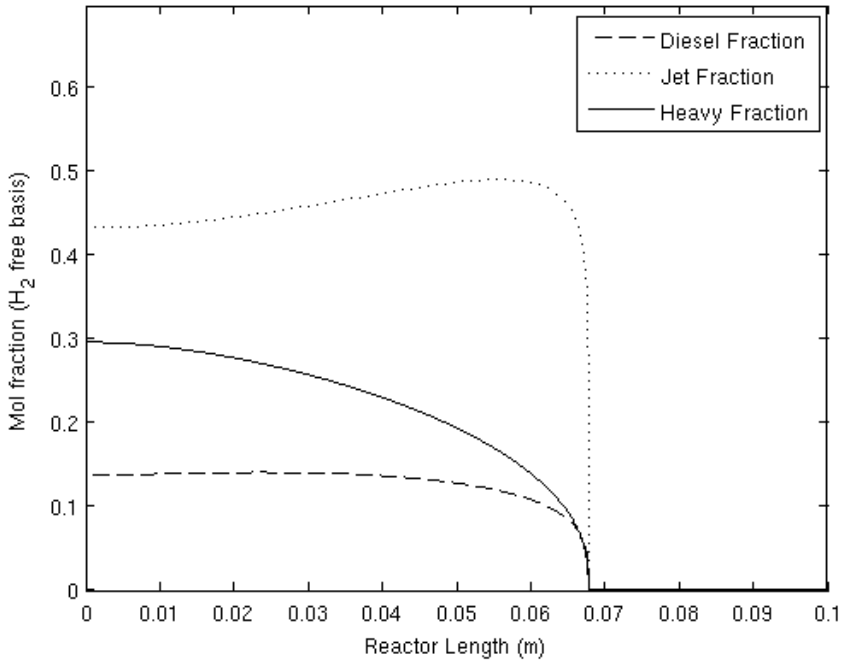

Figure 4.2. Profiles of jet, diesel and heavy cuts along reactor length under adiabatic conditions with complete conversion (WHSV:160 h^{-1} Feed T: 460°C P:53.75 bar and H_2/Wax:0.1275).

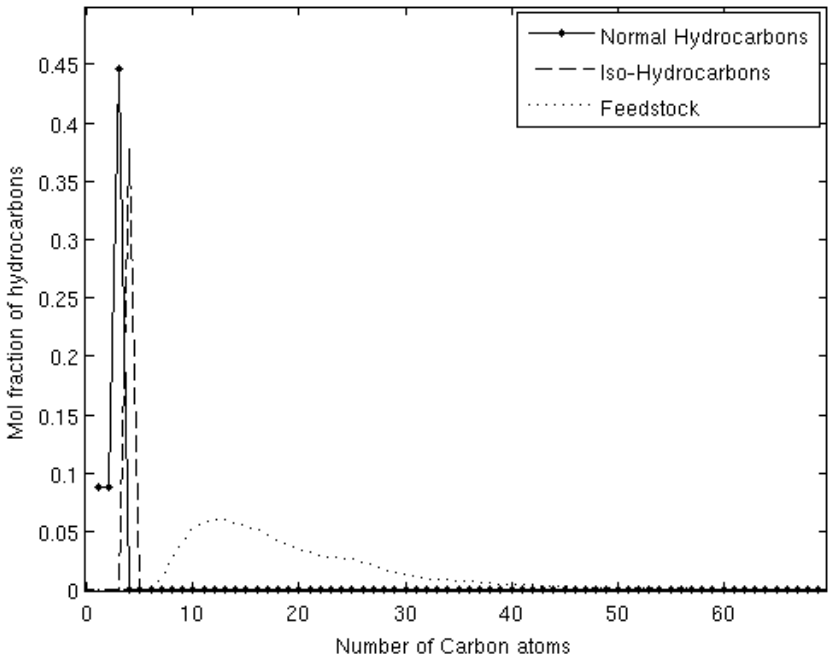

Figure 4.3. Feedstock and product compositions under adiabatic conditions with complete conversion (WHSV:160 h^{-1} Feed T: 460°C P:53.75 bar and H_2/Wax:0.1275).

reciprocal of WHSV, (WHSV:250 h^{-1} instead of 160 h^{-1}) for investigating the profiles of temperature and molar fractions of the pertinent cuts at lower conversion levels. The results are given in Figures 4.4-4.6.

Figure 4.4 shows the temperature profile along the reactor as it can be seen from the figure temperature change is limited in this case, 18°C, compared to the case of 160 h^{-1} WHSV, 210°C. Temperature profile in this case also have an increasing slope with respect to reactor length which implies the possibility of thermal runaway with further conversion as in the case of 160 h^{-1} WHSV and shows importance of temperature control for hydrocracking process.

Figure 4.5 shows the profiles of molar fractions of diesel, jet and heavy cuts along the reactor for an adiabatic operation. As it is seen from the figure, molar fraction of the heavy cut which is aimed to be cracked decreases, diesel cut mole fraction, slightly increases at first and then decreases with the extent of the reaction and the jet fuel cut mole fraction increases up to a certain point and then decreases with

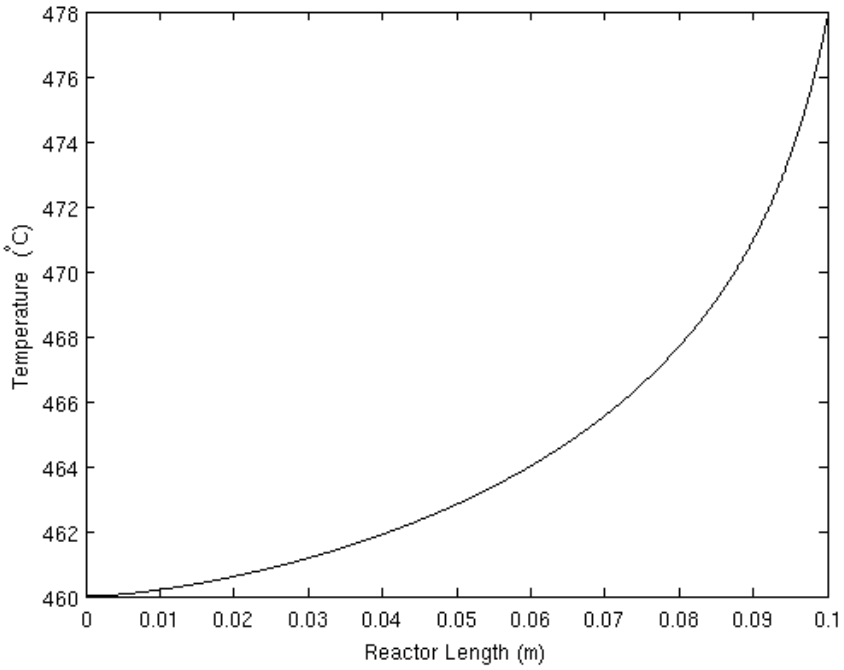

Figure 4.4. Temperature profile along reactor length under adiabatic conditions (WHSV:250 h^{-1} Feed T: 460°C P:53.75 bar and H_2/Wax:0.1275).

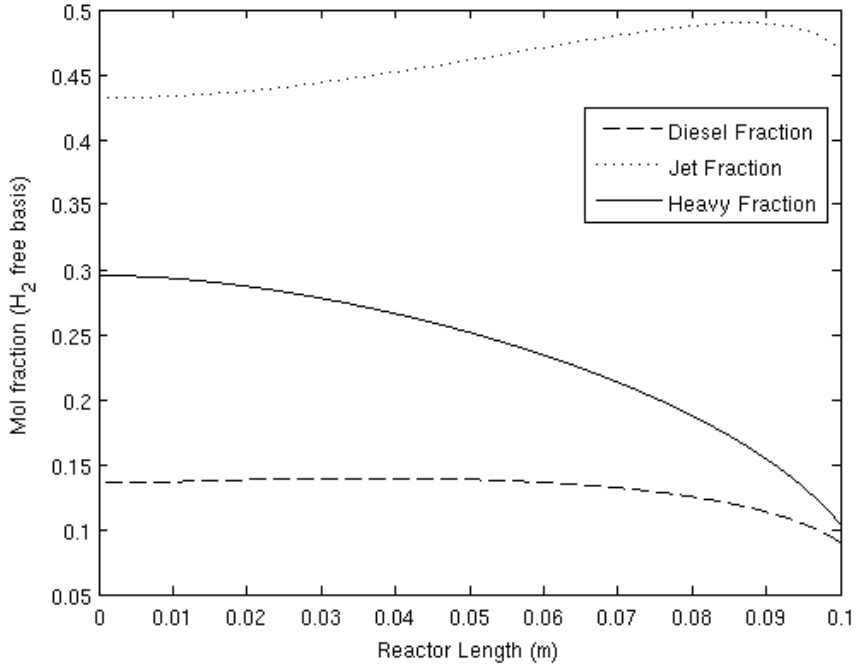

Figure 4.5. Profile of jet, diesel and heavy cuts along reactor length under adiabatic conditions (WHSV:250 h^{-1} Feed T: 460°C P:53.75 bar and H_2/Wax:0.1275).

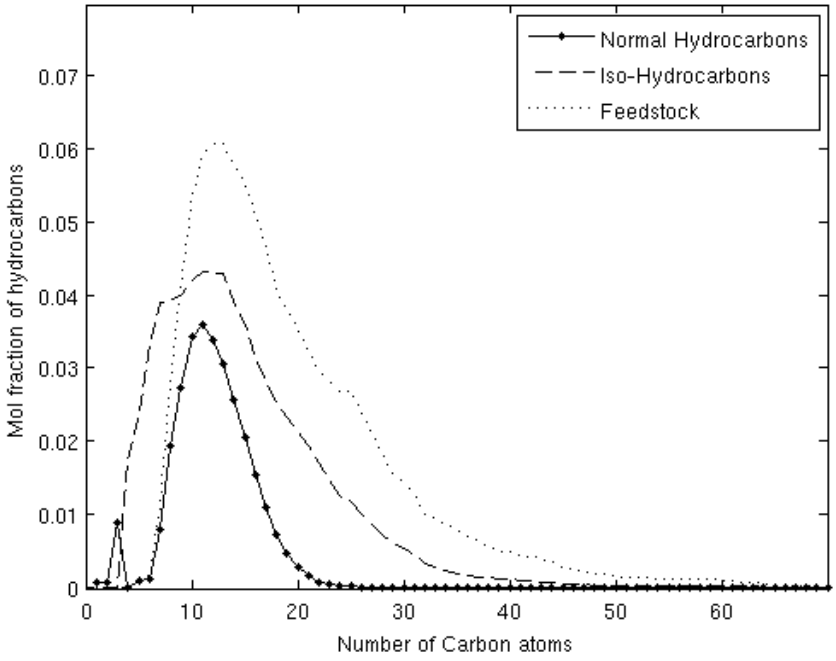

Figure 4.6. Feedstock and product compositions under adiabatic conditions (WHSV:250 h^{-1} Feed T: 460°C P:53.75 bar and H_2/Wax:0.1275).

further conversion. These profiles show that jet fuel cut and diesel fuel cut behave like intermediate products in the system. Therefore, the system should be configured for maximizing the mole fractions of the desired products.

Figure 4.6 gives the composition of the product stream and feedstock with respect to number carbon atoms. As it is seen from the figure, hydrocracking increases the amount of isomerized hydrocarbons significantly which is crucial for improving the cold flow properties of FT wax. It is also shown that hydrocracking process decreases the fraction of heavy hydrocarbons and increases the concentration of the desired products significantly, such that hydrocarbons with more than 40 carbon atoms almost diminishes and around 60% of the heavy hydrocarbons is converted to lighter hydrocarbons.

4.1. Effect of reactant and coolant feed temperatures and residence time on wax hydrocracking

In this section effects of reactant and coolant feed temperatures and residence time on the outputs of jet, diesel and heavy fractions, conversion of C_{22+} normal hydrocarbons and isomer-to-normal paraffin ratio are investigated.

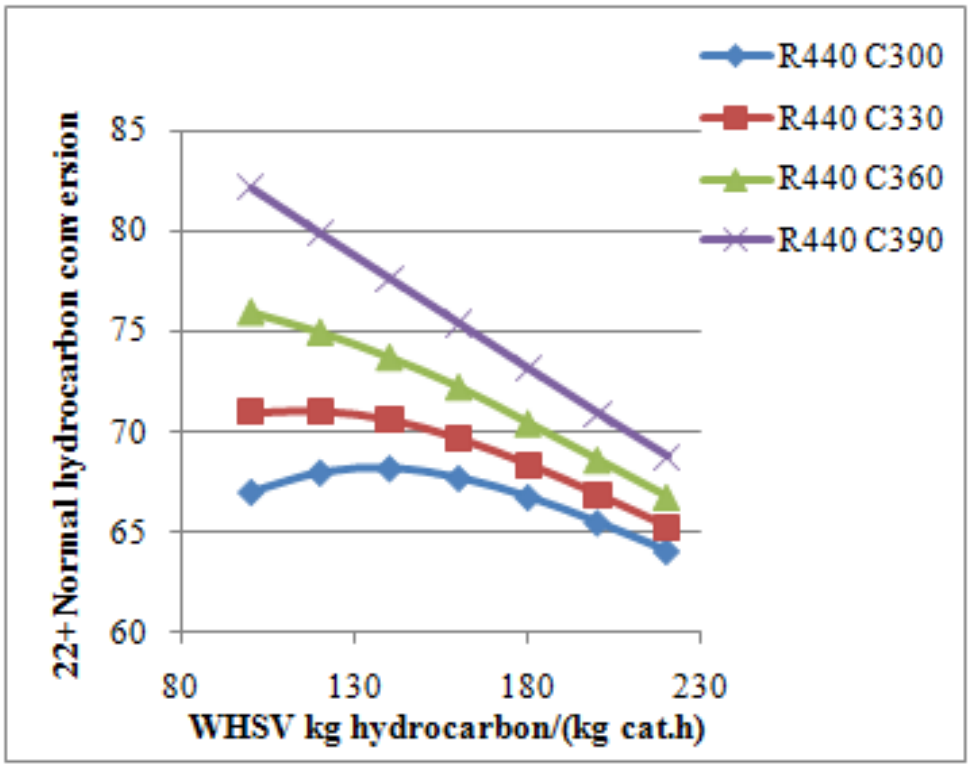

Figure 4.7. 22+ n-hydrocarbon conversions at 440°C.

Figures 4.7 to 4.9 shows the conversion values at the reaction channel outlet with respect to WHSV and coolant feed temperatures varying from 100 h^{-1} to 220 h^{-1} and from 300°C to 390°C respectively. It is observed from figures that reactant and coolant feed temperatures positively affect the conversion values due to kinetic reasons; for the feed temperature of 440°C conversion values varies between 64% to 85%, for the feed temperature of 450°C conversion values varies between 77% to 93% and for the feed temperature of 460°C conversion values varies between 90% to 99% . The results also show that conversion values are affected from WHSV values in a different manner than expected, especially at values lower than 140 h^{-1}. For the WHSV values from 220 h^{-1} to 140 h^{-1} conversion is positively affected from the residence

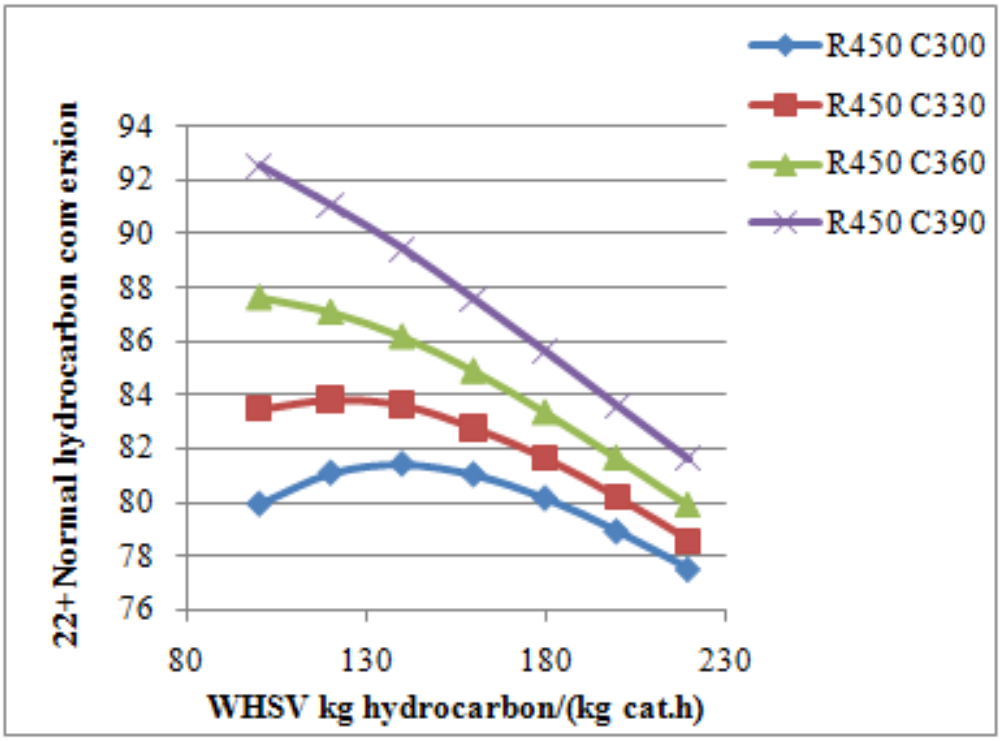

Figure 4.8. 22+ n-hydrocarbon conversions at 450°C.

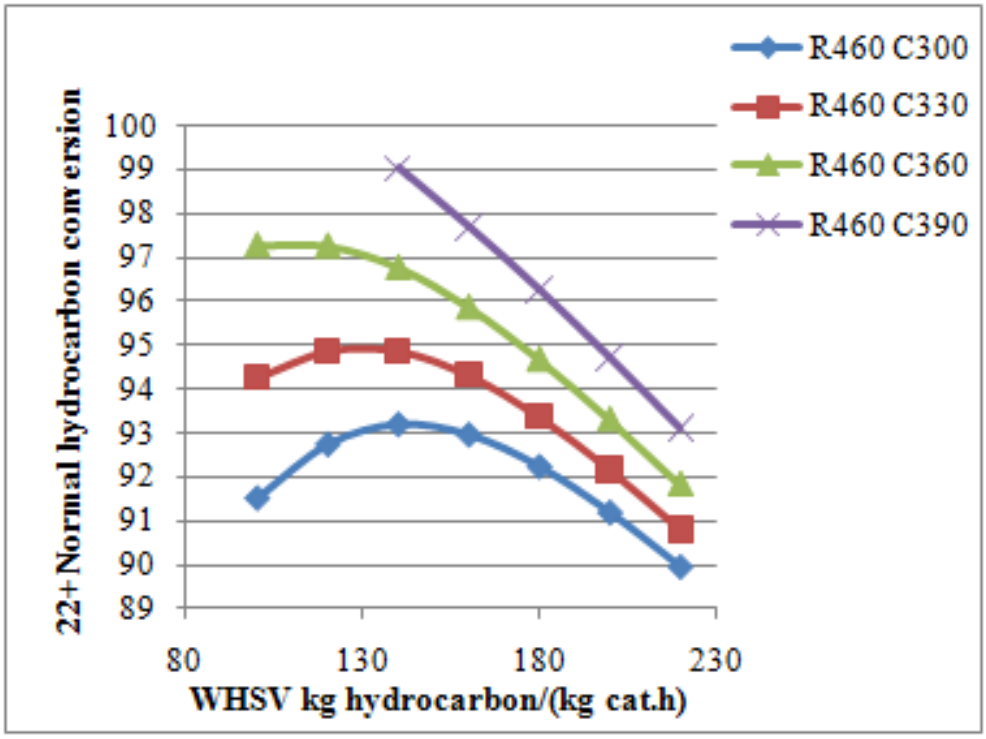

Figure 4.9. 22+ n-hydrocarbon conversions at 460°C.

time as expected. However for WHSV values from 140 h^{-1} to 100 h^{-1} conversion values are decreasing at coolant feed temperatures of 300°C and 330°C. This situation can be explained by the over cooling of the system. Energy entering the system with reactant feed decreases with WHSV while the amount of coolant stream flowing is kept constant which causes unwanted temperature decreases in the reaction channel and also lowers the heat released by the reactions. For coolant feed temperatures of 360°C and 390°C temperature in the reaction channel stays high enough to proceed the reactions. Conversion values keep on increasing with decreasing WHSV values, but slight decreases in the slopes of the conversion profiles are observed, which indicates that the overcooling still affects the process. These figures also indicate the strong dependence of the process on temperature.

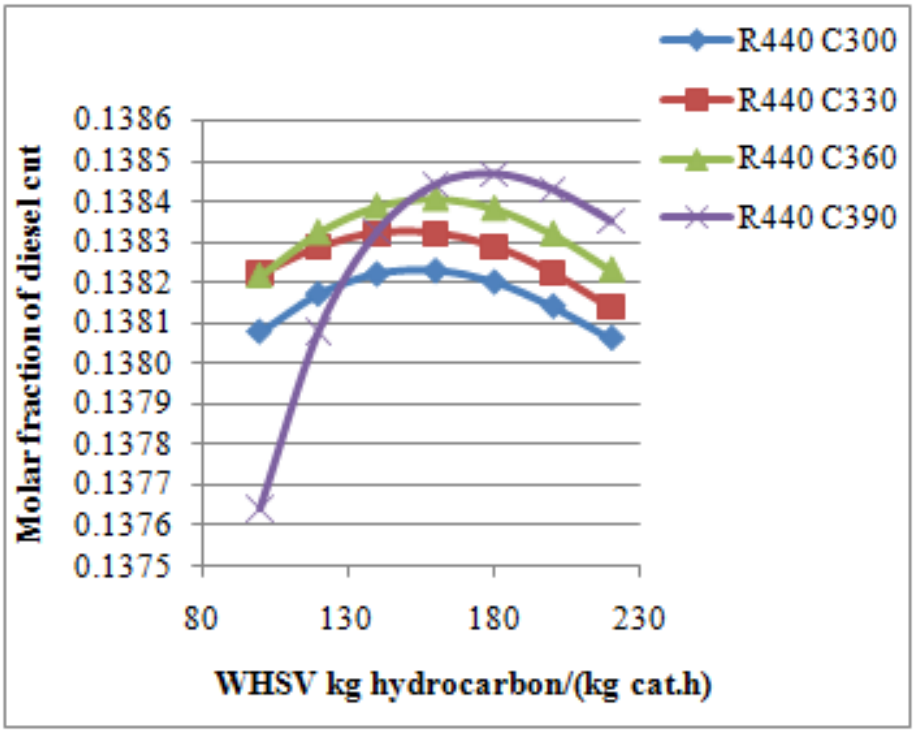

Figure 4.10. Molar fraction of diesel cut at 440°C.

Responses of diesel fuel cut (C_{19} - C_{22}) molar fraction at reactor outlet on process variables are shown in Figures 4.10-4.12. The results show that diesel cut yields show two different profiles at 440°C reactant feed temperature in which conversion values are lower than 75% and at 450°C and 460°C reactant feed temperatures in which conversion values are higher than 75% as it can be seen in Figures 4.7-4.9. Up to conversion values of 75%, which is the conversion value corresponding to maximum

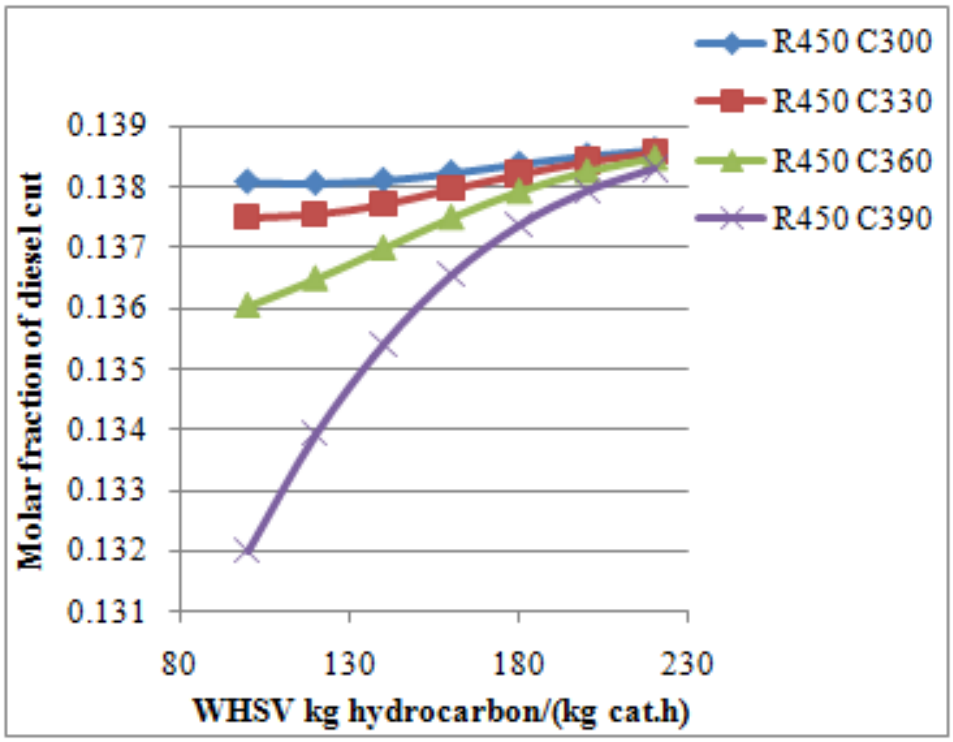

Figure 4.11. Molar fraction of diesel cut at 450°C.

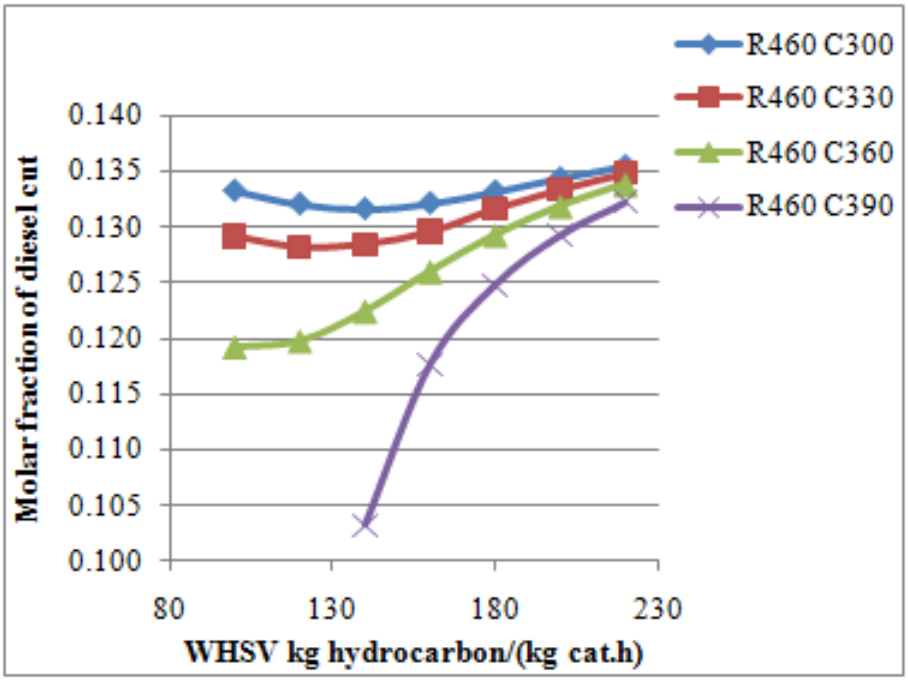

Figure 4.12. Molar fraction of diesel cut at 460°C.

diesel cut molar fraction, fraction of diesel cut increases and after 75% conversion further proceeding of the reaction decreases fraction of the diesel cut. Figure 4.11 and 4.12 are showing conditions with more than 75% conversion and yield of diesel fraction shows an inverse relationship with temperature and positive relationship with WHSV since at these conversion levels molar fraction of diesel cut exceeds its maximum value and starts to decrease with further conversion.

Figure 4.10 shows the two different profiles of the diesel cut fraction. Coolant feed temperatures of 300°C and 330°C give conversion values lower than 75% (Figure 4.7) and diesel cut fraction shows parallel relation with conversion in a manner that with the increase of coolant temperature both conversion and diesel fraction increases and at lower WHSV values diesel fraction and conversion decreases as a result of overcooling. At coolant feed temperatures of 360°C and 390°C conversion values varies around 75% and shows the two profiles, i.e: in the case of 390°C coolant feed temperature, for WHSV values from 220 h^{-1} to 180 h^{-1} conversion values are lower 75% and diesel fraction is increasing with decreasing WHSV values, for WHSV values from 180 h^{-1} to 100 h^{-1} conversion values are exceeding 75% and fraction of diesel cut is decreasing with the extent of reaction with decreasing WHSV values.

The results presented in Figure 4.12 show that 460°C is not suitable for enhancing the diesel yield since molar fraction of diesel cut is lower than the fraction at the inlet value, 0.135. In the cases of 440°C and 450°C, however, yields of diesel fuel cut are slightly higher than input value except the cases with high conversion like 390°C coolant feed temperature and WHSV of 100 h^{-1}. The maximum diesel fuel cut yield occurs at 450°C reactant and 300°C coolant feed temperatures and 220 h^{-1} WHSV with 0.1386 molar fraction.

Figures 4.13-4.15 shows the response of jet fuel cut (C_{11} - C_{18}) molar fraction at reactor outlet, which are directly related to conversion values given in Figures 4.7-4.9. As in the case of diesel cut molar fraction, jet fuel cut behaves like an intermediate product. In the cases of 440°C and 450 °C reactant feed temperatures molar fraction of jet fuel cut increases with increasing both reactant and coolant feed temperatures,

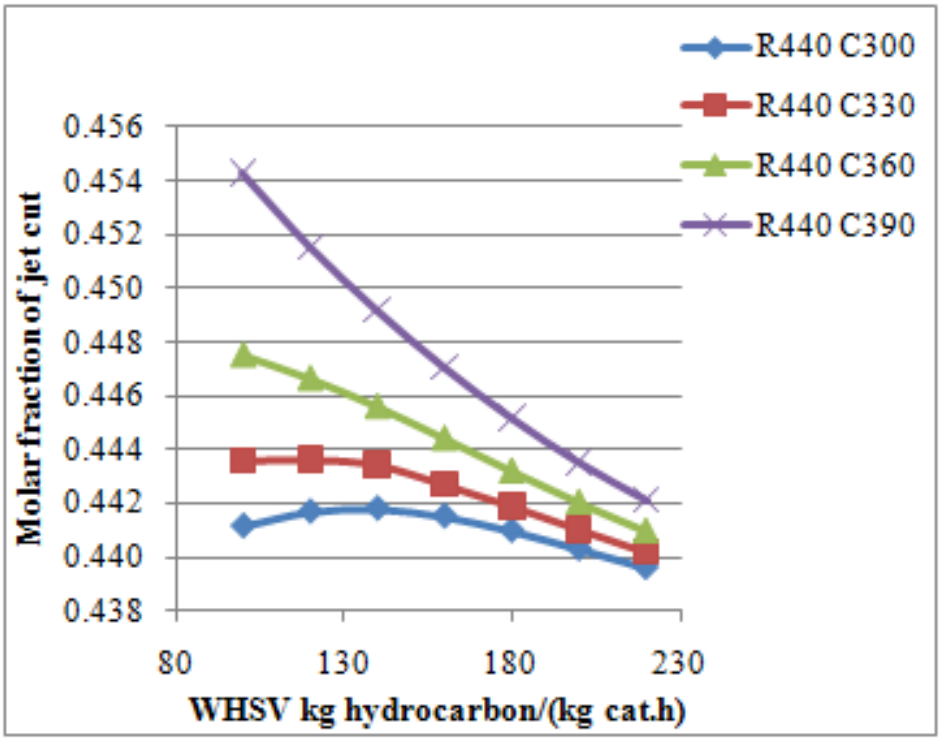

Figure 4.13. Molar fraction of jet fuel cut at at 440°C.

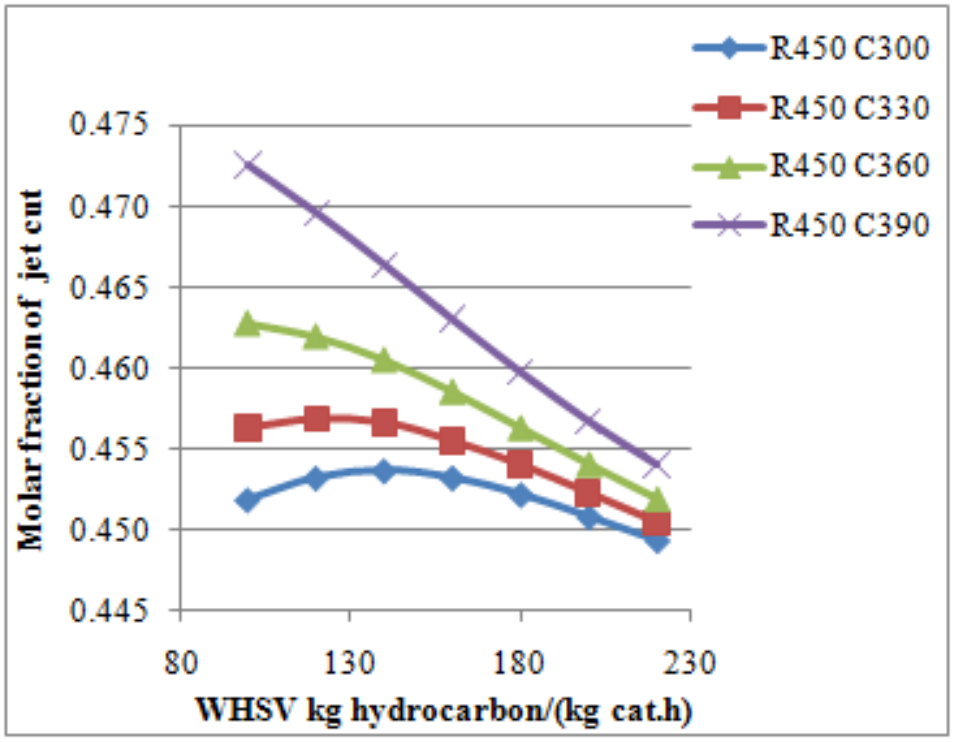

Figure 4.14. Molar fraction of jet fuel cut at 450°C.

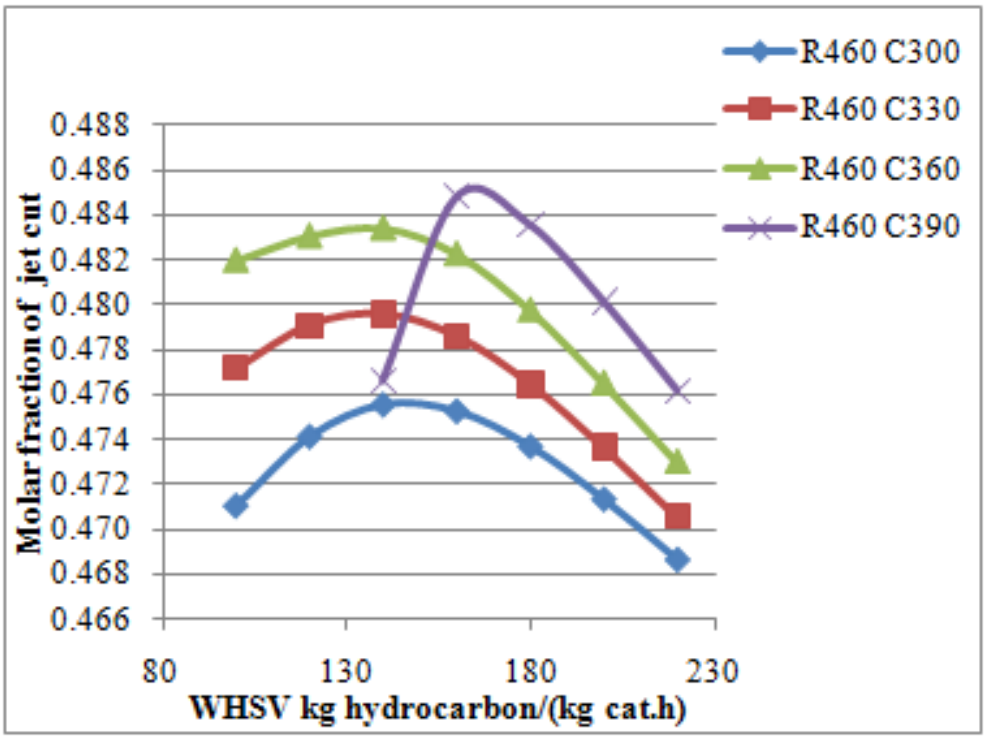

Figure 4.15. Molar fraction of jet fuel cut at 460°C.

in which conversion values are lower than 96% corresponding to maximum jet fuel cut molar fraction. In the cases of 300°C and 330°C coolant feed temperatures for WHSV values of 140 h^{-1} to 220 h^{-1}, molar fraction of jet fuel cut increases with decreasing WHSV values and for WHSV values of 100 h^{-1} to 140 h^{-1}, decreases with increasing WHSV values due to overcooling in the reaction channel which also occurs in conversion values. However, in the cases of 360°C and 390 °C overcooling effect is not obvious as much as 300°C and 330°C cases but it still affects the molar fraction of jet fuel cut by decreasing its slope with respect to decreasing WHSV value.

Figure 4.15 shows the effect of WHSV and coolant feed temperature at 460°C reactant feed temperature, in the cases of 300°C and 330°C coolant feeds conversion values do not reach 96% (Figure 4.9) and molar fraction of jet fuel cut behaves similar to conversion, increases with temperature and increases with residence time at high WHSV values and decreases at low WHSV values due to over cooling of system. In the cases of 360°C and 390°C coolant feed temperatures conversion values reaches 96% at 140 h^{-1} and 160 h^{-1} respectively and fraction of jet fuel cut decreases with increasing residence time even though the conversion is increasing since after cracking the fractions

heavier than jet fuel cut, the process starts to crack hydrocarbons in the jet fuel range.

Considering the fact that fraction of the jet fuel cut is around 0.43 at the reactor inlet, hydrocracking process increase the fraction of jet fuel cut in all of the investigated cases. As it can be seen from Figures 4.13-4.15 molar fraction of the jet fuel cut is around 0.45, 0.46 and 0.48 for 440°C, 450°C and 460°C reactant feed temperatures, respectively. Except for the cases with conversions higher than 96%, 460°C reactant feed gives higher jet fuel fractions compared to the 450°C and 440°C cases. The maximum jet fuel cut yield occurs at 460°C reactant and 390°C coolant feed temperatures and 160 h^{-1} WHSV with 0.485 molar fraction.

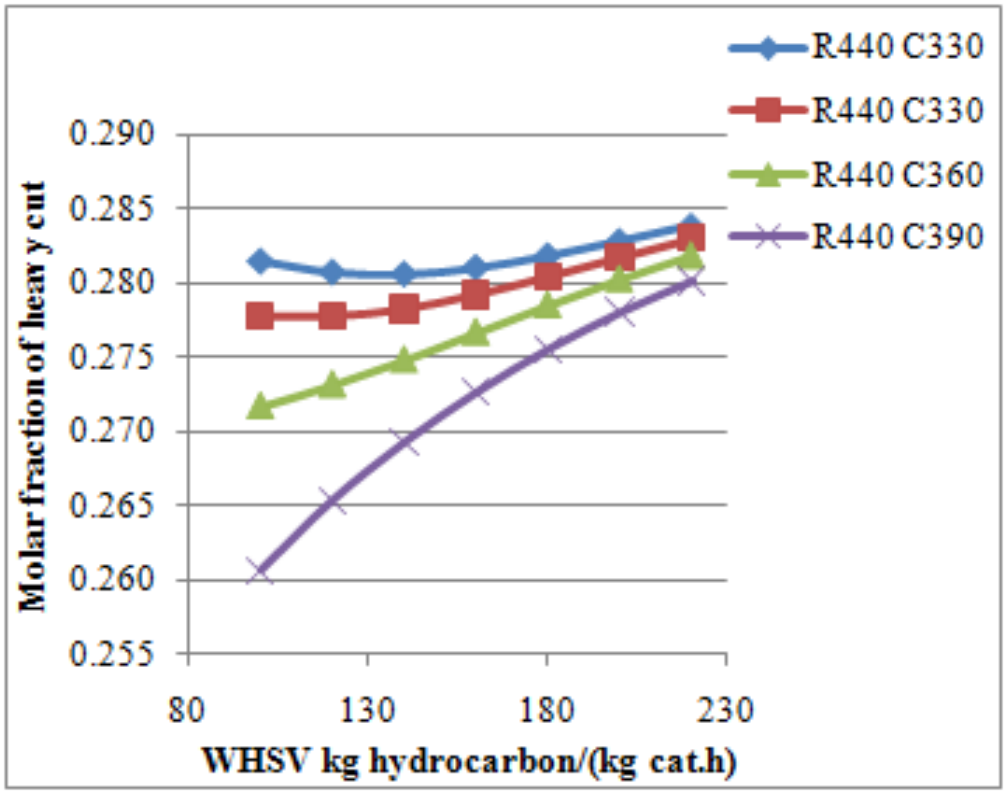

Figure 4.16. Molar fraction of heavy cut at 440°C.

Effect of process variables on the heavy cut fraction (C_{22+}) at reactor outlet are shown in Figures 4.16, 4.17 and 4.18. Heavy cut fraction is the heaviest fraction in the reaction mixture and behaves like raw material in the process. As a result molar fraction of this cut always decreases with proceeding of the reaction until depletion of the fraction. As it can be seen by comparing the Figures 4.16 and 4.17 with Figures

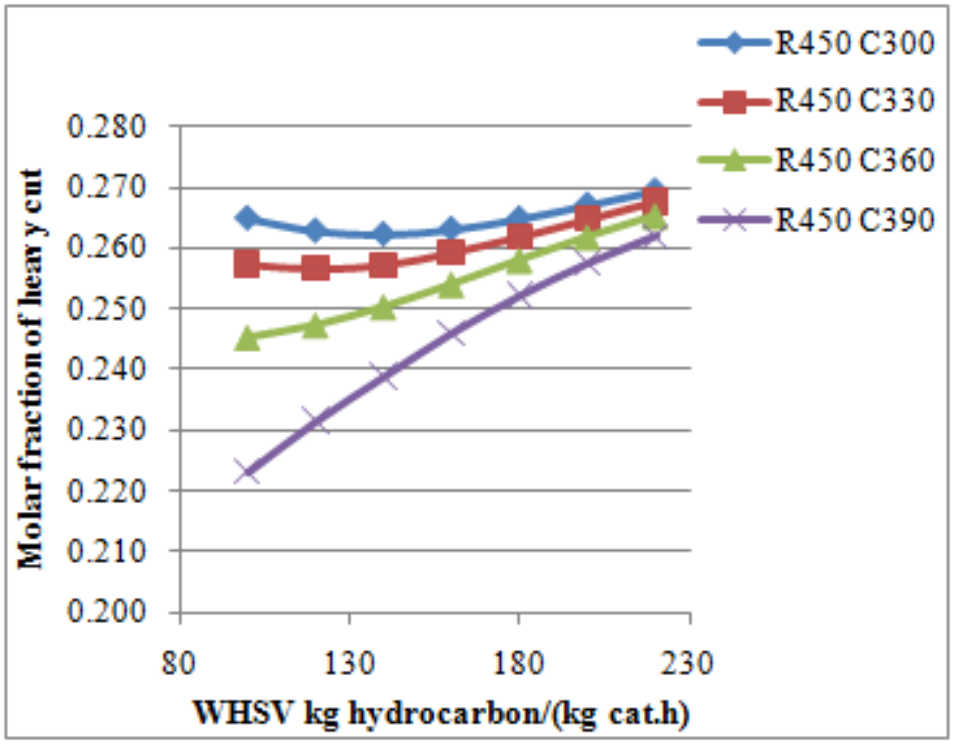

Figure 4.17. Molar fraction of heavy cut at 450°C.

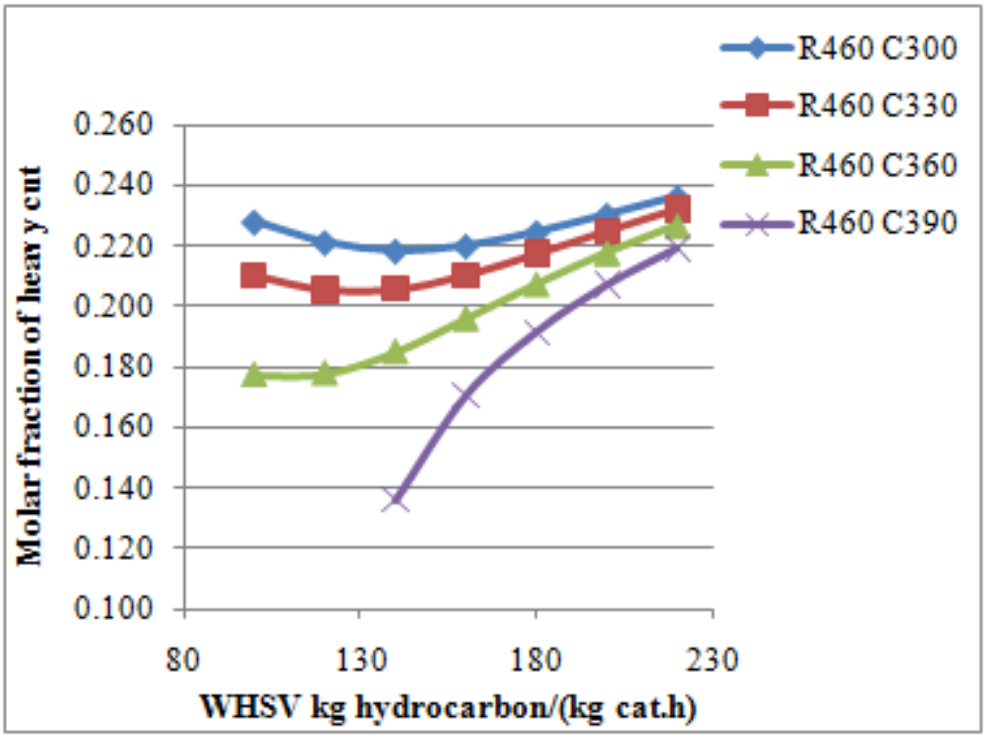

Figure 4.18. Molar fraction of heavy cut at at 460°C.

4.7 to 4.9, fraction of heavy cut at reactor outlet shows a reverse relationship with conversion such that higher feed and coolant temperatures causes lower values of heavy cut at outlet. At higher residence times between 140 h^{-1} to 220 h^{-1} fraction of heavy cut decreases, and further increasing the residence time causes higher heavy cut fractions as a result of overcooling in the system, especially at coolant feed temperatures of 300°C and 330°C.

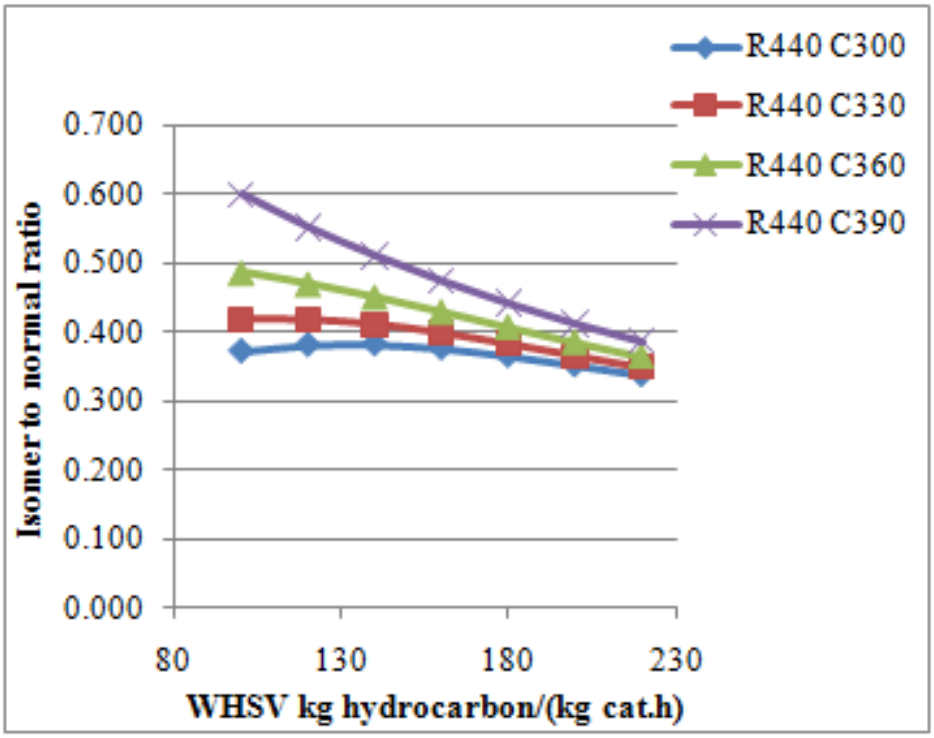

Figure 4.19. Molar fraction of isomer to normal hydrocarbon ratio at 440°C.

Figures 4.19, 4.20 and 4.21 are showing the variations of the isomer-to-normal paraffin ratio in the reaction channel with respect to reactant and coolant feed temperatures and WHSV. The results show that isomer-to-normal paraffin ratio is related to conversion values and always increase with conversion within the investigated range. Isomer to normal paraffin ratios are around 0.5, 0.75 and 1.5 for the cases of 440°C, 450°C and 460°C reactant feed temperatures.

Figure 4.22 shows the relation between the conversion and isomer to normal hydrocarbon ratio. As it can be seen from the figure, there is an exponential relationship between them. The exponential relationship can be explained by two reasons. First reason is based on the kinetic model which states that the equilibrium constants for

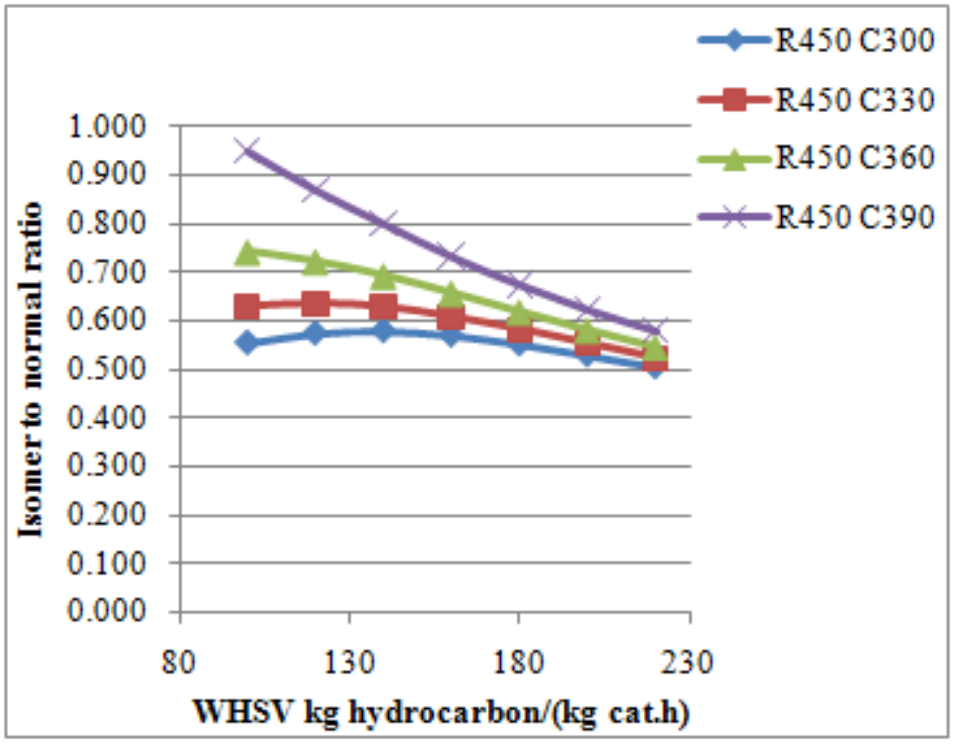

Figure 4.20. Molar fraction of isomer to normal hydrocarbon ratio at 450°C.

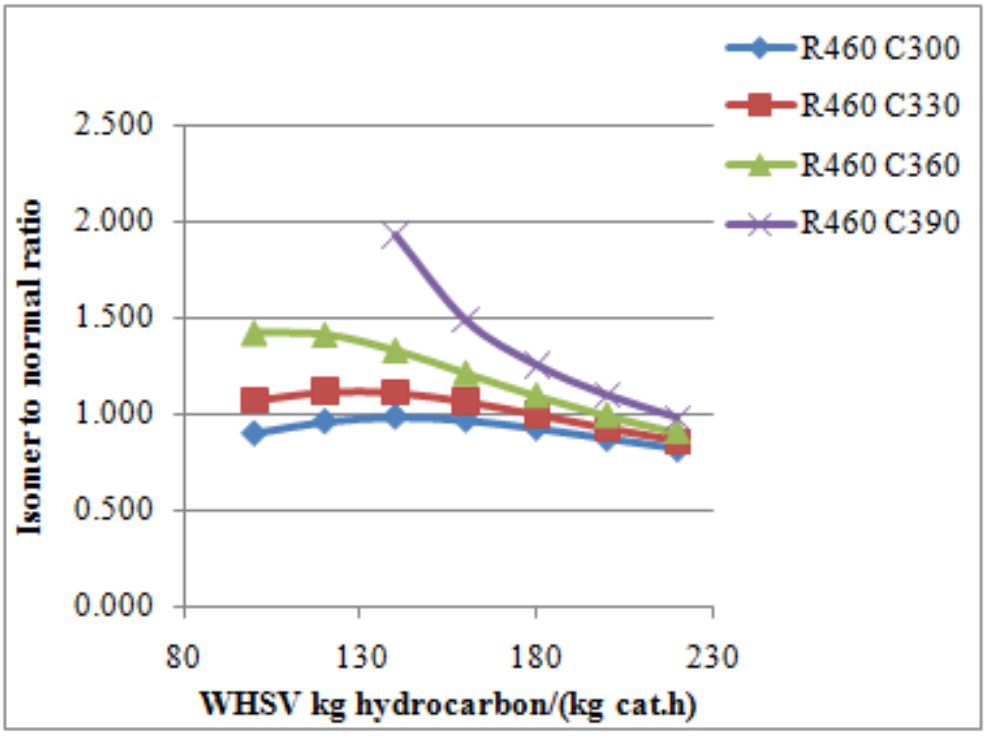

Figure 4.21. Molar fraction of isomer-to-normal hydrocarbon ratio cut at 460°C.

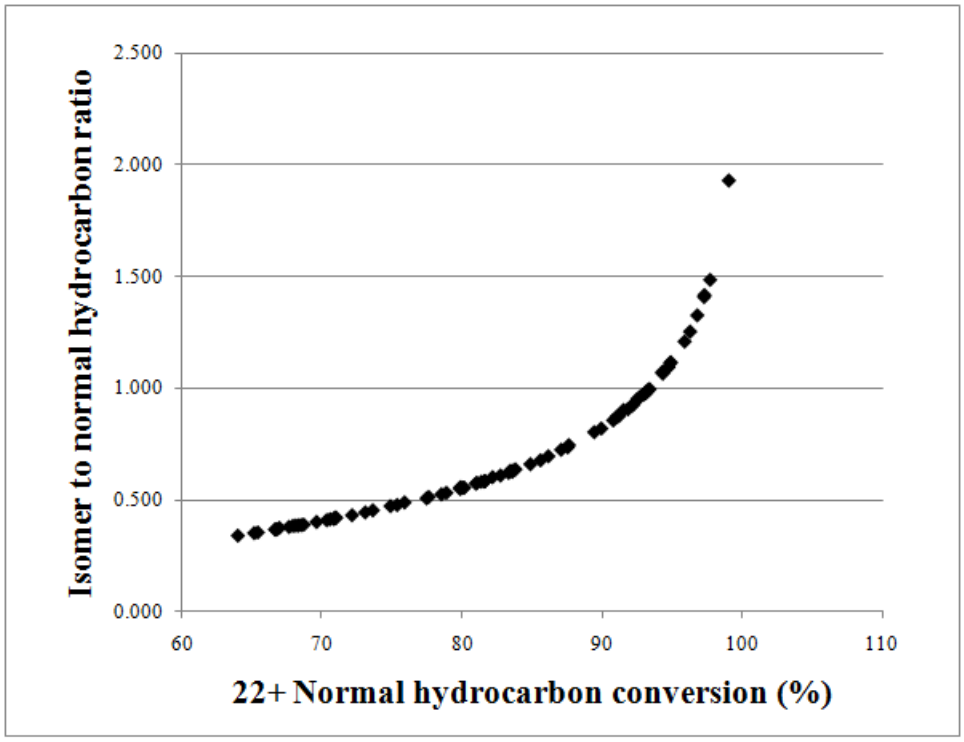

Figure 4.22. Isomer-to-normal paraffin ratio at reactor outlet vs corresponding conversion.

the reversible isomerization reaction are much higher than 1, and are around 4000 for C_4 to C_{30} range. As a result reversible isomerization reactions do not reach equilibrium and the cracking reactions give two isomerized molecules while cracking one isomerized molecule, therefore, proceeding of the process always increase the isomer-to-normal hydrocarbon ratio. Second reason of the exponential increase is related to the definition of conversion which is only considering the change in the C_{22+} normal hydrocarbons. So even if the conversion value reaches 100% process still continues cracking and increases the isomer ratio while conversion value does not change.

4.2. Effect of wall material at jet and diesel fuel base configuration on wax hydrocracking

In this section profiles of jet fuel cut, diesel fuel cut, heavy cut, conversion, isomer-to-normal paraffin ratio and reaction channel temperature along the reactor are given at jet fuel base configuration (Table 3.6) and effect of wall material type on these properties are investigated. Jet fuel base configuration is defined as the combination

of operating and reactor parameters that gives maximum mole fraction of jet cut. As it is seen in Figure 4.15 maximum yield of jet cut occurs at 460°C reactant and 390°C coolant feed temperatures with 160 h^{-1} WHSV. In order to investigate the effect of wall material with lower thermal conductivity values without risk of thermal runaway, WHSV is taken as 180 h^{-1} for jet fuel base configuration in this section although 160 h^{-1} is giving a slightly higher yield.

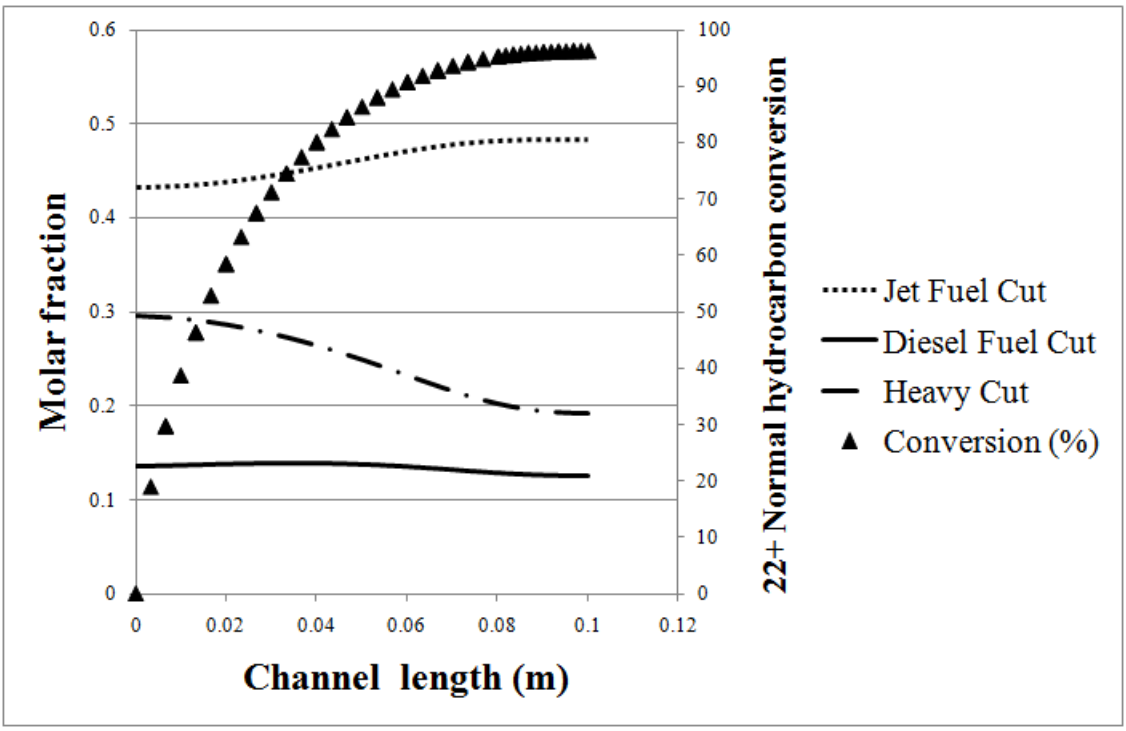

Figure 4.23. Jet fuel, diesel fuel, heavy cut and conversion of 22+ n-hydrocarbon profiles along reaction channel at jet base configuration.

Figure 4.23 shows the profiles of jet fuel, diesel fuel and heavy cuts in primary axis and conversion of C_{22+} normal hydrocarbons in the secondary axis along the reaction channel. As it is seen from the figure fraction of jet fuel cut increases from 43% to 49% with the cracking process while fraction of diesel cut slightly decreases to 12.5% after reaching a maximum of 13.5% and fraction of heavy cut decreases from 30% to below below 20%. Profiles of the jet fuel, diesel and heavy cuts show that hydrocracking process cracks the unwanted heavy fraction while keeping the desired product levels as much as possible which is one of the objectives stated in Section 2.2.2.

Figure 4.24 and Figure 4.25 present the temperature profiles of reaction and

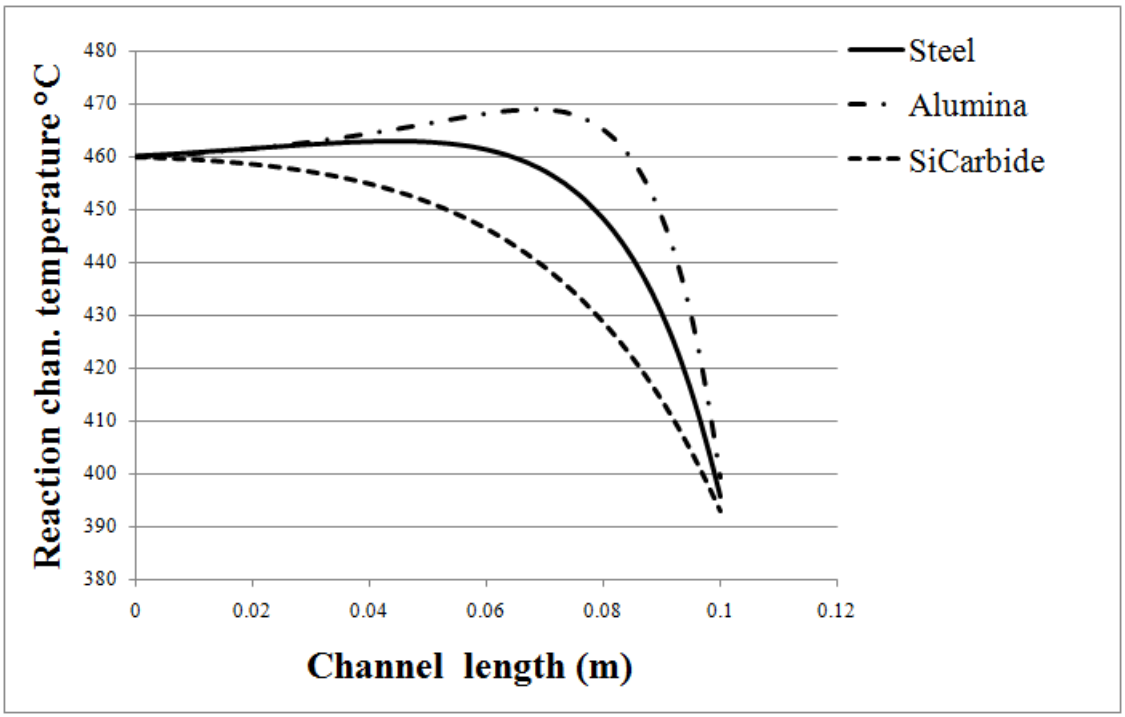

Figure 4.24. Temperature profile along reaction channel with different wall materials.

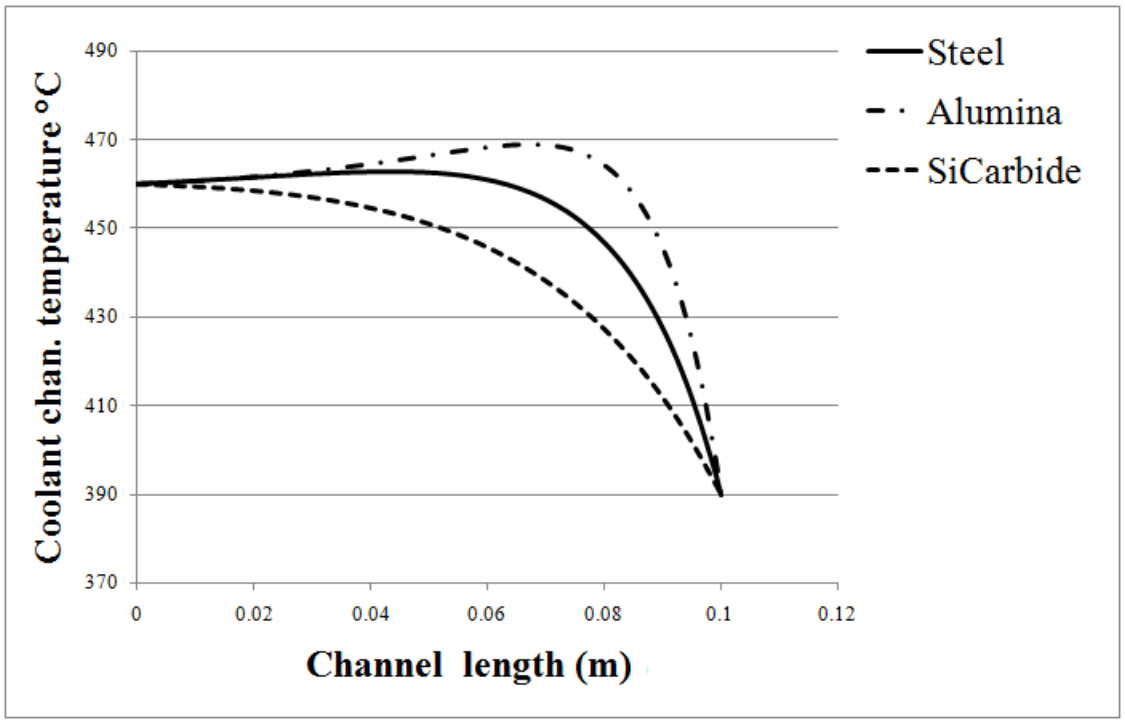

Figure 4.25. Temperature profile of along cooling channel with different wall materials.

cooling channels, respectively. The results show that the use of alumina wall causes higher temperatures in both reaction and cooling channels and use of silicon carbide wall causes lower temperatures in both channels in contrast to alumina wall. In the case of alumina wall, highest temperature observed is 470°C, while 463°C and 460°C are the highest temperatures observed with stainless steel wall and silicon carbide wall, respectively. This situation is related to the thermal conductivity of the wall materials. As stated in Table 3.8 silicon carbide wall has the highest thermal conductivity and alumina has the lowest thermal conductivity values among the investigated material types with 87 W/(m.K) and 27 W/(m.K), respectively, while thermal conductivity of stainless steel wall is 44.5 W/(m.K).

In the case silicon carbide wall, heat transfer between the reaction and cooling channels occurs at higher rates compared to alumina and steel wall because of the higher thermal conductivity value of wall material. This situation both decreases the temperature in the reaction channel and inhibits the cracking reactions. Since the reaction rates decrease with decreasing channel temperature, heat released by the cracking reaction also decreases, i.e. use of silicon carbide wall material causes overcooling and lower temperatures as a result of chained effects as in the case of low WHSV values discussed in the previous section. In the case of alumina wall, however, temperature of the reaction channel stays high due to low thermal conductivity. High temperature causes higher reaction rates and heat release due to exothermic cracking reactions, which causes much higher temperatures as a result of chained effects. Finally, the investigation of Figures 4.24 and 4.25 shows that temperatures observed in the cooling and reaction channels are very close to each other which is an indication of improved heat transfer in the microchannel system.

Figure 4.26 shows the conversion of C_{22+} normal hydrocarbon profile along the reaction channel for different wall materials. The results show that highest conversion value (99%) is obtained with alumina wall, whereas stainless steel and silicon carbide walls have led to 95% and 90% conversions, respectively. Differences in the obtained conversion values can be explained by the temperature profiles obtained for these wall materials. Highest temperature is observed with alumina wall (Figure 4.24) which

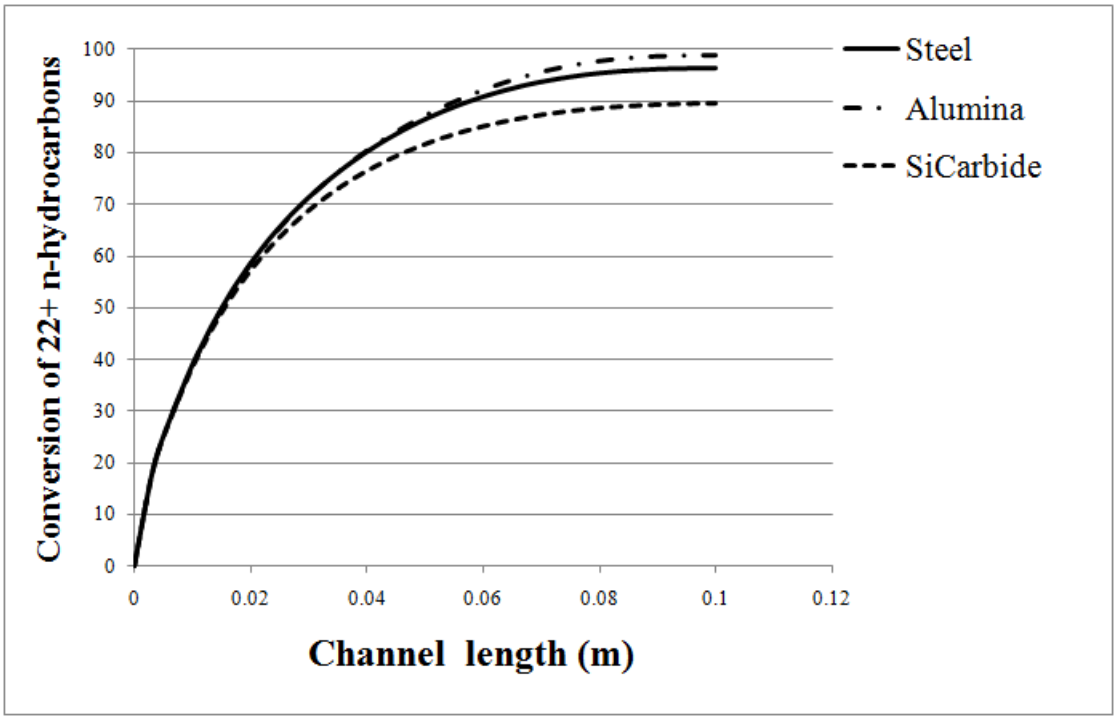

Figure 4.26. 22+ N-hydrocarbon conversion profiles along reaction channel with different wall materials.

also gave the highest conversion value since the reaction rates are highly dependent on temperature. Similar relations are valid for the stainless steel and silicon carbide wall cases; lowest conversion and temperature values are obtained with silicon carbide wall since it has the highest thermal conductivity among the investigated wall materials.

Figure 4.27 shows the molar fractions of jet fuel with respect reactor length and its dependence on wall material type. Highest molar fraction of jet fuel at the channel exit is obtained in the case of stainless steel wall and the lowest fraction is obtained in the case of silicon carbide wall. As it can be seen from Figure 4.27 use of alumina wall gives lower fractions of jet fuel with the jet fuel basis configuration of this study although it yields higher conversion values (Figure 4.26). Profile of the jet fuel fraction for the alumina case exhibits the occurrence of the maximum fraction followed by the decrease with the extent of the hydrocracking reaction.

Investigation of the jet fuel cut profiles for alumina wall and stainless steel wall cases in Figure 4.27 shows that in some portions of the reactor, alumina wall gives

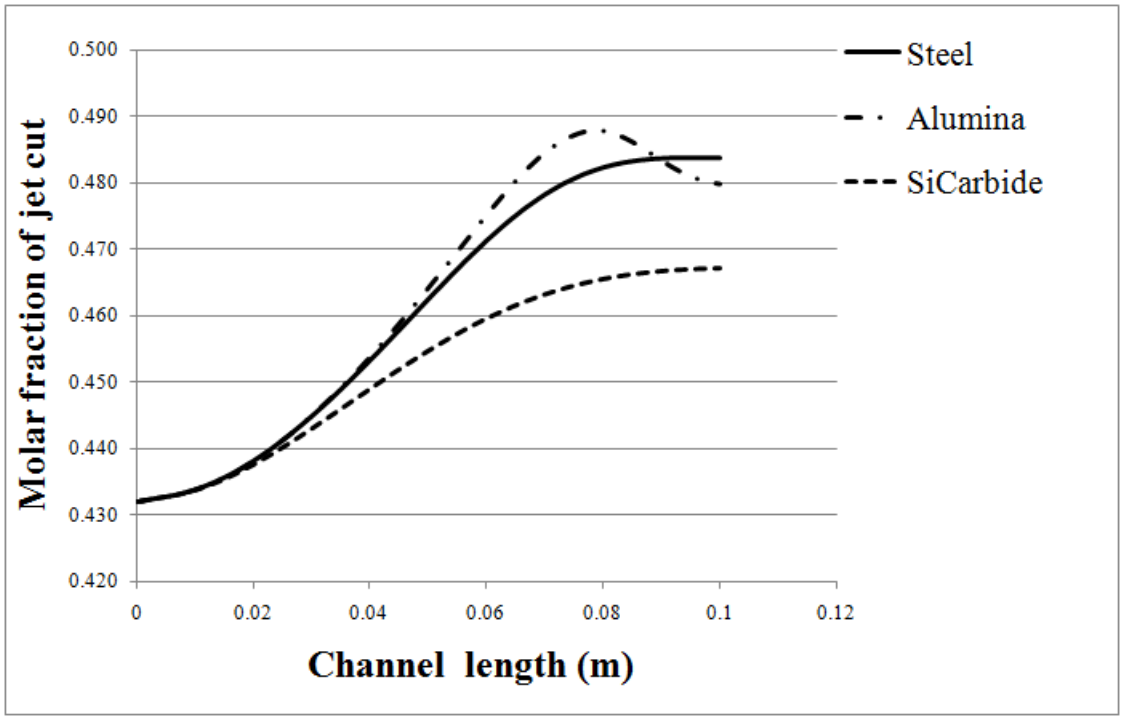

Figure 4.27. Jet fuel cut profiles along reaction channel with different wall materials.

higher fractions than stainless steel wall. This result shows that it is possible to obtain higher jet fuel cut fraction with alumina wall compared to stainless steel wall by changing the configuration of process variables. Figure 4.28 is shows the molar fractions of jet fuel cut at reactor outlet for different wall materials and residence times. It can be observed that maximum fraction of jet cut of 0.486 occurs in the case of alumina wall material at 200 h^{-1} WHSV. This configuration will give the similar product composition with the basis taken in this study (WHSV:180 h^{-1} and Steel wall), but it is also important to note that use of alumina wall instead of stainless steel increases the risk of hot spot formation and thermal runaway since it has lower thermal conductivity value compared to stainless steel wall.

Figure 4.29 shows the profiles of diesel fuel cut with respect to reactor length for different wall materials. The results show that silicon carbide wall gives a diesel fraction very close to the value at the input and stainless steel and alumina walls give values lower than the value at the input. The decrease in the case of alumina wall is highly pronounced since the use of alumina leads to highest conversion. In all of the three cases, fractions of diesel cut reach to their maximum, followed by decrease with further

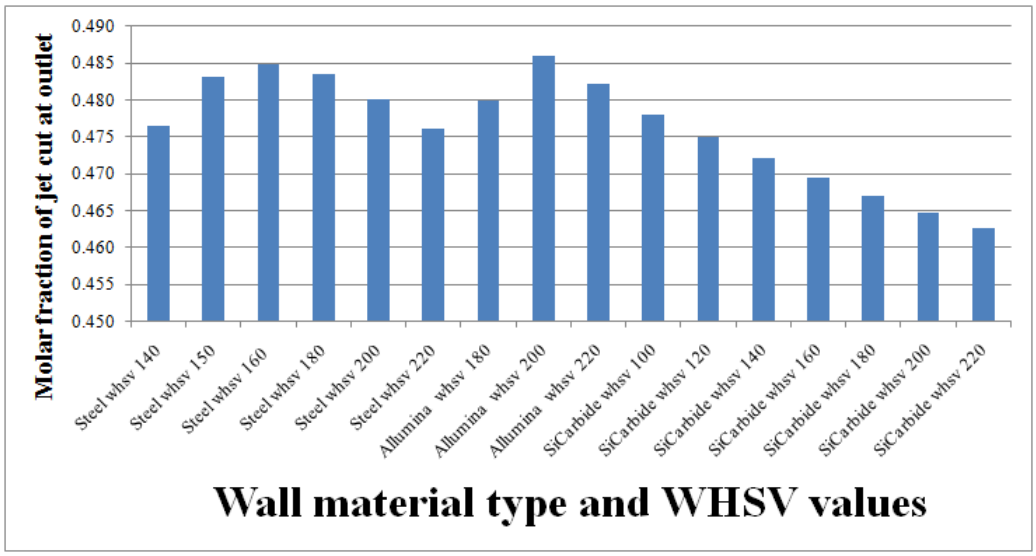

Figure 4.28. Jet fuel cut at reactor outlet for different wall materials and WHSV values.

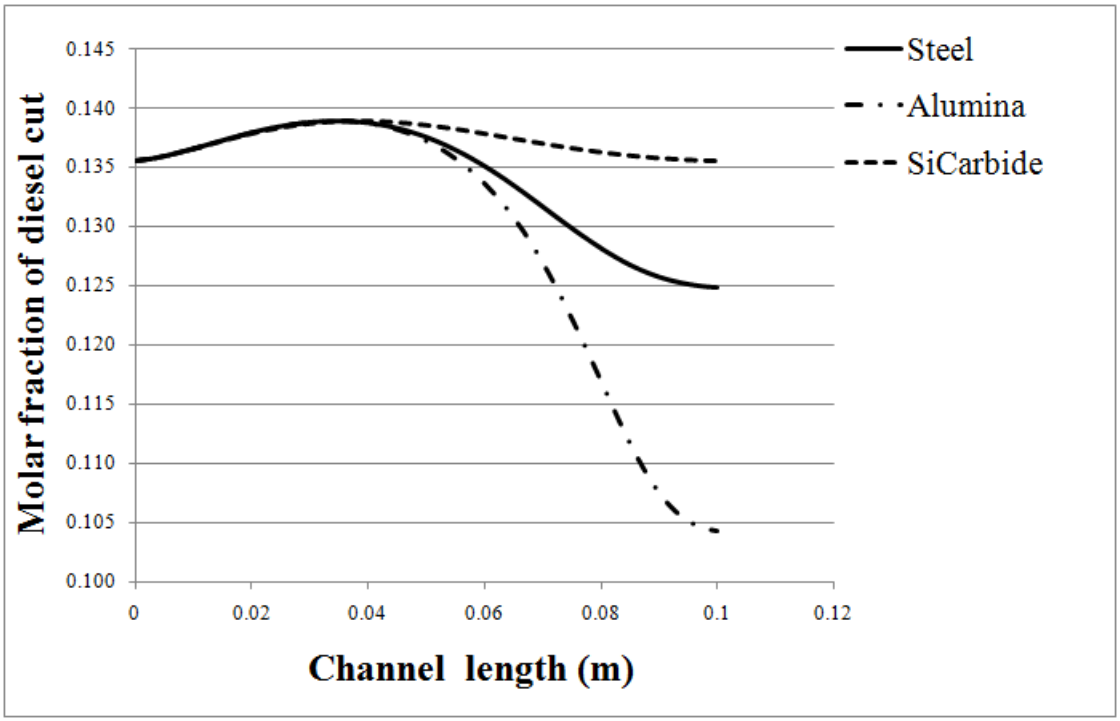

Figure 4.29. Diesel fuel cut profiles along reaction channel with different wall materials.

conversion. It is also observed that use alumina wall gives much lower diesel fraction compared to stainless steel wall while they are giving similar jet fuel fractions as it is seen in Figure 4.27. Considering the yields of diesel and jet fuel fractions together, use of stainless steel wall is able to give both jwt fuel and diesel fuel fractions at sufficiently high quantities.

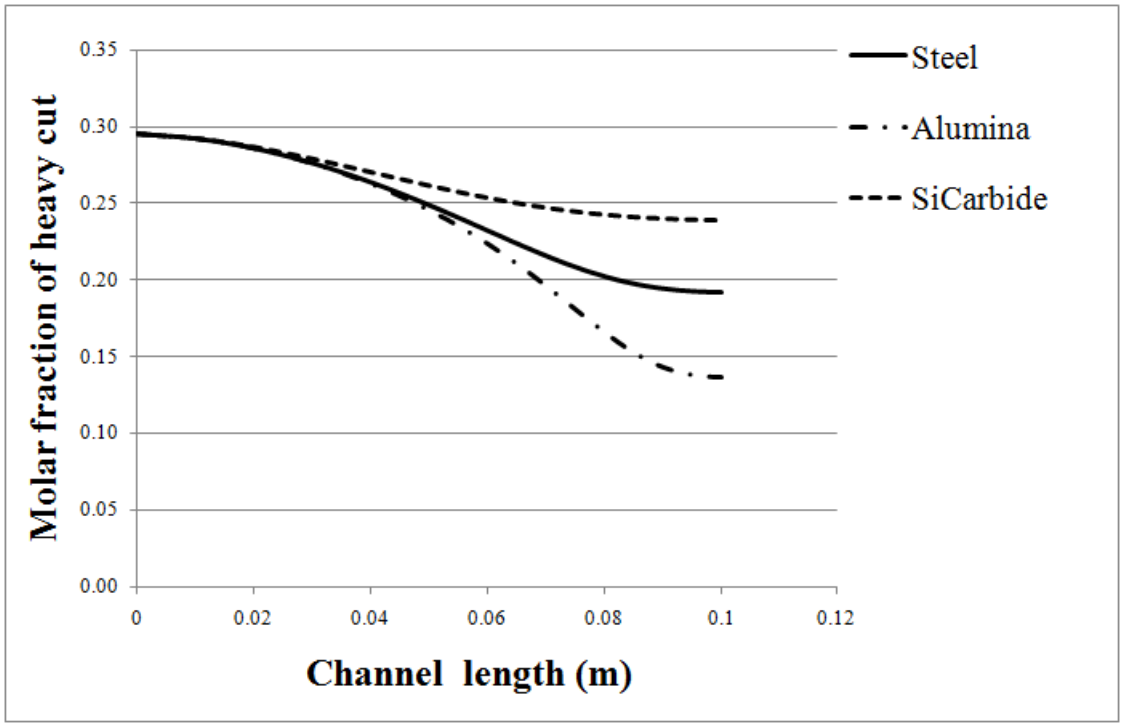

Figure 4.30. Heavy cut profiles along reaction channel with different wall materials.

Figure 4.30 shows the profiles of heavy cut along the reaction channel and effect of wall material on the heavy cut fraction. The results show that profiles of heavy cut fraction are in accordance with conversion in a negative manner. As it is seen in the figure, lowest amount of heavy cut fraction is obtained with alumina wall while the highest amount is obtained in the case of silicon carbide wall, which are giving the highest conversion and lowest conversion values, respectively. It is also observed that more than one half of the heavy cut fraction cracks into lighter fractions in the case of alumina wall while this value is around one third in the case of stainless steel. This situation shows that use of alumina wall gives better results in terms of decreasing the heavy cut fraction.

Figure 4.31 shows the isomer-to-normal hydrocarbon ratio with respect to reac-

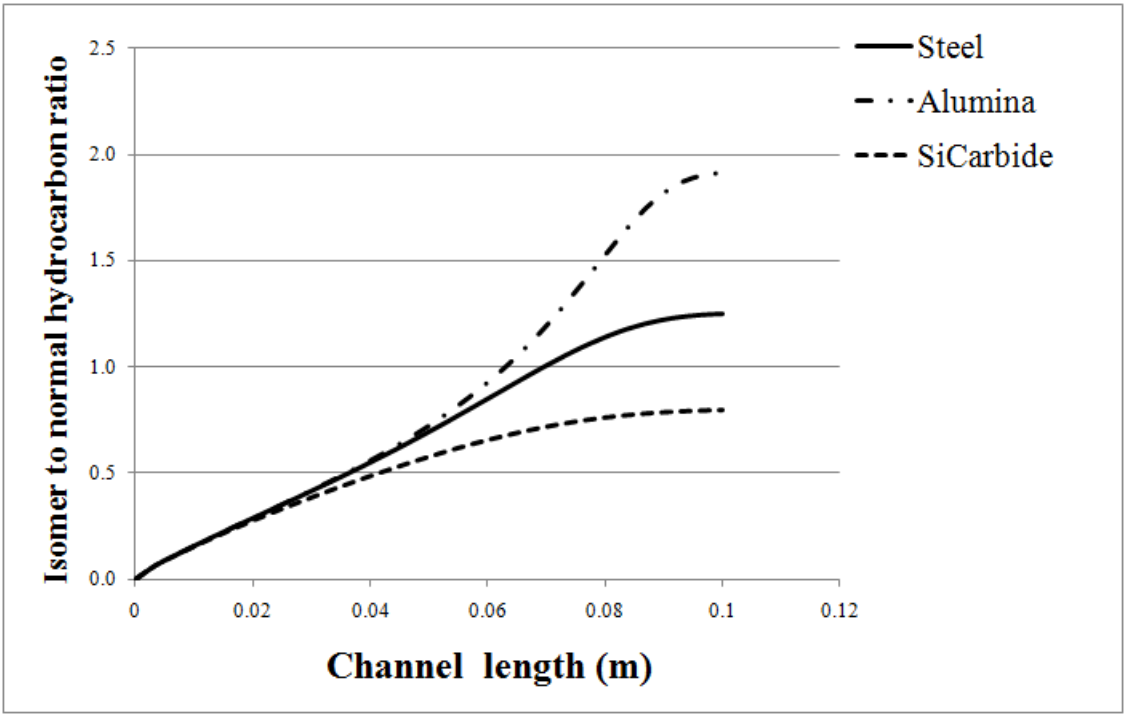

Figure 4.31. Isomer-to-normal ratio profiles along reaction channel with different wall materials.

tion channel length and effect of wall material on this ratio. As it is seen in the figure isomer-to-normal ratios show a similar behavior to conversion values, since the ratio is always increases with conversion in the investigated range, as shown in Figure 4.22. The ratio reaches values closer to 2 in the case of alumina wall, while stainless steel and silicon carbide give 1.3 and 0.8, respectively. Considering the fact that isomerization is increasing the cold flow properties of the fuels, use of alumina wall would be suitable for production of fuels for cold regions.

Figures 4.26, 4.27 and 4.29-4.31 also show that profiles of the investigated properties become constant while the reaction channel length is approaching 0.1 m. This is because of the fact that temperature of the reaction channel becomes very close to the inlet temperature of the coolant feed, which is specified as a boundary condition in the simulations. Due to low temperatures at this zone, profiles of the investigated properties become constant since reaction rates decrease with temperature and reactions does not proceed.

In this section profiles of jet fuel cut, diesel fuel cut, heavy cut, conversion, isomer-to-normal paraffin ratio and reaction channel temperature along the reactor are given in figures at diesel fuel base configuration (Table 3.7) and effect of wall material type on these properties are investigated. Diesel fuel base configuration is defined as the combination of operating and reactor parameters that gives maximum mole fraction of diesel. As it is seen in Figure 4.11, maximum yield of jet cut occurs at 450°C reactant and 300°C coolant feed temperatures with 220 h^{-1} WHSV.

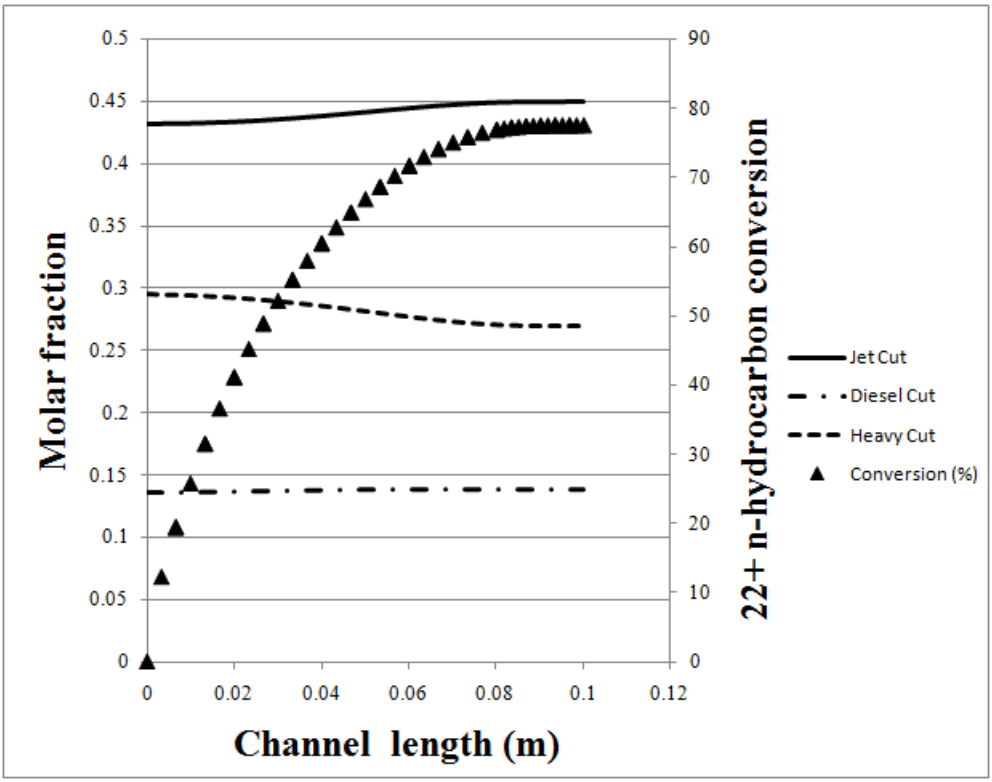

Figure 4.32. Jet fuel, diesel fuel, heavy cut and conversion of 22+ n-hydrocarbon profiles along reaction channel at diesel base configuration.

Figure 4.32 shows the profiles of jet fuel, diesel fuel and heavy cuts in primary axis and conversion of C_{22+} normal hydrocarbons in the secondary axis along the reaction channel. As it is seen from the figure that, the fraction of diesel fuel cut increass from 13.5% to 13.9% and, fraction of jet fuel cut is increases from 43% to 45% with the cracking process, while fraction of heavy cut decrease down to 26%. Profiles of the jet fuel, diesel and heavy cuts are showing that with the hydrocracking process fractions of desired jet fuel cut and diesel fuel cut are increasing while only the unwanted heavy cut fraction is decreasing which is one of the of objectives stated in Section 2.2.2.

Comparison of Figure 4.32 and Figure 4.23 is showing that diesel base configuration gives higher heavy cut fraction and lower jet fuel cut fraction since the conversion stays at lower values at this configuration. Diesel base configuration reaches 75% conversion while jet fuel base configuration reaches 96%. On the other hand diesel base configuration keeps the fraction of diesel cut as much as possible while jet fuel base configuration is decreasing the amount of diesel cut.

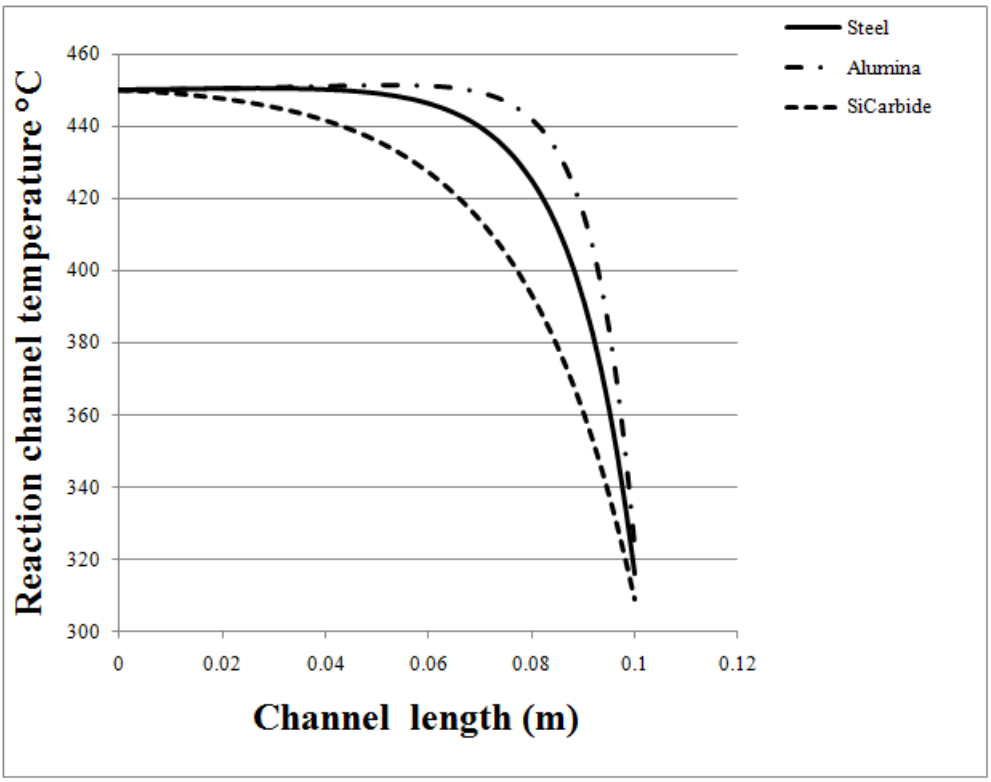

Figure 4.33. Temperature profile along reaction channel with different wall materials.

Figure 4.33 and Figure 4.34 show the temperature profiles of reaction and cooling channels, respectively. The results show that use of alumina wall keeps the temperature of the reaction channel higher compared to silicon carbide and stainless steel walls while the lowest temperature values are observed in the case of silicon carbide wall. This situation is related to the thermal conductivity of the wall materials as in the case of jet fuel base configuration. As stated in Table 3.8, silicon carbide wall has the highest thermal conductivity and alumina has the lowest thermal conductivity values among the investigated material types with 87 W/(m.K) and 27 W/(m.K) respectively, while thermal conductivity of stainless steel wall is 44.5 W/(m.K). In the case of alumina wall, highest temperature observed is 451°C which is slightly higher than

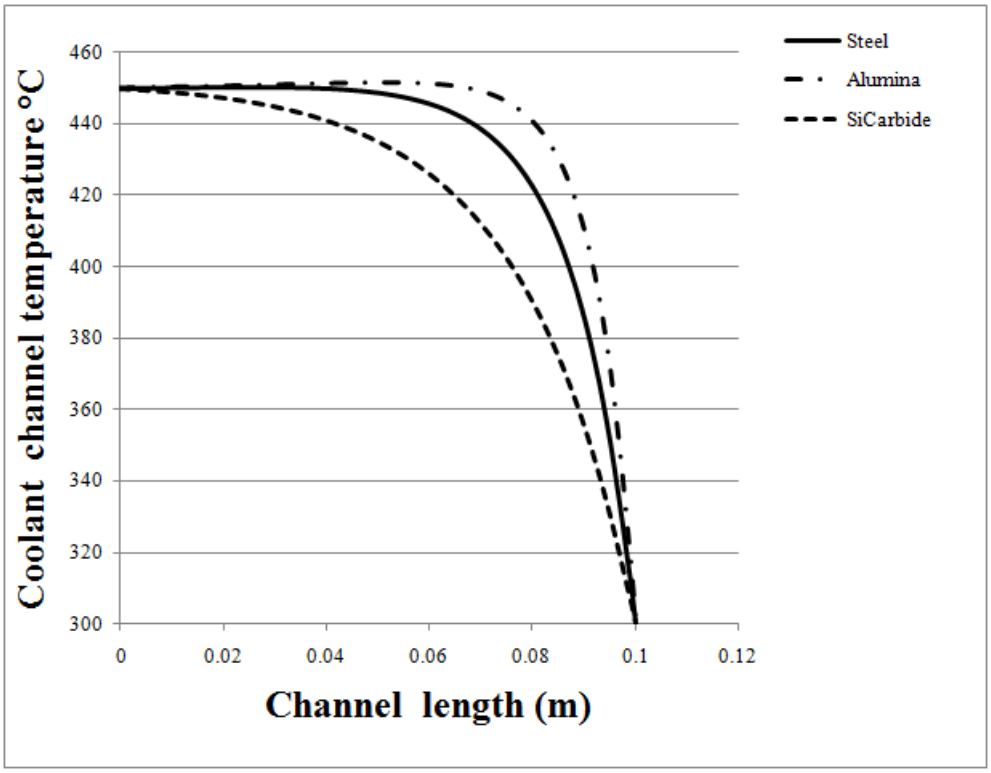

Figure 4.34. Temperature profile along cooling channel with different wall materials.

the feed temperature. In the cases of stainless steel and silicon carbide walls, however, significant temperature increases do not occur, but elevations up to 10°C are reported for the jet fuel base (Figure 4.24). This situation can be explained by the differences of the configurations; temperature difference between the coolant and reactant stream is 70°C and 150°C for the jet fuel base and diesel base configurations, respectively and residence time of the diesel base configuration (WHSV:220 h^{-1}) is lower than the jet fuel base configuration (WHSV:180 h^{-1}). Higher temperature difference and lower residence time keep the temperature of the reaction channel low even preventing the temperature increase although the reactions are exothermic.

In the case silicon carbide wall, heat transfer between the reaction and cooling channels occur at higher rates compared to alumina and steel wall because of the higher thermal conductivity value of wall material. This situation both decreases the temperature in the reaction channel and inhibits the cracking reactions. Since the reaction rates decrease with decreasing channel temperature, heat released by the cracking reaction also decreases. In other words use of silicon carbide wall material causes overcooling

and lower temperatures as a result of chained effects as in the case of low WHSV values discussed in the previous section. The trends demonstrated for steel and alumina, as well as their reasons are the same as given for the jet fuel base case in Figure 4.24 and 4.25 and in Section 4.2.

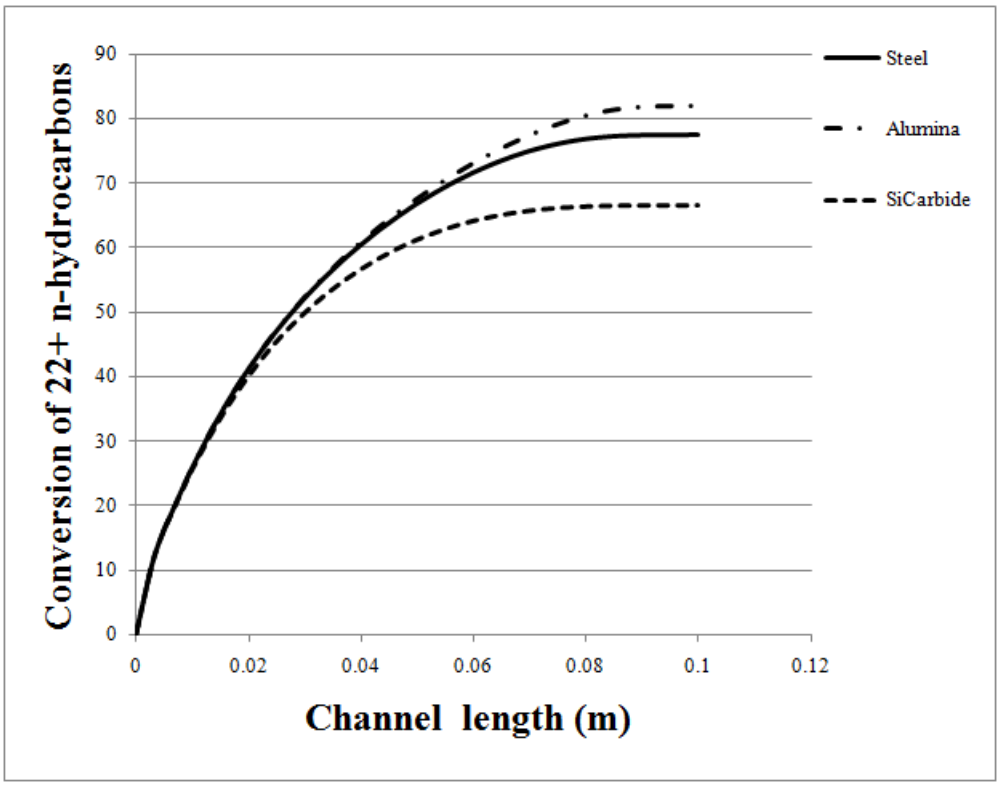

Figure 4.35. 22+ N-hydrocarbon conversion profiles along reaction channel with different wall materials.

Figure 4.35 shows the conversion of C_{22+} normal hydrocarbon profile along the reaction channel for different wall materials. The results show that highest conversion value (82%) is obtained with alumina wall, whereas stainless steel and silicon carbide walls have led to 78% and 66% conversions, respectively. Differences in the obtained conversion values can be explained by the temperature profiles obtained for these wall materials. Highest temperature is observed with alumina wall (Figure 4.33) which also gave the highest conversion value since the reaction rates are highly dependent on temperature. Similar relations are valid for the stainless steel and silicon carbide wall cases; lowest conversion and temperature values are obtained with silicon carbide wall since it has the highest thermal conductivity among the investigated wall materials. Comparison Figure 4.26 and Figure 4.35 shows that diesel base configuration gives lower

conversion values (∼75%) compared to jet fuel base configuration (∼90%) because of lower temperatures in the reaction channel.

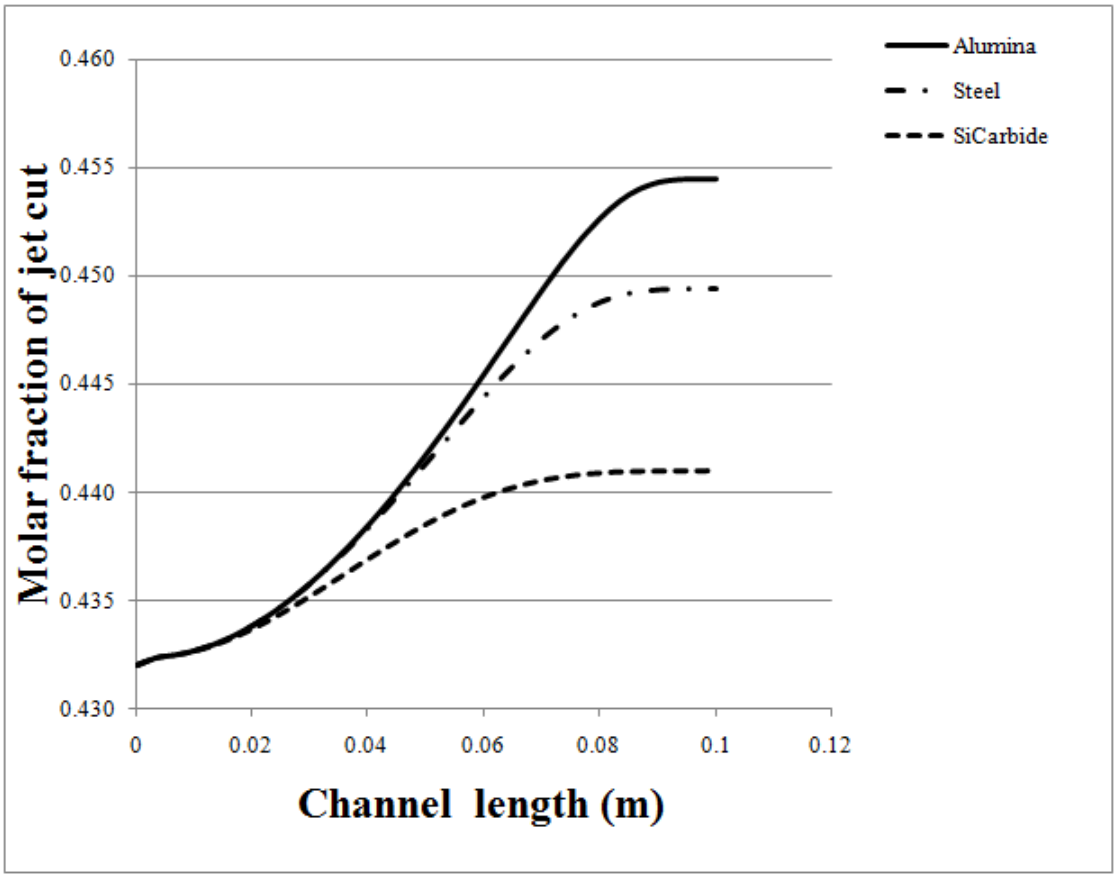

Figure 4.36. Jet fuel cut profiles along reaction channel with different wall materials.

Figure 4.36 shows the molar fractions of jet fuel cut with respect reaction channel length and its dependence on wall material type. Highest molar fraction of jet fuel at the channel exit is obtained in the case of alumina wall and the lowest fraction is obtained in the case of silicon carbide wall. Profiles of jet fuel cut are showing a positive relationship with conversion values given in Figure 4.35 since they are well below of the conversion value corresponding to the maximum jet fuel fraction which is 75%.

Figure 4.37 shows the profiles of diesel fuel cut with respect to reactor length for different wall materials. The results show that stainless steel wall gives the highest diesel fuel cut fraction at the channel exit, while silicon carbide and alumina lead to lower diesel fuel cut fractions. Although alumina wall is giving higher conversion values compared to stainless steel (Figure 4.35), lower fractions of diesel fuel cut are

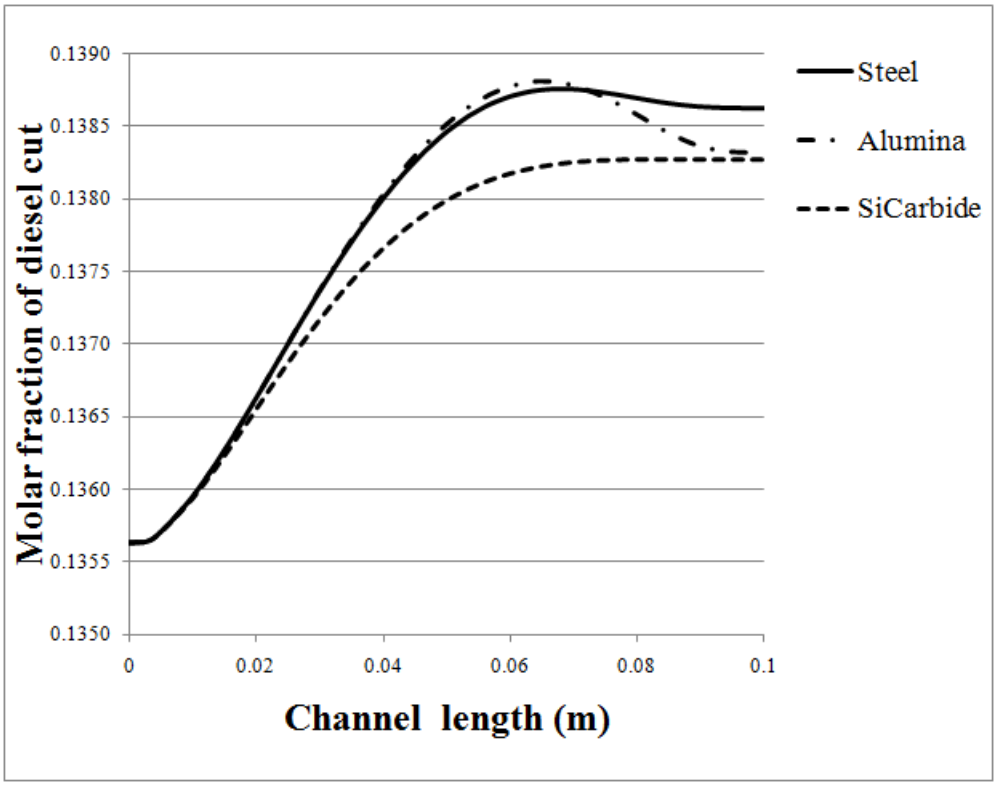

Figure 4.37. Diesel fuel cut profiles along reaction channel with different wall materials.

occurring since the conversion values are exceeding the conversion value corresponding to the maximum diesel fraction (75%) while conversion values are not exceeding this value with stainless steel wall.

Figure 4.38 shows the profiles of heavy cut along the reaction channel and effect of wall material on the heavy cut fraction. The results show that profiles of heavy cut fraction are in accordance with conversion in a negative manner. As it is seen in the figure, lowest amount of heavy cut fraction is obtained with alumina wall while the highest amount is obtained in the case of silicon carbide wall, which are giving the highest conversion and lowest conversion values respectively. Comparison of Figures 4.38 and 4.30 shows that diesel fuel base configuration gives significantly higher heavy cut fractions compared to jet fuel base configuration. Heavy cut fraction at diesel base configuration occurs around 26% while jet fuel base configuration is giving around 16%. In the case of diesel base configuration 10% of the heavy cut fraction cracks into hydrocarbons with lower numbers of carbon atoms at most, while 50% of heavy cut

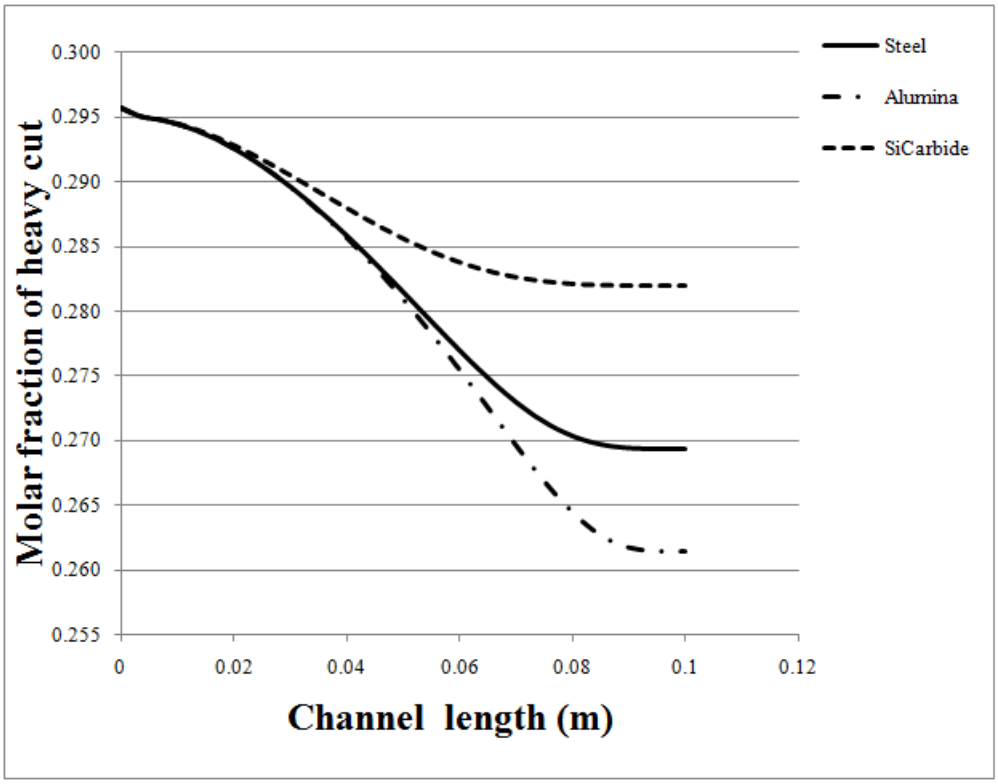

Figure 4.38. Heavy cut profiles along reaction channel with different wall materials.

cracks into lighter molecules in the case of jet fuel base configuration at most.

Figure 4.39 shows the isomer-to-normal hydrocarbon ratio with respect to reaction channel length and effect of wall material on this ratio. As it is seen in the figure, isomer-to-normal ratios show a similar behavior to conversion values, since the ratio always increases with conversion in the investigated range, as shown in Figure 4.22. The ratio reaches values closer to 0.6 in the case of alumina wall, while stainless steel wall and silicon carbide wall give 0.5 and 0.35, respectively.

Comparison of Figures 4.39 and 4.31 shows that significantly lower values of isomer-to-normal hydrocarbon ratios are occurring in the case of diesel fuel base configuration which is related to the lower conversion values occurring with the diesel base configuration. Figures 4.35-4.39 also show that profiles of the investigated properties become constant while the reaction channel length is approaching 0.1 m. This is because of the fact that temperature of the reaction channel becomes very close to the inlet temperature of the coolant feed, which is specified as a boundary condition in the

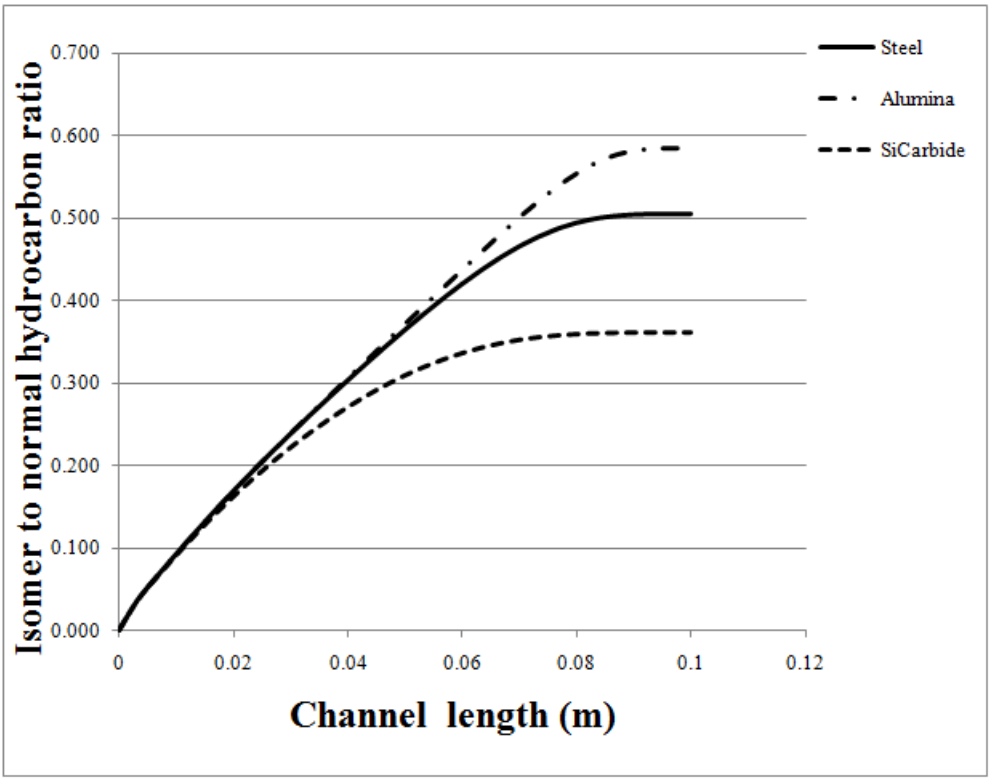

Figure 4.39. Isomer-to-normal ratio profiles along reaction channel with different wall materials.

simulations. Due to low temperatures at this zone, profiles of the investigated properties become constant since reaction rates decrease with temperature and reactions does not proceed.

4.3. Effect of H_2-to-wax ratio on wax hydrocracking

In this section effect of H_2 to wax ratio which is defined as kg H_2 feed / kg hydrocarbon feed is investigated in the range of 0.06 to 0.15, while process variables are kept constant as in jet fuel base configuration given in Table 3.6 except the WHSV value which is taken 180 h^{-1} in order to investigate effect of hydrogen in a wider range without having thermal runaway problem.

Figure 4.40 and 4.41 show the conversion of C_{22+} normal hydrocarbon profiles along the channel length and outlet values, respectively at different H_2/wax values. These figures indicate that effect of H_2/wax ratio is limited such that significant changes

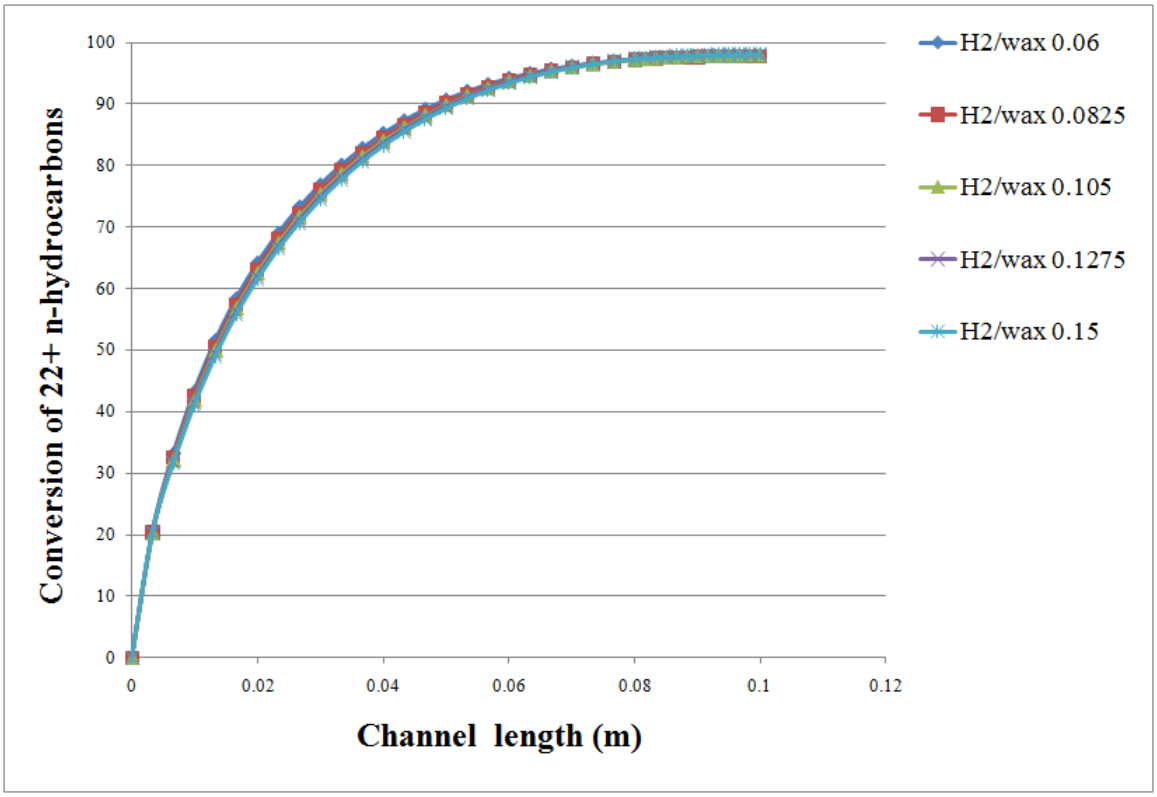

Figure 4.40. 22+ N-hydrocarbon conversion profiles at different H_2/wax ratios.

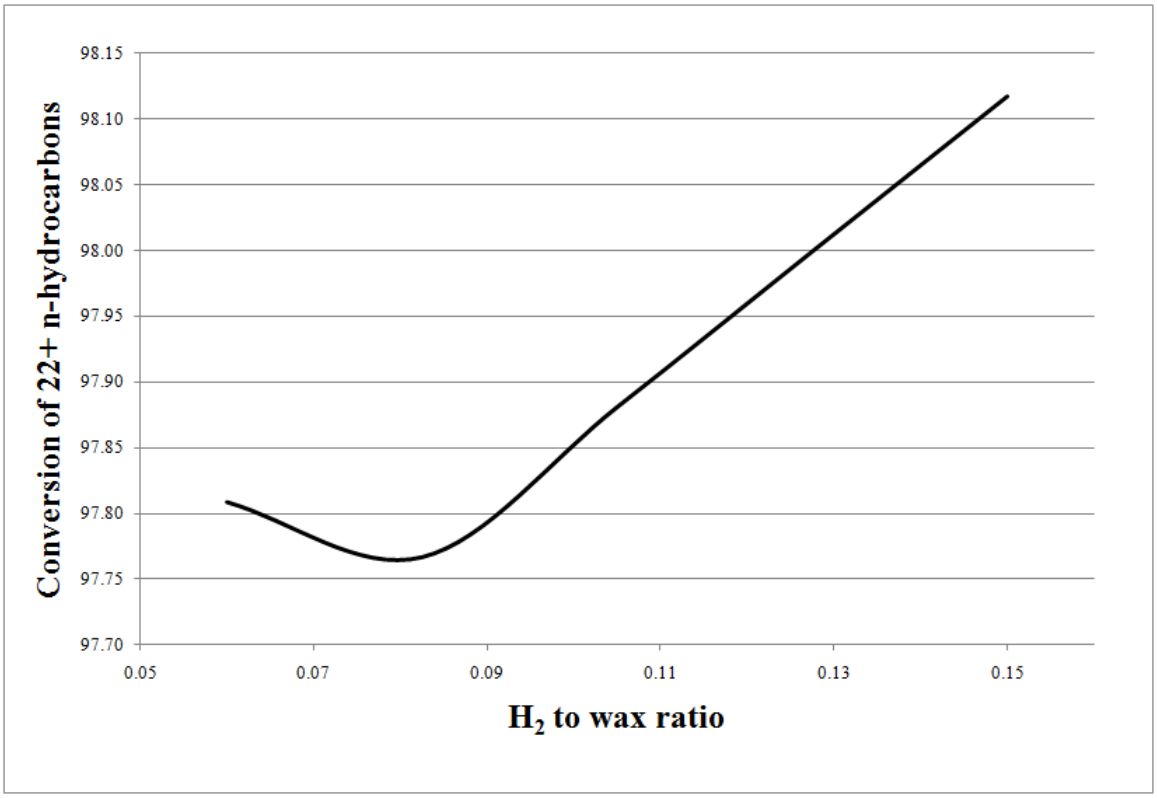

Figure 4.41. 22+ N-hydrocarbon conversion values at different H_2/wax ratios.

are not occurring in the overall profile and limited changes are occurring at the output conversion values.

There is a positive relationship between conversion and H_2/wax ratio for the majority of the investigated range which can be explained by the rate expression and the changes in amount of reactant feed. There is an ADSORB term in the rate expression containing multiplication of partial pressure of hydrogen with the summation of partial pressures of hydrocarbons. Rate expressions are defined as ratio of partial pressures of raw material and the ADSORB value. Decreasing the H_2/wax while keeping the total pressure of the system constant is increasing rates slightly. It is also important to note that reactant feed amount is decreasing with decreasing H_2/wax ratio which causes overcooling in the reaction channel causing lower conversions. This situation also explains the change in the profile at 0.06 H_2/wax ratio. The effects of overcooling and ADSORB terms are compensating each other. Figure 4.41 also shows that change in the conversion value is less than 0.25% within the investigated range since the changes in the rate expression variables are canceling each other and conversion values are already close to 100% conversion.

Figure 4.42-4.44 shows the profiles of jet fuel, diesel fuel and heavy cut profiles along the channel. As it is seen in figures, higher H_2/wax ratios are giving lower jet fuel cut, diesel fuel cut and heavy fractions since the conversion values are higher than the value corresponding to maximum jet fuel fraction. Higher H_2/wax ratios are increasing the conversion and decreasing the jet fuel cut, diesel fuel cut and heavy cut fractions in accordance with conversion.

Figure 4.45 shows the isomer-to-normal hydrocarbon ratio profile along the channel length, and indicates that H_2/wax ratio of 0.06 and 0.0825 give very close values and H_2/wax ratio of 0.15 is gives the maximum isomer-to-normal hydrocarbon ratio since its leads to the highest conversion value (98%, Figure 4.41).

Figures 4.46 and 4.47 show the reaction and cooling channel temperature profiles for different H_2/wax ratios. As can be seen from the figures, lowest temperature values

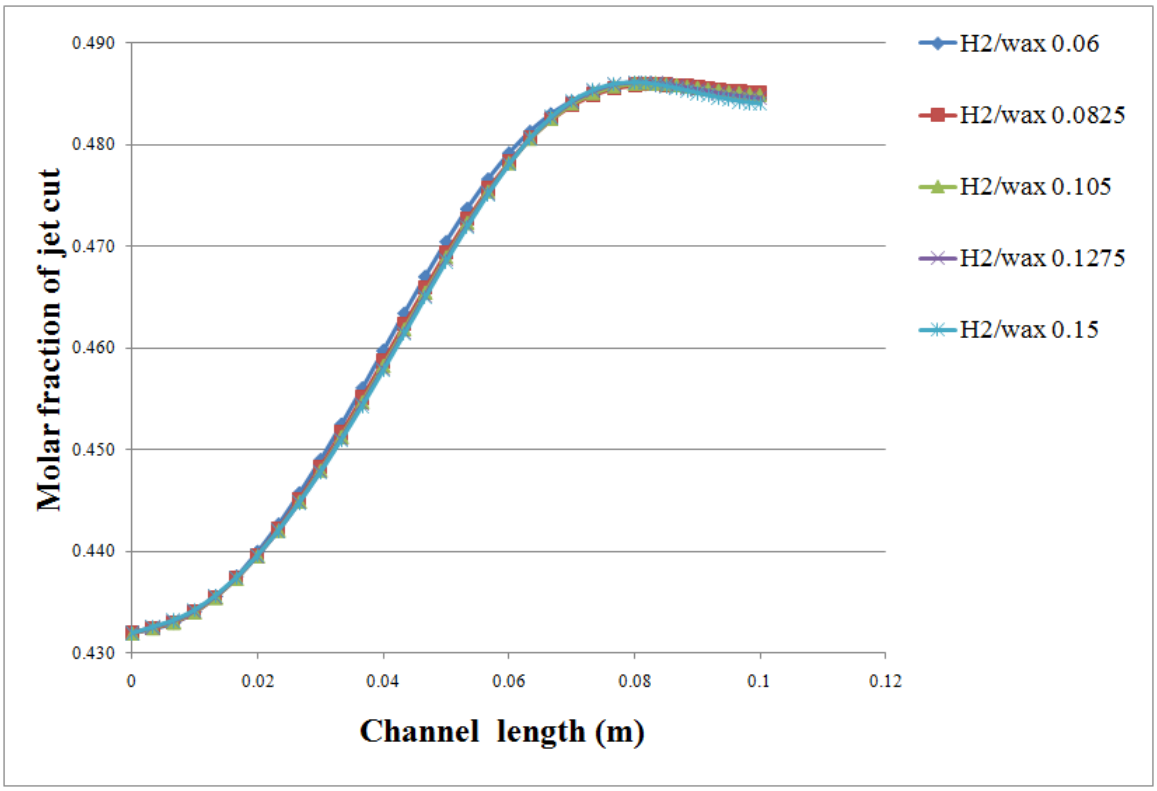

Figure 4.42. Molar fraction of jet fuel cut profiles at different H_2/wax ratios.

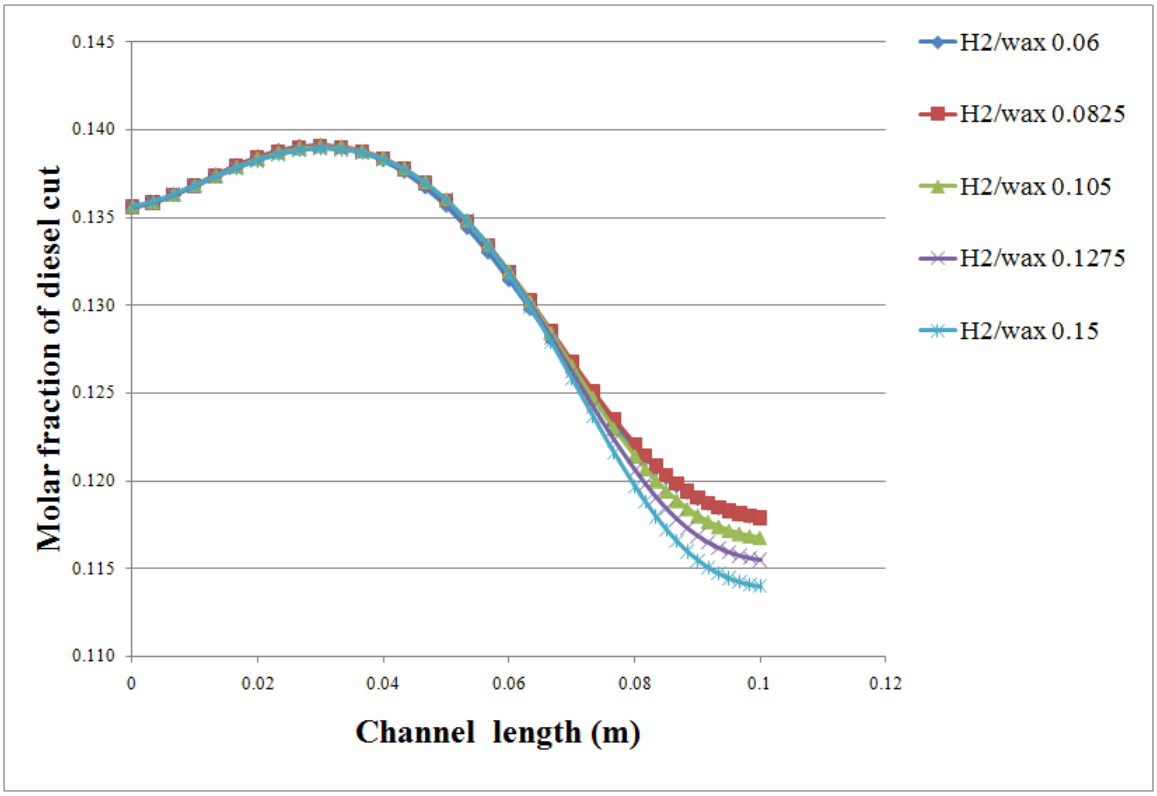

Figure 4.43. Molar fraction of diesel fuel cut profiles at different H_2/wax ratios.

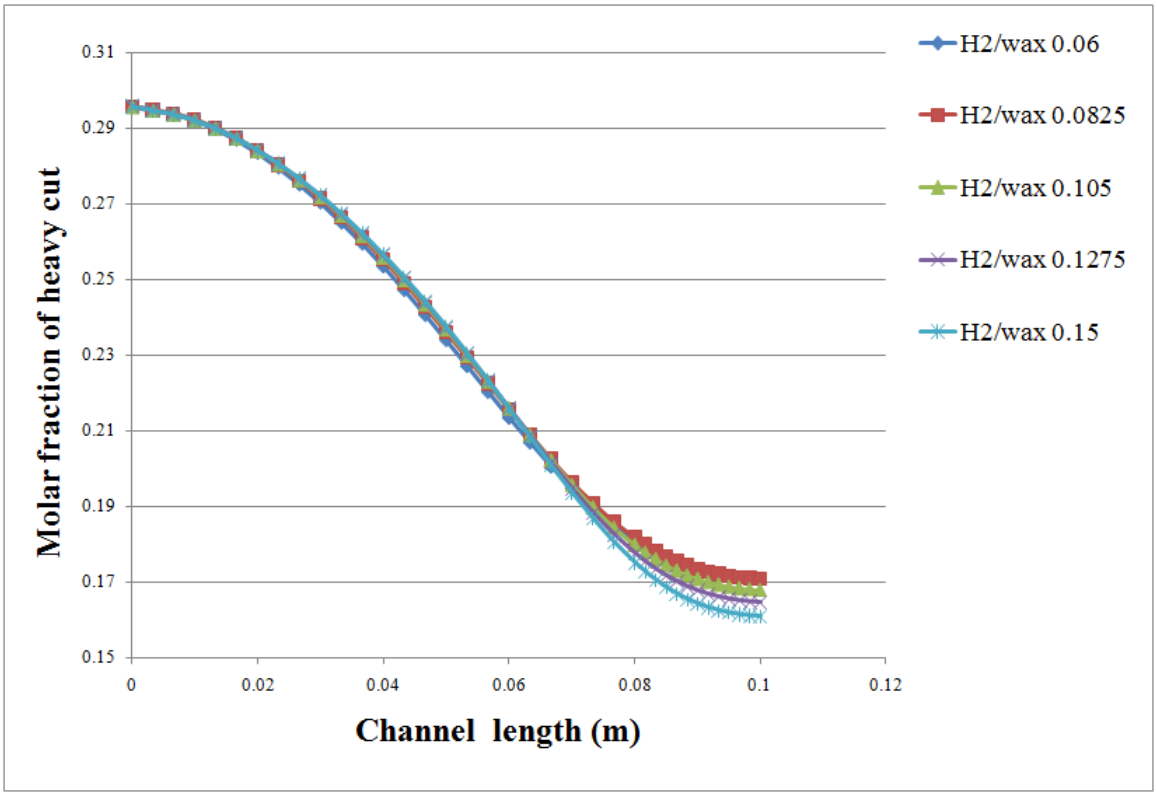

Figure 4.44. Molar fraction of heavy cut profiles at different H_2/wax ratios.

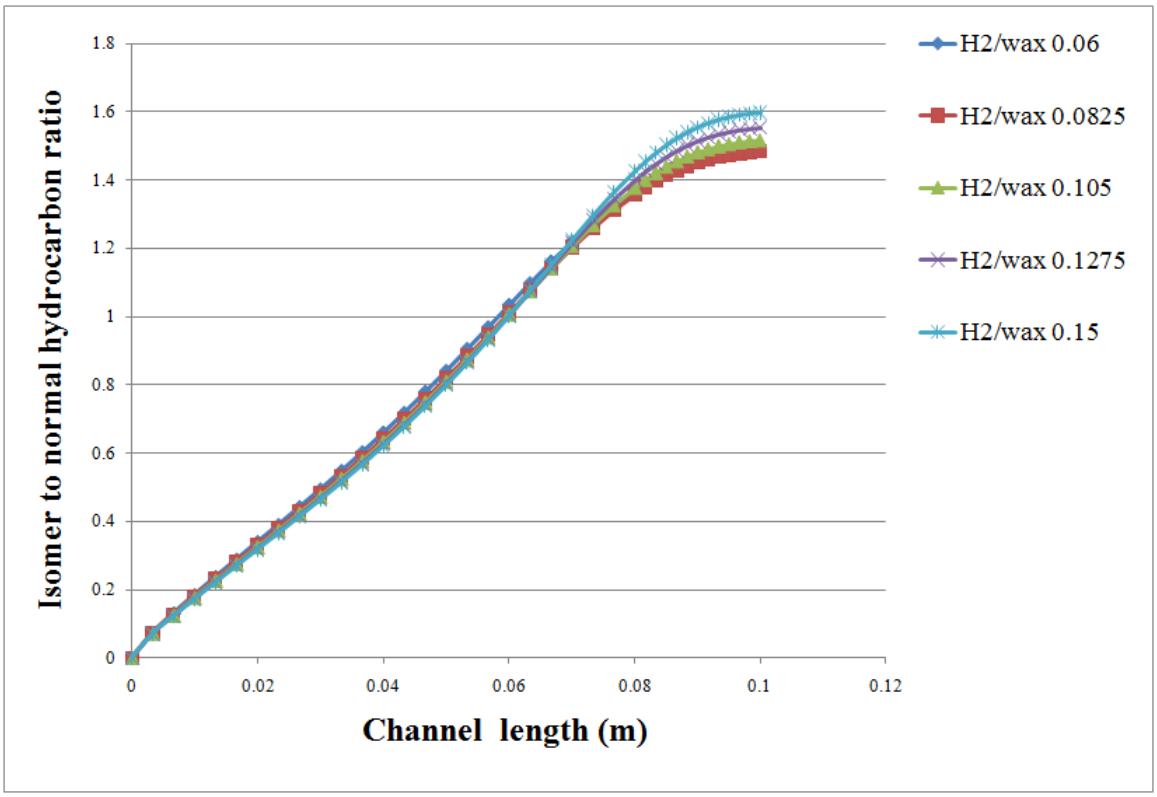

Figure 4.45. Isomer to normal hydrocarbon ratio profiles at different H_2/wax ratios.

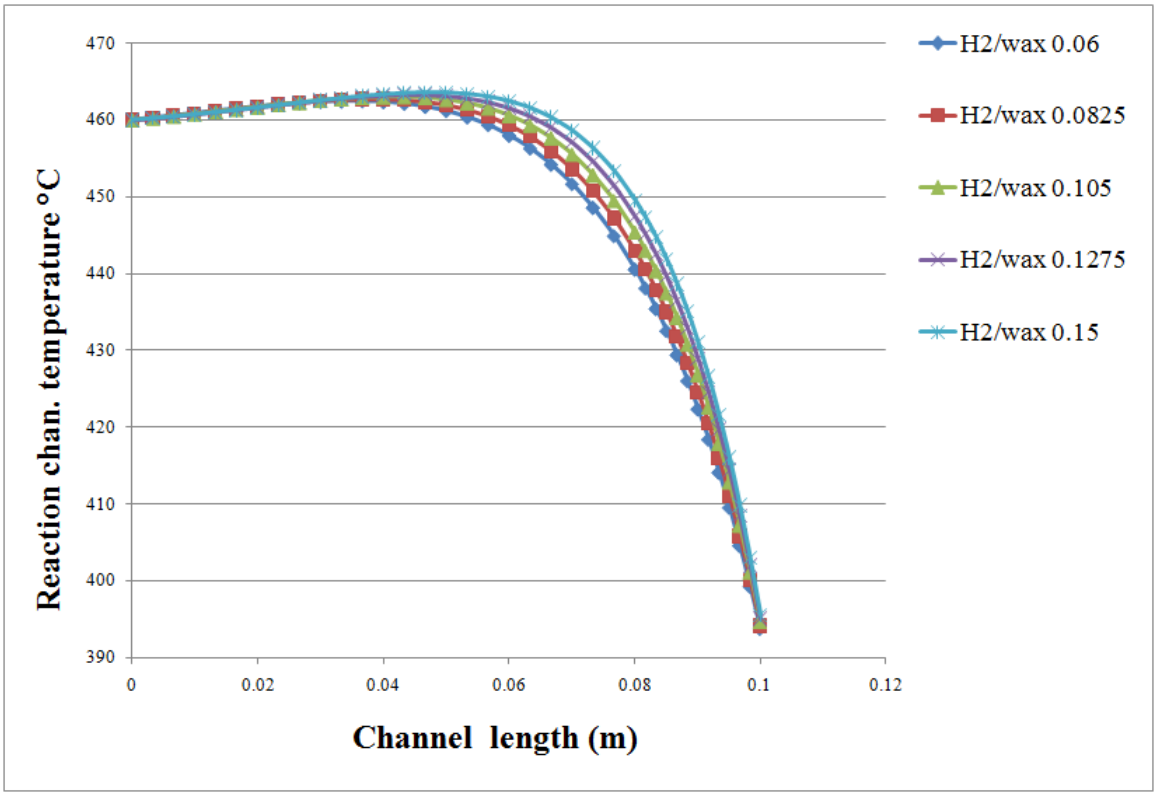

Figure 4.46. Reaction channel temperature profiles at different H_2/wax ratios.

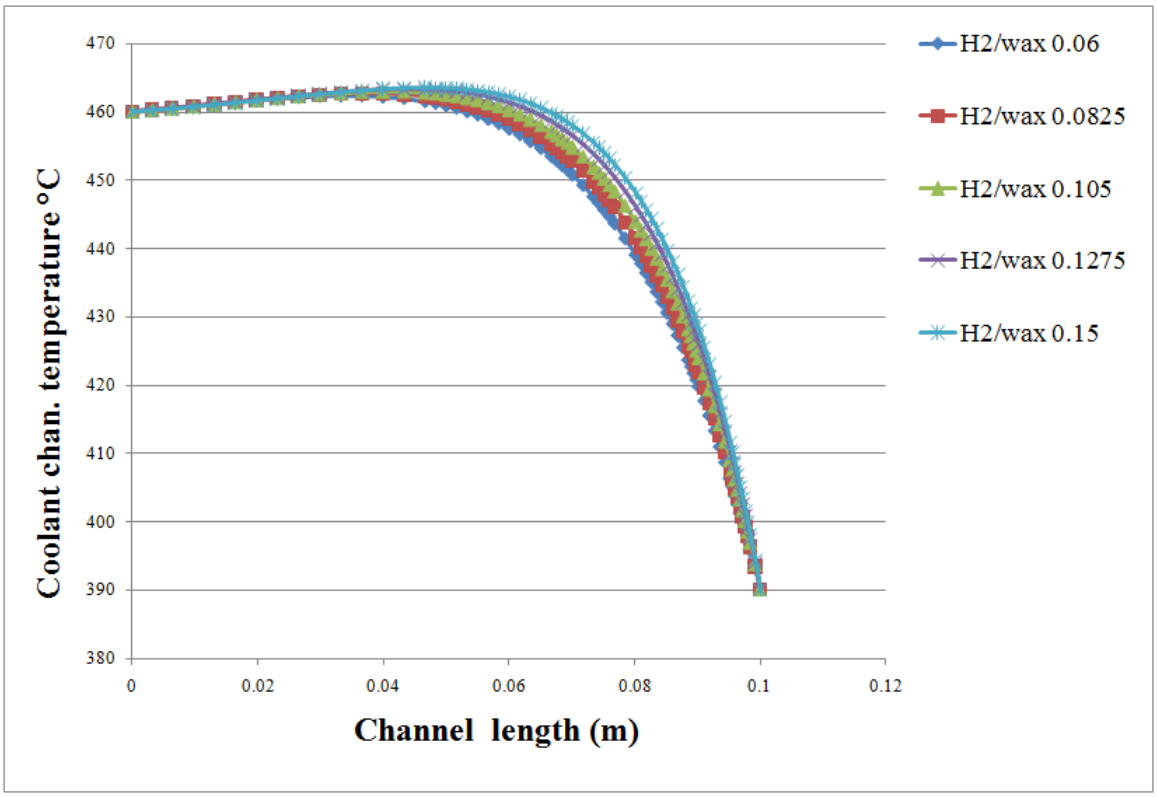

Figure 4.47. Cooling channel temperature profiles at different H_2/wax ratios.

are occurring in the case of 0.06 H_2/wax ratio and the highest temperature values are occurring in the case of 0.15 H_2/wax ratio, in which the conversion value and heat released by reactions are the highest among the values investigated.

4.4. Effect of reactive stream pressure on wax hydrocracking

In this section effect of reactive stream pressure on product, temperature, conversion and isomer-to-normal hydrocarbon ratio profiles along the reaction channel is investigated in the range of 41.25 bar to 60 bar while other process variables are kept constant as in jet fuel base configuration given in Table 3.6, except WHSV value which is taken 220 h^{-1} for investigating the effect of hydrogen in a wider range without having thermal runaway problem since reducing the pressure significantly effecting the process.

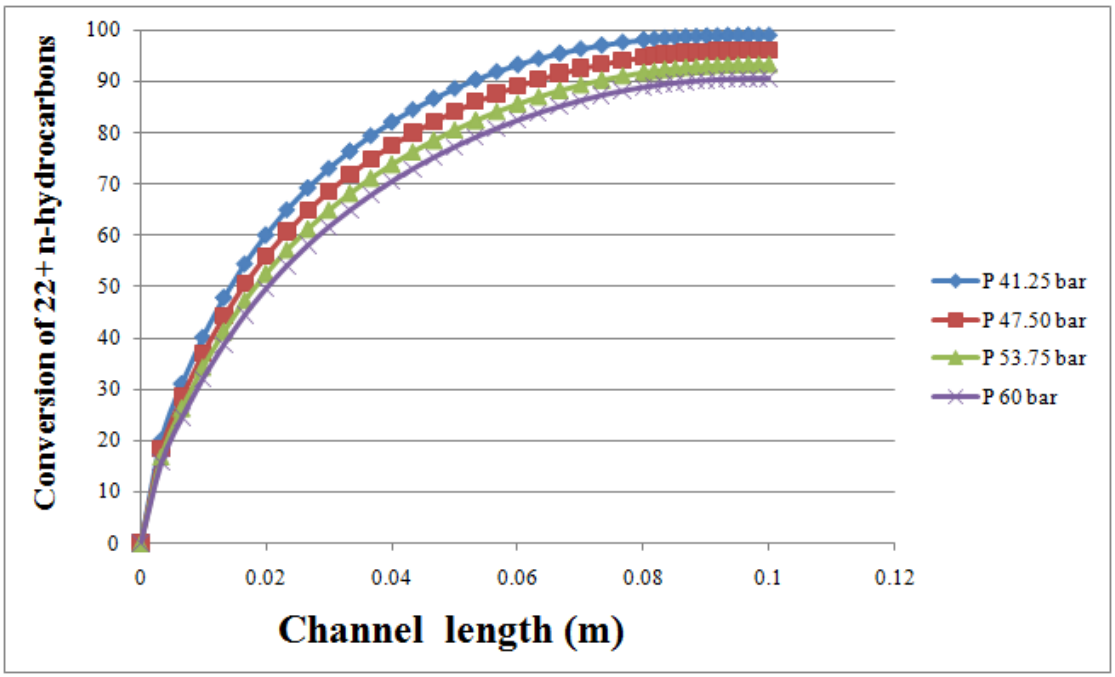

Figure 4.48. Conversion profiles for different reactive stream pressures.

Figure 4.48 shows the conversion of 22+ normal hydrocarbon profiles along the reactor with different system pressures. The results show that lower pressures cause higher conversion values, which is expected according to the rate expression and an experimental study [49]. The rate expressions have terms related to system pressure in both nominator and denominator which have first order and second order relations,

respectively. Therefore decreasing the pressure of reactive stream increases the ratio of the driving forces of reactions and ADSORB term.

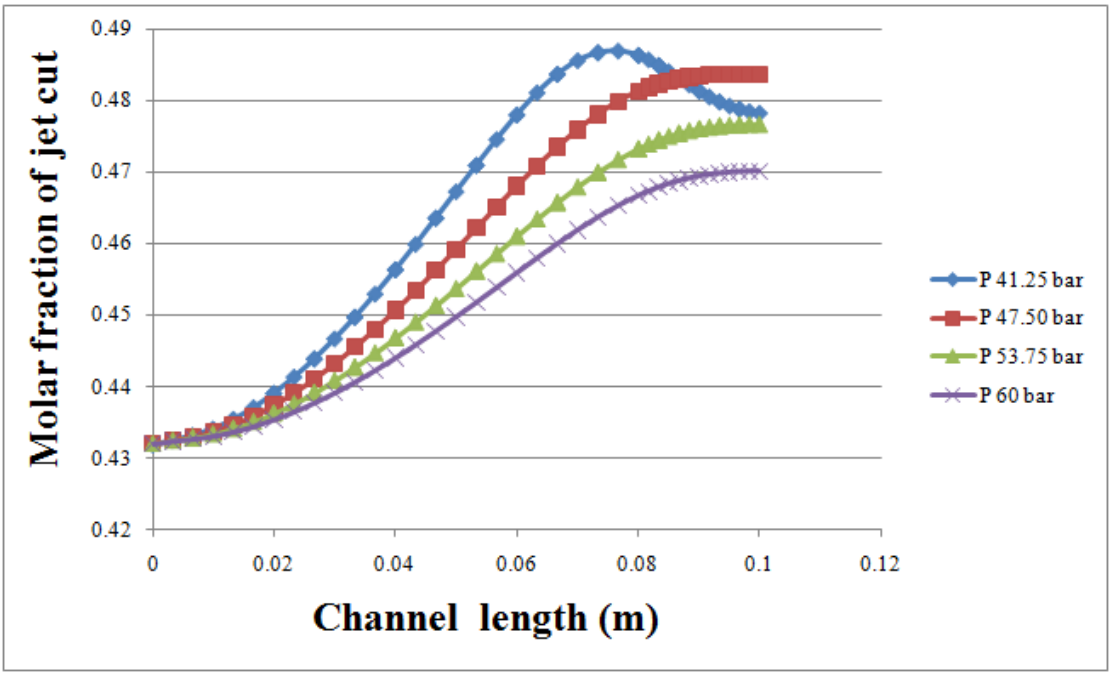

Figure 4.49. Molar fraction of jet fuel cut profiles for different reactive stream pressures.

Figures 4.49-4.51 show the profiles of jet fuel, diesel fuel and heavy cuts along the reaction channel at different reactive stream pressures. For diesel fuel and heavy cut, lower pressures are giving lower fractions since fraction of heavy cut decrease with conversion (Figure 4.48) and fraction of diesel cut decrease at these conversion values. Investigating Figure 4.49 shows that fraction of jet fuel reaches its maximum and decreases further at 41.25 bar reactive stream pressure due to high conversions. For other pressure values lower pressures are giving higher jet fuel cut fractions since the conversion values do not reach the value corresponding to maximum jet fuel fraction (96%).

Figure 4.52 shows the profile of isomer-to-normal hydrocarbon ratio along the reactor, as it is seen in the figure higher isomer-to-normal hydrocarbon ratios occur with lower pressure values in accordance with conversion which is always increasing with conversion within the investigated range of this study.

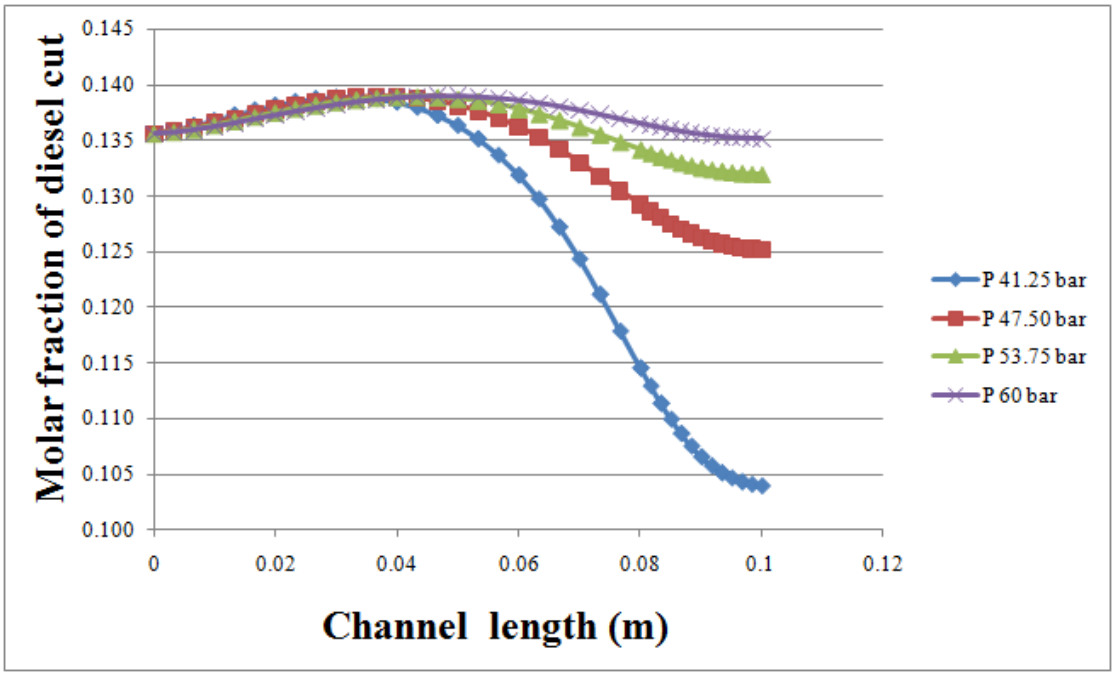

Figure 4.50. Molar fraction of diesel fuel cut profiles for different reactive stream pressures.

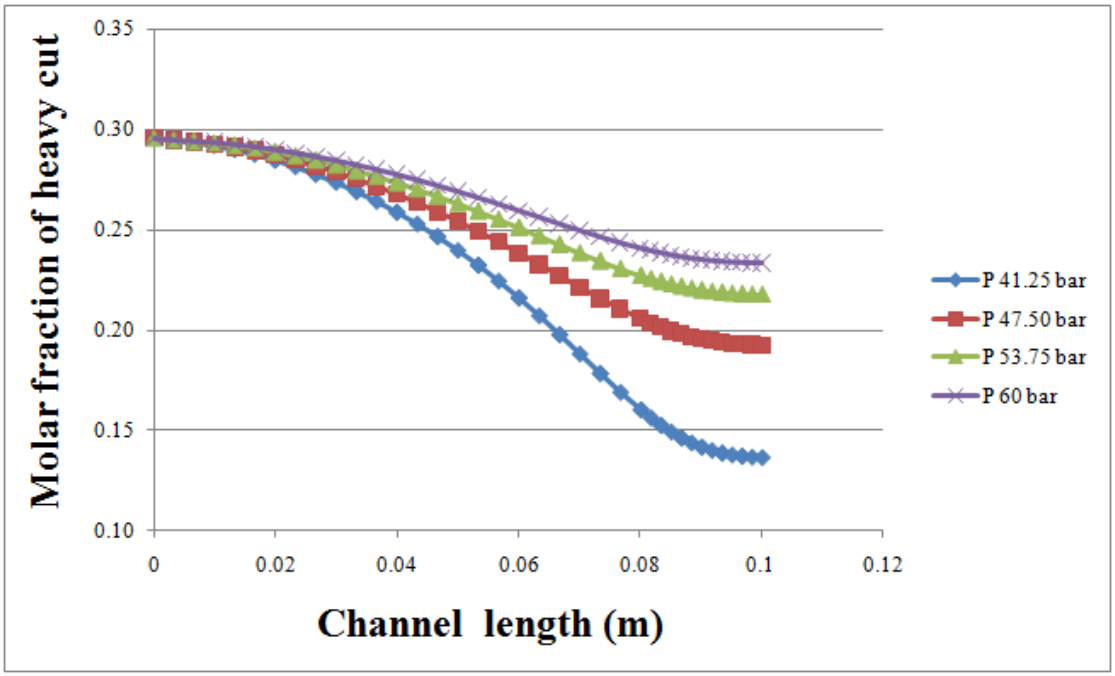

Figure 4.51. Molar fraction of heavy cut profiles for different reactive stream pressures.

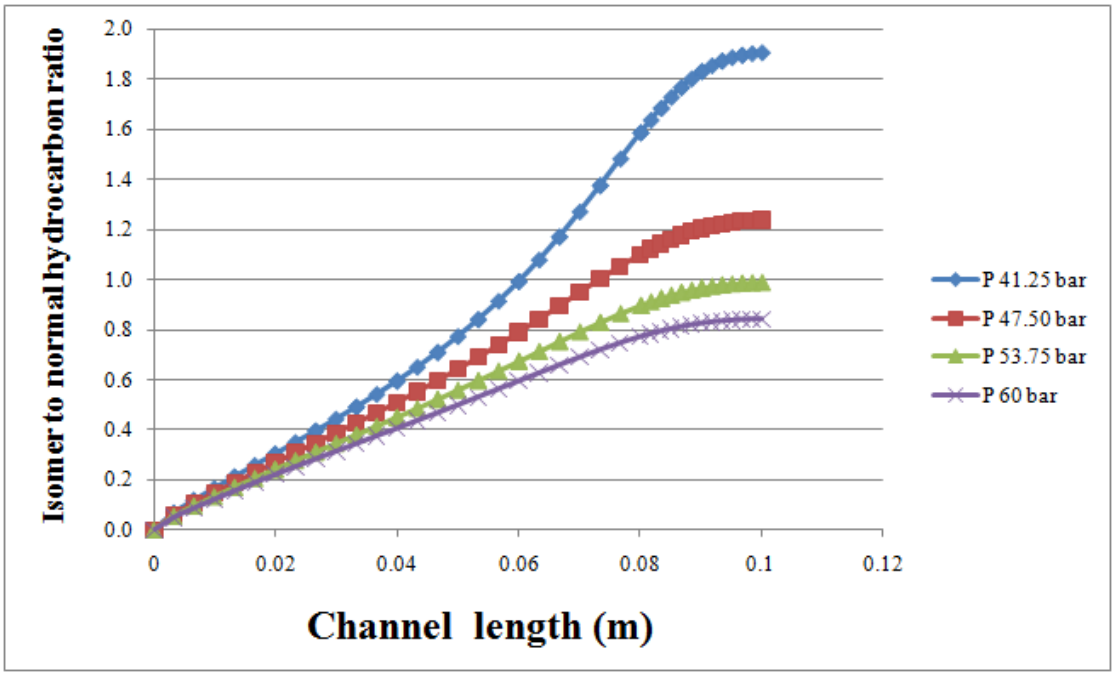

Figure 4.52. Isomer to normal hydrocarbon ratio profiles for different reactive stream pressures.

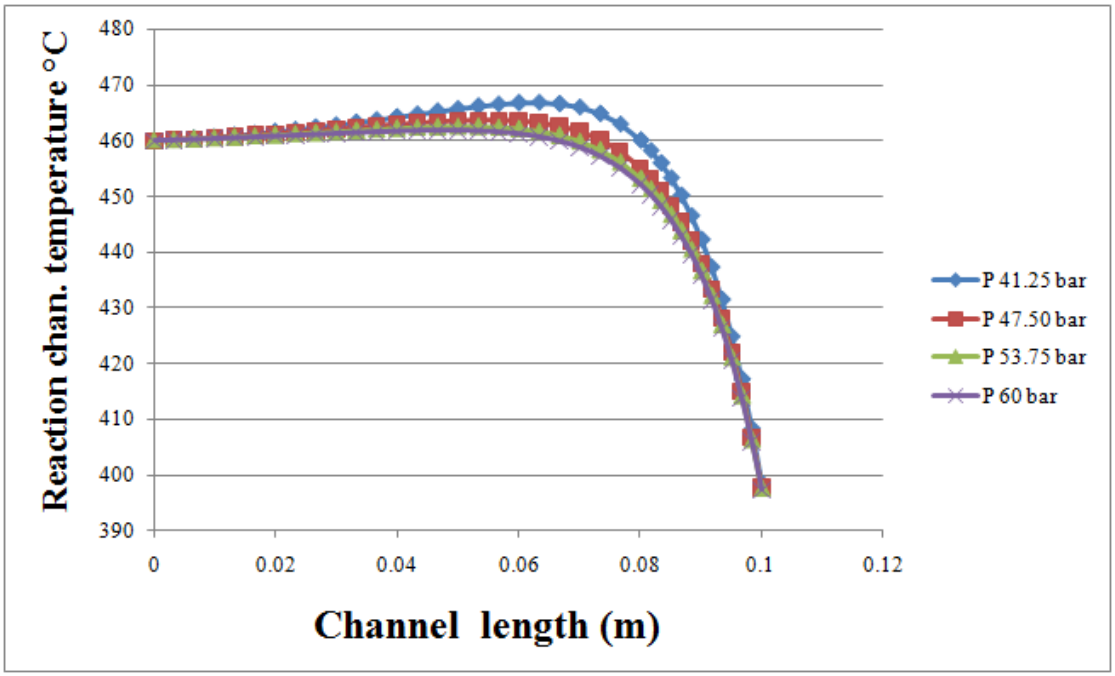

Figure 4.53. Reaction channel temperature profiles for different reactive stream pressures.

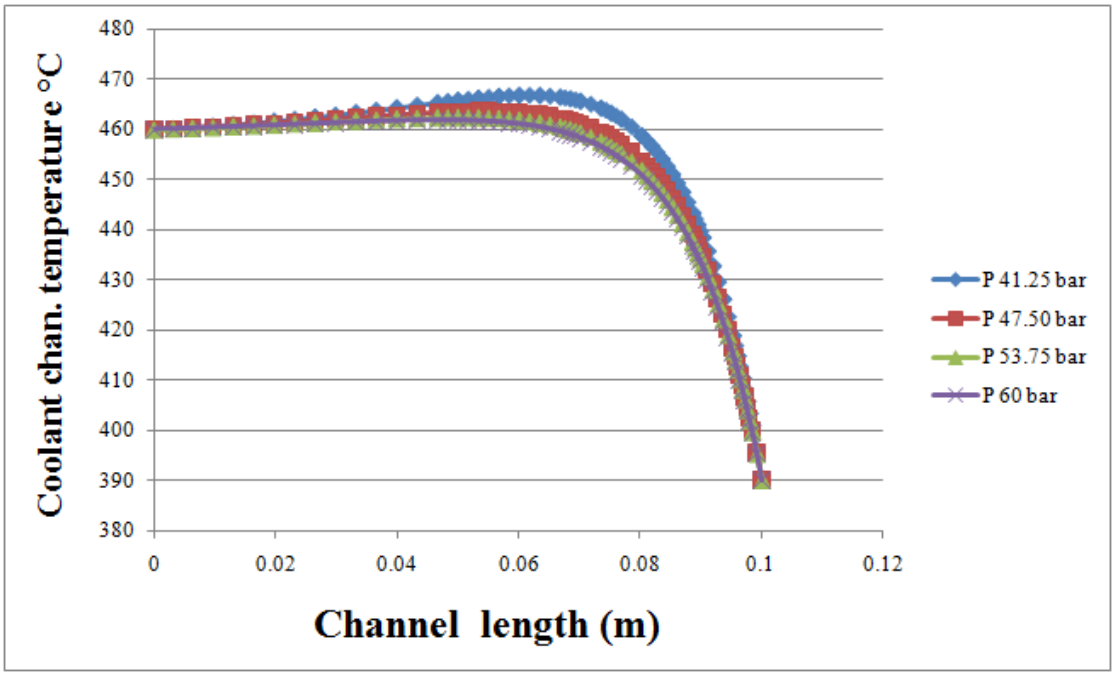

Figure 4.54. Cooling channel temperature profiles for different reactive stream pressures.

Figure 4.53 and 4.54 show the temperature profiles of reaction and cooling channel with respect to reactor length at different reactive stream pressure values, as it is seen in figures higher temperatures are occurring with lower pressure values as a result of higher heat released by exothermic reactions.

5. CONCLUSIONS AND RECOMMENDATIONS

5.1. Conclusions

The objectives of this study are to simulate the Fischer-Tropsch hydrocracking process in a microchannel reactor - heat exchanger system and to conduct a parametric investigation for exploring the effects of process variables such as reactant and coolant feed temperatures, residence time, type of wall material, reactive stream pressure and hydrogen-to-hydrocarbon ratio at the inlet. It is also aimed to investigate the capability of a microchannel reactor-heat exchanger system in terms of controlling the temperature of the hydrocracking process under various operating conditions. The conclusions obtained from this study can be listed as follows:

- Hydrocracking process is highly dependent on temperature; as it can be seen in Figures 4.1 and 4.3, the process can have a thermal runaway in the absence of temperature control resulting in the depletion of desired hydrocarbons to gaseous hydrocarbon with less than 4 carbon atoms. On the other hand the process does not proceed if the temperature values fall below certain values. In other words the hydrocracking process requires strict temperature control to produce desired products and to avoid thermal runaways.

- Desired products of the process; jet fuel fraction and diesel fuel fraction, behave like intermediate species. They reach a maximum upon proceeding of reactions and then decrease with further conversion. Therefore the system should be controlled precisely to avoid wasting of raw material.

- Hydrocracking process can increase the molar fraction jet fuel cut from 43% to 49%, diesel fuel cut fraction from 13.5% to 13.9%, decrease the heavy cut fraction from 29% to 15% and increase the isomer-to-hydrocarbon ratio from 0 to 2 by applying suitable process configurations.

- WHSV values have different effects on the process. At values higher than 140 h^{-1} residence time and conversion have a positive relationship, whereas at values lower than 140 h^{-1} conversion decreases with residence time as a result of overcooling if the coolant.

- Wall material type effects the process in a manner that materials with low thermal conductivity cause higher conversions since the heat transfer rates between the coolant and reaction channel is proportional to thermal conductivity of wall material. Low thermal conductivity keeps the temperature of reaction channel high and materials with high thermal conductivities decrease the conversion values as a result of same causes.

- Microchannel reactor-heat exchanger system enhances the heat transfer between the reaction and cooling channels and eliminates hot spot formations. Simulations show that microchannel system can eliminate temperature gradients in the y, direction which is perpendicular to direction of flowing streams.

5.2. Recommendations

The recommendations for enhancing this study on a possible future work is listed below.

- Effect of some other parameters that have not been investigated in this study can be investigated such as coolant stream inlet velocity, co-current orientation of coolant stream, changing side lengths of wall material, reaction channel and coolant channel and effect of different wall textures such as walls with micro-baffles.

- Rate expressions considering both olefins and paraffins instead of paraffins only can be applied, which is not readily available in literature.

- Rate expressions considering the degree of branching of the isomerized products

can be applied.

- Two phase flow in the reaction channel can be considered.

APPENDIX A: THERMOPHYSICAL PROPERTIES OF THE SPECIES

Table A.1. Viscosity coefficients of hydrogen (micropoise).

Species	**A**	**Bx10^{1}**	**Cx10^{4}**	**Dx10^{8}**
H_2	1.7611	3.4165	-1.8368	5.1147

Table A.2. Thermal conductivity coefficients of hydrogen (W/(mK)).

Species	**Ax10^{2}**	**Bx10^{4}**	**Cx10^{7}**	**Dx10^{11}**
H_2	1.0979	6.6411	-3.4378	9.7283

Table A.3. Enthalpy of formation values of normal hydrocarbons @298 K.

Species	**ΔH(J/mol)**	**Species**	**ΔH(J/mol)**	**Species**	**ΔH(J/mol)**
n-CH_4	-74500	n-$C_{25}H_{52}$	-559330	n-$C_{49}H_{100}$	-1054690
n-C_2H_6	-83800	n-$C_{26}H_{54}$	-579970	n-$C_{50}H_{102}$	-1075330
n-C_3H_8	-104700	n-$C_{27}H_{56}$	-600610	n-$C_{51}H_{104}$	-1095970
n-C_4H_{10}	-126800	n-$C_{28}H_{58}$	-621250	n-$C_{52}H_{106}$	-1116610
n-C_5H_{12}	-146800	n-$C_{29}H_{60}$	-641890	n-$C_{53}H_{108}$	-1137250
n-C_6H_{14}	-166900	n-$C_{30}H_{62}$	-662530	n-$C_{54}H_{110}$	-1157890
n-C_7H_{16}	-187800	n-$C_{31}H_{64}$	-683170	n-$C_{55}H_{112}$	-1178530
n-C_8H_{18}	-208800	n-$C_{32}H_{66}$	-703810	n-$C_{56}H_{114}$	-1199170
n-C_9H_{20}	-229030	n-$C_{33}H_{68}$	-724450	n-$C_{57}H_{116}$	-1219810
n-$C_{10}H_{22}$	-249500	n-$C_{34}H_{70}$	-745090	n-$C_{58}H_{118}$	-1240450
n-$C_{11}H_{24}$	-270430	n-$C_{35}H_{72}$	-765730	n-$C_{59}H_{120}$	-1261090
n-$C_{12}H_{26}$	-290830	n-$C_{36}H_{74}$	-786370	n-$C_{60}H_{122}$	-1281730
n-$C_{13}H_{28}$	-311770	n-$C_{37}H_{76}$	-807010	n-$C_{61}H_{124}$	-1302370
n-$C_{14}H_{30}$	-332440	n-$C_{38}H_{78}$	-827650	n-$C_{62}H_{126}$	-1323010
n-$C_{15}H_{32}$	-353110	n-$C_{39}H_{80}$	-848290	n-$C_{63}H_{128}$	-1343650
n-$C_{16}H_{34}$	-374170	n-$C_{40}H_{82}$	-868930	n-$C_{64}H_{130}$	-1364290
n-$C_{17}H_{36}$	-394450	n-$C_{41}H_{84}$	-889570	n-$C_{65}H_{132}$	-1384930
n-$C_{18}H_{38}$	-415120	n-$C_{42}H_{86}$	-910210	n-$C_{66}H_{134}$	-1405570
n-$C_{19}H_{40}$	-435790	n-$C_{43}H_{88}$	-930850	n-$C_{67}H_{136}$	-1426210
n-$C_{20}H_{42}$	-456460	n-$C_{44}H_{90}$	-951490	n-$C_{68}H_{138}$	-1446850
n-$C_{21}H_{44}$	-476770	n-$C_{45}H_{92}$	-972130	n-$C_{69}H_{140}$	-1467490
n-$C_{22}H_{46}$	-497410	n-$C_{46}H_{94}$	-992770	n-$C_{70}H_{142}$	-1488130
n-$C_{23}H_{48}$	-518050	n-$C_{47}H_{96}$	-1013410		
n-$C_{24}H_{50}$	-538690	n-$C_{48}H_{98}$	-1034050		

Table A.4. Enthalpy of formation values of iso-hydrocarbons and hydrogen @298 K.

Species	**ΔH(J/mol)**	**Species**	**ΔH(J/mol)**	**Species**	**ΔH(J/mol)**
i-C_4H_{10}	-135000	i-$C_{27}H_{56}$	-600610	i-$C_{50}H_{102}$	-1075330
i-C_5H_{12}	-153700	i-$C_{28}H_{58}$	-621250	i-$C_{51}H_{104}$	-1095970
i-C_6H_{14}	-174600	i-$C_{29}H_{60}$	-641890	i-$C_{52}H_{106}$	-1116610
i-C_7H_{16}	-191300	i-$C_{30}H_{62}$	-662530	i-$C_{53}H_{108}$	-1137250
i-C_8H_{18}	-215400	i-$C_{31}H_{64}$	-683170	i-$C_{54}H_{110}$	-1157890
i-C_9H_{20}	-235900	i-$C_{32}H_{66}$	-703810	i-$C_{55}H_{112}$	-1178530
i-$C_{10}H_{22}$	-256500	i-$C_{33}H_{68}$	-724450	i-$C_{56}H_{114}$	-1199170
i-$C_{11}H_{24}$	-275650	i-$C_{34}H_{70}$	-745090	i-$C_{57}H_{116}$	-1219810
i-$C_{12}H_{26}$	-295500	i-$C_{35}H_{72}$	-765730	i-$C_{58}H_{118}$	-1240450
i-$C_{13}H_{28}$	-318410	i-$C_{36}H_{74}$	-786370	i-$C_{59}H_{120}$	-1261090
i-$C_{14}H_{30}$	-339040	i-$C_{37}H_{76}$	-807010	i-$C_{60}H_{122}$	-1281730
i-$C_{15}H_{32}$	-359670	i-$C_{38}H_{78}$	-827650	i-$C_{61}H_{124}$	-1302370
i-$C_{16}H_{34}$	-380300	i-$C_{39}H_{80}$	-848290	i-$C_{62}H_{126}$	-1323010
i-$C_{17}H_{36}$	-400930	i-$C_{40}H_{82}$	-868930	i-$C_{63}H_{128}$	-1343650
i-$C_{18}H_{38}$	-421560	i-$C_{41}H_{84}$	-889570	i-$C_{64}H_{130}$	-1364290
i-$C_{19}H_{40}$	-442190	i-$C_{42}H_{86}$	-910210	i-$C_{65}H_{132}$	-1384930
i-$C_{20}H_{42}$	-462820	i-$C_{43}H_{88}$	-930850	i-$C_{66}H_{134}$	-1405570
i-$C_{21}H_{44}$	-476770	i-$C_{44}H_{90}$	-951490	i-$C_{67}H_{136}$	-1426210
i-$C_{22}H_{46}$	-497410	i-$C_{45}H_{92}$	-972130	i-$C_{68}H_{138}$	-1446850
i-$C_{23}H_{48}$	-518050	i-$C_{46}H_{94}$	-992770	i-$C_{69}H_{140}$	-1467490
i-$C_{24}H_{50}$	-538690	i-$C_{47}H_{96}$	-1013410	i-$C_{70}H_{142}$	-1488130
i-$C_{25}H_{52}$	-559330	i-$C_{48}H_{98}$	-1034050	H_2	0
i-$C_{26}H_{54}$	-579970	i-$C_{49}H_{100}$	-1054690		

Table A.5. Heat capacities of normal hydrocarbons @298 K.

Species	$\mathbf{C_P}$**(J/mol.K)**	**Species**	$\mathbf{C_P}$**(J/mol.K)**	**Species**	$\mathbf{C_P}$**(J/mol.K)**
n-CH_4	35.78	n-$C_{25}H_{52}$	577.76	n-$C_{49}H_{100}$	1120.63
n-C_2H_6	52.96	n-$C_{26}H_{54}$	600.23	n-$C_{50}H_{102}$	1148.05
n-C_3H_8	73.36	n-$C_{27}H_{56}$	623.79	n-$C_{51}H_{104}$	1169.96
n-C_4H_{10}	98.73	n-$C_{28}H_{58}$	647.38	n-$C_{52}H_{106}$	1184.95
n-C_5H_{12}	119.85	n-$C_{29}H_{60}$	670.05	n-$C_{53}H_{108}$	1214.11
n-C_6H_{14}	142.39	n-$C_{30}H_{62}$	689.79	n-$C_{54}H_{110}$	1237.50
n-C_7H_{16}	165.16	n-$C_{31}H_{64}$	716.90	n-$C_{55}H_{112}$	1253.57
n-C_8H_{18}	188.10	n-$C_{32}H_{66}$	736.64	n-$C_{56}H_{114}$	1281.67
n-C_9H_{20}	210.18	n-$C_{33}H_{68}$	765.67	n-$C_{57}H_{116}$	1301.49
n-$C_{10}H_{22}$	232.86	n-$C_{34}H_{70}$	784.82	n-$C_{58}H_{118}$	1325.16
n-$C_{11}H_{24}$	266.51	n-$C_{35}H_{72}$	803.64	n-$C_{59}H_{120}$	1350.50
n-$C_{12}H_{26}$	288.20	n-$C_{36}H_{74}$	832.63	n-$C_{60}H_{122}$	1365.27
n-$C_{13}H_{28}$	310.55	n-$C_{37}H_{76}$	850.82	n-$C_{61}H_{124}$	1396.09
n-$C_{14}H_{30}$	333.98	n-$C_{38}H_{78}$	878.45	n-$C_{62}H_{126}$	1427.67
n-$C_{15}H_{32}$	358.82	n-$C_{39}H_{80}$	898.74	n-$C_{63}H_{128}$	1448.02
n-$C_{16}H_{34}$	380.66	n-$C_{40}H_{82}$	917.50	n-$C_{64}H_{130}$	1467.51
n-$C_{17}H_{36}$	406.97	n-$C_{41}H_{84}$	939.31	n-$C_{65}H_{132}$	1495.84
n-$C_{18}H_{38}$	430.77	n-$C_{42}H_{86}$	964.36	n-$C_{66}H_{134}$	1515.42
n-$C_{19}H_{40}$	454.37	n-$C_{43}H_{88}$	984.07	n-$C_{67}H_{136}$	1540.68
n-$C_{20}H_{42}$	479.03	n-$C_{44}H_{90}$	1003.82	n-$C_{68}H_{138}$	1560.03
n-$C_{21}H_{44}$	487.24	n-$C_{45}H_{92}$	1028.44	n-$C_{69}H_{140}$	1580.90
n-$C_{22}H_{46}$	509.94	n-$C_{46}H_{94}$	1048.20	n-$C_{70}H_{142}$	1608.85
n-$C_{23}H_{48}$	532.63	n-$C_{47}H_{96}$	1076.93		
n-$C_{24}H_{50}$	555.01	n-$C_{48}H_{98}$	1096.98		

Table A.6. Heat capacities of iso-hydrocarbons and hydrogen @298 K.

Species	$\mathbf{C_P}$**(J/mol.K)**	**Species**	$\mathbf{C_P}$**(J/mol.K)**	**Species**	$\mathbf{C_P}$**(J/mol.K)**
i-C_4H_{10}	96.48	i-$C_{27}H_{56}$	623.79	i-$C_{50}H_{102}$	1148.05
i-C_5H_{12}	118.65	i-$C_{28}H_{58}$	647.38	i-$C_{51}H_{104}$	1169.96
i-C_6H_{14}	141.91	i-$C_{29}H_{60}$	670.05	i-$C_{52}H_{106}$	1184.95
i-C_7H_{16}	164.10	i-$C_{30}H_{62}$	689.79	i-$C_{53}H_{108}$	1214.11
i-C_8H_{18}	187.22	i-$C_{31}H_{64}$	716.90	i-$C_{54}H_{110}$	1237.50
i-C_9H_{20}	210.17	i-$C_{32}H_{66}$	736.64	i-$C_{55}H_{112}$	1253.57
i-$C_{10}H_{22}$	232.59	i-$C_{33}H_{68}$	765.67	i-$C_{56}H_{114}$	1281.67
i-$C_{11}H_{24}$	257.19	i-$C_{34}H_{70}$	784.82	i-$C_{57}H_{116}$	1301.49
i-$C_{12}H_{26}$	280.89	i-$C_{35}H_{72}$	803.64	i-$C_{58}H_{118}$	1325.16
i-$C_{13}H_{28}$	303.42	i-$C_{36}H_{74}$	832.63	i-$C_{59}H_{120}$	1350.50
i-$C_{14}H_{30}$	325.96	i-$C_{37}H_{76}$	850.82	i-$C_{60}H_{122}$	1365.27
i-$C_{15}H_{32}$	348.36	i-$C_{38}H_{78}$	878.45	i-$C_{61}H_{124}$	1396.09
i-$C_{16}H_{34}$	371.04	i-$C_{39}H_{80}$	898.74	i-$C_{62}H_{126}$	1427.67
i-$C_{17}H_{36}$	394.63	i-$C_{40}H_{82}$	917.50	i-$C_{63}H_{128}$	1448.02
i-$C_{18}H_{38}$	418.03	i-$C_{41}H_{84}$	939.31	i-$C_{64}H_{130}$	1467.51
i-$C_{19}H_{40}$	440.70	i-$C_{42}H_{86}$	964.36	i-$C_{65}H_{132}$	1495.84
i-$C_{20}H_{42}$	463.41	i-$C_{43}H_{88}$	984.07	i-$C_{66}H_{134}$	1515.42
i-$C_{21}H_{44}$	487.24	i-$C_{44}H_{90}$	1003.82	i-$C_{67}H_{136}$	1540.68
i-$C_{22}H_{46}$	509.94	i-$C_{45}H_{92}$	1028.44	i-$C_{68}H_{138}$	1560.03
i-$C_{23}H_{48}$	532.63	i-$C_{46}H_{94}$	1048.20	i-$C_{69}H_{140}$	1580.90
i-$C_{24}H_{50}$	555.01	i-$C_{47}H_{96}$	1076.93	i-$C_{70}H_{142}$	1608.85
i-$C_{25}H_{52}$	577.76	i-$C_{48}H_{98}$	1096.98	H_2	28.81
i-$C_{26}H_{54}$	600.23	i-$C_{49}H_{100}$	1120.63		

Table A.7. Heat capacity constants of species.

Species	A	B	C	D	E	F
n-CH_4	-1.46E-01	6.00E-04	-8.74E-07	6.78E-10	-2.75E-13	4.58E-17
n-C_2H_6	-1.74E-01	1.11E-03	-1.93E-06	1.70E-09	-7.57E-13	1.35E-16
n-C_3H_8	-1.75E-01	1.48E-03	-2.76E-06	2.51E-09	-1.14E-12	2.06E-16
n-C_4H_{10}	-3.44E-01	2.33E-03	-4.28E-06	3.90E-09	-1.77E-12	3.20E-16
n-C_5H_{12}	-1.49E-01	1.88E-03	-3.50E-06	3.14E-09	-1.42E-12	2.56E-16
n-C_6H_{14}	-2.55E-01	2.61E-03	-4.99E-06	4.63E-09	-2.17E-12	4.07E-16
n-C_7H_{16}	-2.75E-01	2.88E-03	-5.30E-06	4.66E-09	-2.02E-12	3.49E-16
n-C_8H_{18}	-2.78E-01	3.07E-03	-5.44E-06	4.47E-09	-1.77E-12	2.65E-16
n-C_9H_{20}	5.69E-02	2.37E-03	-4.70E-06	4.20E-09	-1.84E-12	3.21E-16
n-$C_{10}H_{22}$	9.81E-03	2.88E-03	-5.76E-06	5.24E-09	-2.35E-12	4.20E-16
n-$C_{11}H_{24}$	1.11E+00	-2.11E-03	4.39E-06	-4.91E-09	2.58E-12	-5.13E-16
n-$C_{12}H_{26}$	5.88E-01	5.22E-04	-9.56E-07	4.63E-10	-5.57E-14	-8.16E-18
n-$C_{13}H_{28}$	9.37E-01	-1.06E-03	2.97E-06	-4.29E-09	2.65E-12	-5.86E-16
n-$C_{14}H_{30}$	9.78E-01	-9.26E-04	2.52E-06	-3.68E-09	2.26E-12	-4.96E-16
n-$C_{15}H_{32}$	1.07E+00	-1.17E-03	3.35E-06	-4.94E-09	3.07E-12	-6.85E-16
n-$C_{16}H_{34}$	1.13E+00	-1.23E-03	3.55E-06	-5.26E-09	3.29E-12	-7.35E-16
n-$C_{17}H_{36}$	9.64E-01	1.25E-04	-9.71E-08	-6.48E-10	5.87E-13	-1.44E-16
n-$C_{18}H_{38}$	1.09E+00	-1.55E-04	4.17E-07	-1.16E-09	8.33E-13	-1.89E-16
n-$C_{19}H_{40}$	1.16E+00	-2.17E-04	5.42E-07	-1.32E-09	9.28E-13	-2.09E-16
n-$C_{20}H_{42}$	1.21E+00	-1.57E-04	4.23E-07	-1.24E-09	8.99E-13	-2.05E-16
n-$C_{21}H_{44}$	-4.53E-01	7.26E-03	-1.39E-05	1.26E-08	-5.69E-12	1.02E-15
n-$C_{22}H_{46}$	-4.74E-01	7.60E-03	-1.46E-05	1.32E-08	-5.95E-12	1.07E-15
n-$C_{23}H_{48}$	-4.95E-01	7.94E-03	-1.52E-05	1.38E-08	-6.21E-12	1.11E-15
n-$C_{24}H_{50}$	-5.17E-01	8.28E-03	-1.59E-05	1.44E-08	-6.48E-12	1.16E-15
n-$C_{25}H_{52}$	-5.38E-01	8.62E-03	-1.65E-05	1.50E-08	-6.74E-12	1.21E-15
n-$C_{26}H_{54}$	-5.59E-01	8.96E-03	-1.72E-05	1.56E-08	-7.01E-12	1.25E-15
n-$C_{27}H_{56}$	-5.81E-01	9.30E-03	-1.78E-05	1.62E-08	-7.27E-12	1.30E-15
n-$C_{28}H_{58}$	-6.02E-01	9.65E-03	-1.85E-05	1.68E-08	-7.53E-12	1.35E-15
n-$C_{29}H_{60}$	-6.23E-01	9.99E-03	-1.92E-05	1.74E-08	-7.80E-12	1.39E-15

Table A.7. Heat capacity constants of species, continued.

n-$C_{30}H_{62}$	-6.45E-01	1.03E-02	-1.98E-05	1.79E-08	-8.06E-12	1.44E-15
n-$C_{31}H_{64}$	-6.66E-01	1.07E-02	-2.05E-05	1.85E-08	-8.32E-12	1.49E-15
n-$C_{32}H_{66}$	-6.88E-01	1.10E-02	-2.11E-05	1.91E-08	-8.59E-12	1.53E-15
n-$C_{33}H_{68}$	-7.09E-01	1.14E-02	-2.18E-05	1.97E-08	-8.85E-12	1.58E-15
n-$C_{34}H_{70}$	-7.30E-01	1.17E-02	-2.24E-05	2.03E-08	-9.11E-12	1.63E-15
n-$C_{35}H_{72}$	-7.52E-01	1.20E-02	-2.31E-05	2.09E-08	-9.38E-12	1.67E-15
n-$C_{36}H_{74}$	-7.73E-01	1.24E-02	-2.37E-05	2.15E-08	-9.64E-12	1.72E-15
n-$C_{37}H_{76}$	-7.94E-01	1.27E-02	-2.44E-05	2.21E-08	-9.90E-12	1.77E-15
n-$C_{38}H_{78}$	-8.16E-01	1.31E-02	-2.50E-05	2.27E-08	-1.02E-11	1.81E-15
n-$C_{39}H_{80}$	-8.37E-01	1.34E-02	-2.57E-05	2.33E-08	-1.04E-11	1.86E-15
n-$C_{40}H_{82}$	-8.59E-01	1.37E-02	-2.64E-05	2.38E-08	-1.07E-11	1.91E-15
n-$C_{41}H_{84}$	-3.48E+00	2.70E-02	-5.59E-05	5.60E-08	-2.75E-11	5.27E-15
n-$C_{42}H_{86}$	-3.57E+00	2.77E-02	-5.72E-05	5.73E-08	-2.81E-11	5.40E-15
n-$C_{43}H_{88}$	-3.65E+00	2.83E-02	-5.85E-05	5.86E-08	-2.87E-11	5.52E-15
n-$C_{44}H_{90}$	-3.73E+00	2.89E-02	-5.98E-05	5.99E-08	-2.94E-11	5.64E-15
n-$C_{45}H_{92}$	-3.82E+00	2.96E-02	-6.12E-05	6.13E-08	-3.01E-11	5.78E-15
n-$C_{46}H_{94}$	-3.90E+00	3.02E-02	-6.25E-05	6.26E-08	-3.07E-11	5.90E-15
n-$C_{47}H_{96}$	-3.98E+00	3.09E-02	-6.38E-05	6.39E-08	-3.14E-11	6.02E-15
n-$C_{48}H_{98}$	-4.08E+00	3.16E-02	-6.54E-05	6.55E-08	-3.21E-11	6.17E-15
n-$C_{49}H_{100}$	-4.15E+00	3.22E-02	-6.65E-05	6.66E-08	-3.27E-11	6.27E-15
n-$C_{50}H_{102}$	-4.23E+00	3.29E-02	-6.79E-05	6.80E-08	-3.34E-11	6.41E-15
n-$C_{51}H_{104}$	-4.33E+00	3.36E-02	-6.94E-05	6.95E-08	-3.41E-11	6.55E-15
n-$C_{52}H_{106}$	-4.40E+00	3.41E-02	-7.06E-05	7.07E-08	-3.47E-11	6.66E-15
n-$C_{53}H_{108}$	-4.50E+00	3.49E-02	-7.21E-05	7.22E-08	-3.54E-11	6.80E-15
n-$C_{54}H_{110}$	-4.57E+00	3.55E-02	-7.34E-05	7.35E-08	-3.61E-11	6.92E-15
n-$C_{55}H_{112}$	-4.66E+00	3.61E-02	-7.47E-05	7.48E-08	-3.67E-11	7.04E-15
n-$C_{56}H_{114}$	-4.74E+00	3.68E-02	-7.60E-05	7.61E-08	-3.74E-11	7.17E-15
n-$C_{57}H_{116}$	-4.82E+00	3.74E-02	-7.74E-05	7.75E-08	-3.80E-11	7.30E-15
n-$C_{58}H_{118}$	-4.91E+00	3.81E-02	-7.88E-05	7.89E-08	-3.87E-11	7.43E-15

Table A.7. Heat capacity constants of species, continued.

n-$C_{59}H_{120}$	-5.00E+00	3.88E-02	-8.02E-05	8.03E-08	-3.94E-11	7.57E-15
n-$C_{60}H_{122}$	-5.07E+00	3.93E-02	-8.13E-05	8.14E-08	-4.00E-11	7.67E-15
n-$C_{61}H_{124}$	-5.16E+00	4.01E-02	-8.28E-05	8.29E-08	-4.07E-11	7.81E-15
n-$C_{62}H_{126}$	-1.33E+00	2.13E-02	-4.07E-05	3.68E-08	-1.65E-11	2.94E-15
n-$C_{63}H_{128}$	-1.35E+00	2.16E-02	-4.14E-05	3.74E-08	-1.68E-11	2.98E-15
n-$C_{64}H_{130}$	-1.37E+00	2.19E-02	-4.21E-05	3.80E-08	-1.70E-11	3.03E-15
n-$C_{65}H_{132}$	-1.39E+00	2.23E-02	-4.27E-05	3.86E-08	-1.73E-11	3.08E-15
n-$C_{66}H_{134}$	-1.41E+00	2.26E-02	-4.34E-05	3.92E-08	-1.75E-11	3.12E-15
n-$C_{67}H_{136}$	-1.44E+00	2.30E-02	-4.40E-05	3.98E-08	-1.78E-11	3.17E-15
n-$C_{68}H_{138}$	-1.46E+00	2.33E-02	-4.47E-05	4.04E-08	-1.81E-11	3.22E-15
n-$C_{69}H_{140}$	-1.48E+00	2.36E-02	-4.53E-05	4.10E-08	-1.83E-11	3.26E-15
n-$C_{70}H_{142}$	-1.50E+00	2.40E-02	-4.60E-05	4.16E-08	-1.86E-11	3.31E-15
i-C_4H_{10}	-1.49E-01	1.76E-03	-3.40E-06	3.14E-09	-1.43E-12	2.59E-16
i-C_5H_{12}	-2.64E-01	2.37E-03	-4.45E-06	4.08E-09	-1.87E-12	3.41E-16
i-C_6H_{14}	-3.72E-01	3.07E-03	-5.72E-06	5.15E-09	-2.29E-12	4.04E-16
i-C_7H_{16}	-4.05E-01	3.43E-03	-6.34E-06	5.62E-09	-2.46E-12	4.24E-16
i-C_8H_{18}	-4.73E-01	3.96E-03	-7.30E-06	6.45E-09	-2.80E-12	4.80E-16
i-C_9H_{20}	-1.05E-01	3.09E-03	-6.11E-06	5.62E-09	-2.55E-12	4.59E-16
i-$C_{10}H_{22}$	-1.27E-01	3.47E-03	-6.89E-06	6.36E-09	-2.90E-12	5.28E-16
i-$C_{11}H_{24}$	-2.60E-01	3.92E-03	-7.49E-06	6.80E-09	-3.07E-12	5.51E-16
i-$C_{12}H_{26}$	-2.81E-01	4.26E-03	-8.15E-06	7.39E-09	-3.33E-12	5.98E-16
i-$C_{13}H_{28}$	-3.03E-01	4.60E-03	-8.80E-06	8.00E-09	-3.60E-12	6.45E-16
i-$C_{14}H_{30}$	-3.24E-01	4.94E-03	-9.45E-06	8.57E-09	-3.86E-12	6.92E-16
i-$C_{15}H_{32}$	-3.46E-01	5.28E-03	-1.01E-05	9.16E-09	-4.12E-12	7.39E-16
i-$C_{16}H_{34}$	-3.67E-01	5.62E-03	-1.08E-05	9.75E-09	-4.39E-12	7.85E-16
i-$C_{17}H_{36}$	-3.88E-01	5.97E-03	-1.14E-05	1.03E-08	-4.65E-12	8.32E-16
i-$C_{18}H_{38}$	-4.10E-01	6.31E-03	-1.21E-05	1.09E-08	-4.91E-12	8.79E-16
i-$C_{19}H_{40}$	-4.31E-01	6.65E-03	-1.27E-05	1.15E-08	-5.18E-12	9.26E-16
i-$C_{20}H_{42}$	-4.52E-01	6.99E-03	-1.34E-05	1.21E-08	-5.44E-12	9.73E-16

Table A.7. Heat capacity constants of species, continued.

i-$C_{21}H_{44}$	-4.53E-01	7.26E-03	-1.39E-05	1.26E-08	-5.69E-12	1.02E-15
i-$C_{22}H_{46}$	-4.74E-01	7.60E-03	-1.46E-05	1.32E-08	-5.95E-12	1.07E-15
i-$C_{23}H_{48}$	-4.95E-01	7.94E-03	-1.52E-05	1.38E-08	-6.21E-12	1.11E-15
i-$C_{24}H_{50}$	-5.17E-01	8.28E-03	-1.59E-05	1.44E-08	-6.48E-12	1.16E-15
i-$C_{25}H_{52}$	-5.38E-01	8.62E-03	-1.65E-05	1.50E-08	-6.74E-12	1.21E-15
i-$C_{26}H_{54}$	-5.59E-01	8.96E-03	-1.72E-05	1.56E-08	-7.01E-12	1.25E-15
i-$C_{27}H_{56}$	-5.81E-01	9.30E-03	-1.78E-05	1.62E-08	-7.27E-12	1.30E-15
i-$C_{28}H_{58}$	-6.02E-01	9.65E-03	-1.85E-05	1.68E-08	-7.53E-12	1.35E-15
i-$C_{29}H_{60}$	-6.23E-01	9.99E-03	-1.92E-05	1.74E-08	-7.80E-12	1.39E-15
i-$C_{30}H_{62}$	-6.45E-01	1.03E-02	-1.98E-05	1.79E-08	-8.06E-12	1.44E-15
i-$C_{31}H_{64}$	-6.66E-01	1.07E-02	-2.05E-05	1.85E-08	-8.32E-12	1.49E-15
i-$C_{32}H_{66}$	-6.88E-01	1.10E-02	-2.11E-05	1.91E-08	-8.59E-12	1.53E-15
i-$C_{33}H_{68}$	-7.09E-01	1.14E-02	-2.18E-05	1.97E-08	-8.85E-12	1.58E-15
i-$C_{34}H_{70}$	-7.30E-01	1.17E-02	-2.24E-05	2.03E-08	-9.11E-12	1.63E-15
i-$C_{35}H_{72}$	-7.52E-01	1.20E-02	-2.31E-05	2.09E-08	-9.38E-12	1.67E-15
i-$C_{36}H_{74}$	-7.73E-01	1.24E-02	-2.37E-05	2.15E-08	-9.64E-12	1.72E-15
i-$C_{37}H_{76}$	-7.94E-01	1.27E-02	-2.44E-05	2.21E-08	-9.90E-12	1.77E-15
i-$C_{38}H_{78}$	-8.16E-01	1.31E-02	-2.50E-05	2.27E-08	-1.02E-11	1.81E-15
i-$C_{39}H_{80}$	-8.37E-01	1.34E-02	-2.57E-05	2.33E-08	-1.04E-11	1.86E-15
i-$C_{40}H_{82}$	-8.59E-01	1.37E-02	-2.64E-05	2.38E-08	-1.07E-11	1.91E-15
i-$C_{41}H_{84}$	-3.48E+00	2.70E-02	-5.59E-05	5.60E-08	-2.75E-11	5.27E-15
i-$C_{42}H_{86}$	-3.57E+00	2.77E-02	-5.72E-05	5.73E-08	-2.81E-11	5.40E-15
i-$C_{43}H_{88}$	-3.65E+00	2.83E-02	-5.85E-05	5.86E-08	-2.87E-11	5.52E-15
i-$C_{44}H_{90}$	-3.73E+00	2.89E-02	-5.98E-05	5.99E-08	-2.94E-11	5.64E-15
i-$C_{45}H_{92}$	-3.82E+00	2.96E-02	-6.12E-05	6.13E-08	-3.01E-11	5.78E-15
i-$C_{46}H_{94}$	-3.90E+00	3.02E-02	-6.25E-05	6.26E-08	-3.07E-11	5.90E-15
i-$C_{47}H_{96}$	-3.98E+00	3.09E-02	-6.38E-05	6.39E-08	-3.14E-11	6.02E-15
i-$C_{48}H_{98}$	-4.08E+00	3.16E-02	-6.54E-05	6.55E-08	-3.21E-11	6.17E-15
i-$C_{49}H_{100}$	-4.15E+00	3.22E-02	-6.65E-05	6.66E-08	-3.27E-11	6.27E-15

Table A.7. Heat capacity constants of species, continued.

i-$C_{50}H_{102}$	-4.23E+00	3.29E-02	-6.79E-05	6.80E-08	-3.34E-11	6.41E-15
i-$C_{51}H_{104}$	-4.33E+00	3.36E-02	-6.94E-05	6.95E-08	-3.41E-11	6.55E-15
i-$C_{52}H_{106}$	-4.40E+00	3.41E-02	-7.06E-05	7.07E-08	-3.47E-11	6.66E-15
i-$C_{53}H_{108}$	-4.50E+00	3.49E-02	-7.21E-05	7.22E-08	-3.54E-11	6.80E-15
i-$C_{54}H_{110}$	-4.57E+00	3.55E-02	-7.34E-05	7.35E-08	-3.61E-11	6.92E-15
i-$C_{55}H_{112}$	-4.66E+00	3.61E-02	-7.47E-05	7.48E-08	-3.67E-11	7.04E-15
i-$C_{56}H_{114}$	-4.74E+00	3.68E-02	-7.60E-05	7.61E-08	-3.74E-11	7.17E-15
i-$C_{57}H_{116}$	-4.82E+00	3.74E-02	-7.74E-05	7.75E-08	-3.80E-11	7.30E-15
i-$C_{58}H_{118}$	-4.91E+00	3.81E-02	-7.88E-05	7.89E-08	-3.87E-11	7.43E-15
i-$C_{59}H_{120}$	-5.00E+00	3.88E-02	-8.02E-05	8.03E-08	-3.94E-11	7.57E-15
i-$C_{60}H_{122}$	-5.07E+00	3.93E-02	-8.13E-05	8.14E-08	-4.00E-11	7.67E-15
i-$C_{61}H_{124}$	-5.16E+00	4.01E-02	-8.28E-05	8.29E-08	-4.07E-11	7.81E-15
i-$C_{62}H_{126}$	-1.33E+00	2.13E-02	-4.07E-05	3.68E-08	-1.65E-11	2.94E-15
i-$C_{63}H_{128}$	-1.35E+00	2.16E-02	-4.14E-05	3.74E-08	-1.68E-11	2.98E-15
i-$C_{64}H_{130}$	-1.37E+00	2.19E-02	-4.21E-05	3.80E-08	-1.70E-11	3.03E-15
i-$C_{65}H_{132}$	-1.39E+00	2.23E-02	-4.27E-05	3.86E-08	-1.73E-11	3.08E-15
i-$C_{66}H_{134}$	-1.41E+00	2.26E-02	-4.34E-05	3.92E-08	-1.75E-11	3.12E-15
i-$C_{67}H_{136}$	-1.44E+00	2.30E-02	-4.40E-05	3.98E-08	-1.78E-11	3.17E-15
i-$C_{68}H_{138}$	-1.46E+00	2.33E-02	-4.47E-05	4.04E-08	-1.81E-11	3.22E-15
i-$C_{69}H_{140}$	-1.48E+00	2.36E-02	-4.53E-05	4.10E-08	-1.83E-11	3.26E-15
i-$C_{70}H_{142}$	-1.50E+00	2.40E-02	-4.60E-05	4.16E-08	-1.86E-11	3.31E-15
H_2	6.97E-02	-2.00E-04	2.89E-07	-2.22E-10	8.81E-14	-1.42E-17

REFERENCES

1. Ehrfeld, W., V. Hessel, and H. Löwe, *Microreactors: New Technology for Modern Chemistry*, Wiley-VCH Verlag GmbH, Weinheim, Germany, 2000.

2. Ehrfeld, W., V. Hessel, and V Haverkamp, *Microreactors, Ulman's Encyclopedia of Industrial Chemistry*, Wiley-VCH Verlag GmbH, Weinheim, Germany, 1999.

3. Charpentier, J. C., "In The Frame of Globalization and Sustainability, Process Intensification, a Path to the Future of Chemical and Process Engineering (Molecules Into Money)", *Chemical Engineering Journal*, Vol. 134, pp. 84-92, 2007.

4. Wirth, T., Microreactors in Organic Synthesis and Catalysis, Wiley-VCH Verlag GmbH, Weinheim, Germany, 2008.

5. Hardt, S., W. Ehrfeld, V. Hessel, and K.M. Bussche, "Strategies for Size Reduction of Microreactors by Heat Transfer Enhancement Effects", *Chemical Engineering Communications*, Vol. 190, pp. 540-559, 2003.

6. Hessel, V., and H. Löwe, "Microchemical Engineering: Components, Plant Concepts, User Acceptance - Part II", *Chemical Engineering Technology*, Vol. 26, pp. 391-408, 2003.

7. Kiwi-Minsker, L., and A. Renken, "Microstructured Reactors for Catalytic Reactions", *Catalysis Today*, Vol.110, pp. 2-14, 2005.

8. Herskowits, D., V. Herskovits, and K. Stephan, "Characterization of a Two-Phase Impinging Jet Absorber- II. Absorbtion with Chemical Reaction of CO_2 in NaOH Solutions", *Chemical Engineerins Science*, Vol. 45, pp. 1281-1287, 1990.

9. Tonkovich, A.Y., S. Perry, Y. Wang, D. Qui, T. LaPlante, and W.A. Rogers, "Microchannel Process Technology for Compact Methane Steam Reforming", *Chemical*

Engineering Science, Vol. 59, pp. 4819-4824, 2004.

10. Hessel, V., and G. Kolb, "Microstructured Reactors for Gas Phase Reactions", *Chemical Engineering Journal*, Vol. 98, pp. 1-38, 2004.

11. Veser, G., and J. Frauhammer, "Modeling Steady State and Ignition During Catalytic Methane Oxidation in a Monolith Reactor", *Chemical Engineering Science*, Vol. 55, pp. 2271-2286, 2000.

12. Veser, G., "Experimental and Theoretical Investigation of H_2 Oxidation in a High Temperature Catalytic Microreactor", *Chemical Engineering Science*, Vol. 56, pp. 1265-1273, 2001.

13. Janickle, M.T., H. Kestenbaum, U.I. Hagendorf, F. Schüth, M. Fitchnerand, and K. Schubert, "The Controlled Oxidation of Hydrogen from an Explosive Mixture of Gases Using a Microstructured Reactor/Heat Exchanger and Pt/Al_2O_3 Catalyst", *Journal of Catalysis*, Vol. 191, pp. 282-293, 2000.

14. Fithcner, M., J. Mayer, D. Wolf, and K. Schubert, "Microstructured Rhodium Catalysts for Partial Oxidation of Methane to Syngas under Pressure", *Industrial and Engineering Chemistry Research*, Vol. 40, pp. 3475-3483, 2001.

15. Hasebe, S., "Design and Operation of Micro-Chemical Plants - Bridging the Gap between Nano, Micro and Macro Technologies", *Computers and Chemical Engineering*, Vol. 29, pp. 57-64, 2004.

16. Gandia, L.M., G. Arzamendi, P.M. Dieguez, M. Montes, J.A. Odriozola, and E. Falabella Sousa-Aguiar, "Computational Fluid Dynamics Study of Heat Transfer in a Microchannel Reactor for Low Temperature Fischer-Tropsch Synthesis", *Chemical Engineering Journal*, Vol 160, pp. 915-922, 2010.

17. Gandia, L.M., G. Arzamendi, P.M. Dieguez, M. Montes, J.A. Odriozola, and E. Falabella Sousa-Aguiar, "Methane Steam Reforming in a Microchannel Reactor for

GTL Intensification: A Computational Fluid Dynamics Simulation Study", *Chemical Engineering Journal*, Vol 154, pp. 168-173, 2009.

18. Chin, Y., J. Hu, C. Cao, Y. Gao, and Y. Wang, "Preparation of a Novel Structured Catalyst Based on Aligned Carbon Nanotube Arrays for a Microchannel Fischer-Tropsch Synthesis Reactor", *Catalysis Today*, Vol 110, pp. 47-52, 2005.

19. Seris, E.L.C., G. Abramowitz, A. M. Johnston, and B.S. Haynes, "Scalable, Microstructured Plant for Steam Reforming of Methane", *Chemical Engineering Journal*, Vol. 135, pp. 9-16, 2008.

20. Davis, B. H., "Overview of Reactors for Liquid Phase Fischer-Tropsch Synhtesis", *Catalysis Today*, Vol. 71, pp. 249-300, 2002.

21. Agarwal, A. K., "Biofules (Alcohols and Biodiesel) Applications as Fuel for Internal Combustion Engines", *Progress in Energy and Combustion Science*, Vol. 33, pp. 233-271, 2007.

22. Dry, M.E., "Fischer-Tropsch Reactions and Environment", *Applied Catalysis A: General*, Vol 189, pp. 185-190, 1999.

23. Yang, J.I., J.H. Yang, H.J. Kim, D.H. Chun, H.T. Lerr, J.C. Hong, and H. Jung, "Mass Transfer Limitations on Fixed-Bed Reactor for Fischer–Tropsch Synthesis", *Fuel Processing Technology*, Vol 91, pp. 285-289, 2010.

24. Hunt, V.D., *Synfuels Handbook*, Industrial Press Inc, New York, USA, 1983.

25. Dry, M.E. "Practical and Theoretical Aspects of the Catalytic Fischer-Tropsch Process" *Applied Catalalysis. A: General*, Vol. 138, pp.319-344, 1996.

26. Vliet, O.P.R., A.P.C. Faaij, and W.C. Turkenburg, "Fischer–Tropsch Diesel Production in a Well-to-Wheel Perspective: A carbon, Energy Flow and Cost Analysis", *Energy conversion and Management*, Vol 50, pp. 855-876, 2009.

27. Gill S.S., A. Tsolakis, K.D: Dearn, and J. Rodriguez-Fernandez, "Combustion Characteristics and Emissions of Fischer Tropsch Diesel Fuels in IV Engines", *Progress in Energy and Combustion Science*, Vol. 37, pp. 503-523, 2011

28. Bezemer, G.L., A. van Laak, A.J. van Dillen and K.P. de Jong, "Cobalt Supported on Carbon Nanofibers - a Promising Novel Fischer-Tropsch Catalysts", *Studies in Surface Science and Catalysis*, Vol. 147, pp. 259-264, 2004.

29. Dry, M.E., "The Fischer-Tropsch Process: 1950-200", *Catalysis Today*, Vol. 77, pp. 227-241, 2002.

30. Samuel P., "GTL Technology Challenges and Opportunities in Catalyst", *Bulletin of the Catalysis Society of India*, Vol. 2, pp. 82-99, 2003

31. Höök, M., and K. Aleklett, "A Review on Coal to Liquid Fuels and Its Coal Consumption", *International Journal of Energy Research*, Vol. 34, pp. 348-364, 2009.

32. Leckel, D., "Diesel Production from Fischer Tropsch; the Past, the Present, and New Concepts", *Energy Fuels*, Vol. 23, pp. 2342-2358, 2009

33. Abu-Jrai A, J. Rodríguez-Fernández, A. Tsolakis, A Megaritis, K. Theinnoi, and R.F. Cracknell, "Performance, Combustion and Emissions of a Diesel Engine Operated with Reformed EGR. Comparison of Diesel and GTL Fuelling.", *Fuel*, Vol. 88, pp. 1031-1041, 2009.

34. Guettel R. and T. Turek, "Comparison of Different Reactor Types for Low Temperature Fischer–Tropsch Synthesis: A Simulation Study", *Chemical Engineering Science*, Vol. 64, pp. 955-964, 2009.

35. Gumuslu, G., and A.K. Avci, "Parametric Analysis of Fischer-Tropsch Synthesis in a Catalytic Microchannel Reactor", *AIChe Journal*, DOI 10.1002/aic, 2011

36. Dieselnet Website, *Eurpean Union Diesel Regulations*, 2010, www.dieselnet.com/standards/eu/fuel.php, 03.05.2011

37. Kaufmann T.G., A. Kaldor, G.F. Stuntz, M.C. Kerby, and L.L. Ansell, "Catalysis Science and Technology for Cleaner Transportations Fuels.", *Catalysis Today*, Vol. 62, pp. 77-90, 2000.

38. Epdk.gov.tr, *Enerji Piyasası Düzenleme Kurumu Petrol Piyasası Mevzuat Klasörü Onüçüncü Revizyon*, 2011, www.epdk.org.tr/documents/10157/9685c981-e4fd-48e4-b24f-c4a524fc9a25, 03.05.2011

39. Fernandes F.A.N. and U.M. Teles, "Modeling and Optimization of Fischer-Tropsch Products Hydrocracking", *Fuel Processing Technology*, Vol. 88, pp. 207-214, 2007.

40. Calemma V., C. Gambaro, W.O. Parker Jr., and R. Caebone, "Middle Distillate from Hydrocracking of FT waxes; Composition, Characteristics and Emission Properties", *Catalysis Today*, Vol. 149, pp. 40-46, 2010.

41. Leckel, D., and M. Liwanga-Ehumbu, "Diesel-Selective Hydrocracking of an Iron-Based Fischer-Tropsch Wax Fraction (C_{15}-C_{45}) Using a MoO_3-Modified Noble Metal Catalyst", *Energy and Fuels*, Vol. 20, pp. 2330-2336, 2006.

42. Gamba, S., L.A. Pellegrini, V. Calemma, and C. Gambaro, "Liquid fuels from Fischer-Tropsch Wax Hydrocracking: Isomer Distribution", *Catalysis Today*, Vol. 156, pp. 58-64, 2010.

43. Chavarria J.C., J. Ramirez, H. Gonzalez and M.A. Baltanas, "Modeling of N-hexadecane Hydroisomerization and Hydrocracking Reactions on a Mo/Hβ-Alumina Bi-functional Catalyst, Using the Single Event Concept", *Catalysis Today*, Vol. 98, pp. 235-242, 2004.

44. Rossetti I., C. Gambaro and V. Calemma, "Hydrocracking of Long Chain Linear Paraffins", *Chemical Engineering Journal*, Vol. 154, pp. 295-301, 2009.

45. Collins J.P., J.J.H.M.F. Freide, and B. Nay, "A History of Fischer-Tropsch Wax Upgrading at BP from Catalyst Screening Studies to Full Scale Demonstration in

Alaska", *Journal of Natural Gas Chemistry*, Vol. 15, pp. 1-10, 2006

46. Pellegrini L., S. Locatelli, S. Rasella, S. Bonomi, and V. Calemma, "Modeling of Fischer-Tropsch Products Hydrocracking", *Chemical Engineering Science*, Vol. 59, pp. 4781-4787, 2004.

47. Calemma V., S. Correra, C. Perego, P. Pollesel, and L. Pellegrini, "Hydroconversion of Fischer–Tropsch Waxes: Assessment of The Operating Conditions Effect by Factorial Design Experiments", *Catalysis Today*, Vol. 106, pp. 282-287, 2005.

48. Pellegrini L., S. Bonomi, S. Gamba, V. Calemma, and D. Molinari, "The all components hydrocracking model", *Chemical Engineering Science*, Vol. 62, pp. 5013-5020, 2007.

49. Pellegrini. L.A., S. Gamba, V. Calemma and S. Bonomi, "Modeling of Hydrocracking with Vapor-Liquid Equilibrium", *Chemical Engineering Science*, Vol 63, pp. 4285-4291, 2008.

50. Smith, J.M., H.C. Van Ness and M.M. Abbott, *Introduction to Chemical Engineering Thermodynamics*, 7th edn., McGraw Hill, Singapore, 2005.

51. Bird, R.B., W.E. Stewart and E.N. Lightfoot, *Transport Phenomena*, 2nd edn, Wiley, New York, 2007.

52. Avcı, A.K., D.L. Trimm and M. Karakaya, "Microreactor Catalytic Combustion for Chemicals Processing", *Catalysis Today*, Vol. 155, pp.66-74, 2010

53. Armatas, G.S., and P.J. Ponomis, "A Monte Carlo Pore Network for the Simulation of Porous Characteristics of Functionalized Silica: Pore Size Distribution, Connectivity Distribution and Mean Tortuosities", *Chemical Engineering Science*, Vol. 59, pp. 5735-5749, 2004.

54. Geankoplis, G.J., *Transport Processes and Separation Process Principles*, 4th edn, Prentice Hall, New Jersey, 2003.

55. Yaws, C.L., *Yaws' Handbook of Thermodynamic Properties for Hydrocarbons and Chemicals*, William Andrew, Norwich, NY, USA, 2009.

56. Yaws, C.L., *Transport Properties of Chemicals and Hydrocarbons* , William Andrew, Norwich, NY, USA, 2009.

57. Fogler, H.S., *Elements of Chemical Reaction Engineering*, 4th edn., Pearson, USA, 2006.